CONTROLLING ADATOM KINETICS TO OVERCOME TRADITIONAL LIMITATIONS FOR III-NITRIDE TERNARY ALLOYS

A Dissertation
Presented to
The Academic Faculty

by

Zachary Engel

In Partial Fulfillment
of the Requirements for the Degree
Doctor of Philosophy in the
School of Electrical and Computer Engineering

Georgia Institute of Technology
[December 2022]

COPYRIGHT © 2022 BY ZACHARY ENGEL

CONTROLLING ADATOM KINETICS TO OVERCOME TRADITIONAL LIMITATIONS FOR III-NITRIDE TERNARY ALLOYS

Approved by:

Dr. W. Alan Doolittle, Advisor

School of Electrical and Computer Engineering

Georgia Institute of Technology

Dr. William Hunt

School of Electrical and Computer Engineering

Georgia Institute of Technology

Dr. Mark D. Losego

School of Material Science and Engineering

Georgia Institute of Technology

Dr. Asif I. Khan

School of Electrical and Computer Engineering

Georgia Institute of Technology

Dr. Eric M. Vogel

School of Material Science and Engineering

Georgia Institute of Technology

Date Approved: [12/5/2022]

ACKNOWLEDGEMENTS

I would first like to thank my advisor Dr. Alan Doolittle for his support and guidance throughout the entire process of my study and research during my time at Georgia Tech. His constant backing of my work has been invaluable to me during these past five years and I greatly appreciate the time he has given to me and his assistance in overcoming the challenges I face both professionally and personally.

Second, I would like to thank my family for their continuous support during this time. My parents have provided moral support during the entire time I have been working towards my PhD. In addition to always being there when I needed to talk, I also appreciate the support they have given me in helping me get away and take vacations when I needed to step away from work for a time. I would also like to thank all my relatives who live in the south whose doors were always open to me when I wanted to get away from Atlanta for a few days.

None of this work would have been possible without the support of my colleagues. I would especially like to thank Dr. Evan Clinton and Dr. Ehsan Vadiee for their training and guidance in my initial time in the group. I would also like to thank all the members of my research group for their support of my work, including Dr. Habib Ahmad, Jobi Zivasatienraj, Alex Weidenbach, Chris Matthews, Keisuke Motoki, Sangho Lee, Tim McCrone, and Aheli Ghosh. Their time and effort taken on my behalf was of great assistance in the completion of my work.

Finally, I would like to thank all the members of the IEN staff for both their personal assistance in my training and tool usage and their general work in keeping an outstanding cleanroom facility for the graduate researchers of Georgia Tech.

TABLE OF CONTENTS

ACKNOWLEDGEMENTS **i**

LIST OF TABLES **vi**

LIST OF FIGURES **vii**

LIST OF SYMBOLS AND ABBREVIATIONS **xii**

SUMMARY **xv**

CHAPTER 1. Background **1**
1.1 History and Development of III-Nitrides **1**
1.2 Metal Modulated Epitaxy – A Novel MBE Technique for Low Temperature Growth **4**
1.3 Optoelectronic Development and Applications **7**
1.4 III-Nitride Photovoltaics **15**
1.5 Application of III-Nitrides Towards Power Electronics and RF Transistors **16**

CHAPTER 2. Application of Low Temperature, Metal Rich Growth for Improvement of Traditionally Difficult $Al_{0.3}In_{0.7}N$ Films **19**
2.1 Introduction **19**
2.2 Experimental **20**
2.3 1.3 Results and Discussion **22**
2.3.1 Establishment of Epitaxy Conditions 22
2.3.2 Establishment of MME Conditions 24
2.3.3 Optimization of MME Growth Conditions 29
2.3.4 Quantum Well Like Emissions Observed From Bulk Films 36
2.4 Conclusion **40**

CHAPTER 3. Application of MME Towards High Indium Content AlInN Over a Wide Composition Range **41**
3.1 Introduction **41**
3.2 Experimental **43**
3.3 Results and Discussion **44**
3.3.1 Structural Properties of High In Content AlInN 44
3.3.2 Strong Stokes Shift in the Photoluminescence of AlInN 49
3.3.3 Spectroscopic Ellipsometry – An Alternate Method of Determining Optical Properties 52
3.4 Conclusion **55**

CHAPTER 4. Hyper Doping of AlGaN for Improvement of Deep UV Optoelectronics 57
4.1 Introduction 57
4.2 Experimental Details 58
4.3 Results and Discussion 60
4.3.1 Hyper doping of AlxGa1-xN thin films 60
4.3.2 Realization of an AlGaN Homojunction Tunnel Diode 63
4.3.3 Investigation of Tunneling Behavior in High Al Content Devices. 66
4.3.4 Utilizing AlGaN Tunnel Contacts to Improve UV LEDs 68
4.4 Conclusion 70

CHAPTER 5. Adlayer Control for Tunable AlGaN Self-Assembled Superlattices72
5.1 Introduction 72
5.2 Experimental 75
5.3 Results and Discussion 77
5.3.1 Effects of Metal Dose on SASL Formation 77
5.3.2 Effects of III/V Ratio on SASL Parameters 83
5.3.3 Effects of Growth Rate on the Coherency of SASL Structures 86
5.3.4 5.3.4 Methods for Control of SASL Structure Parameters 87
5.4 Conclusion 89

CHAPTER 6. Discovery of a Significant Catylitic Effect for ScN Growth and Improved Nucleation of Cubic (111) ScN Films on Wurtzite (0002) GaN 91
6.1 Intro 91
6.2 Experimental Details 93
6.3 Results and discussion 95
6.3.1 Initiation Schemes for ScN Epitaxy 95
6.3.2 Surface Progression of (111) ScN Films 97
6.3.3 A Strong Catalytic Effect in ScN Growth 102
6.4 Conclusion 105

CHAPTER 7. Overcoming Metal Rich Surface Chemistry Limitations of ScAlN for High Electrical Performance Heterostructures 107
7.1 Introduction 107
7.2 Experimental Details 110
7.3 Results and Discussion 113
7.3.1 Growth Temperature Optimization of ScAlN 113
7.3.2 Metal Dose Optimization of ScAlN Growth 121
7.3.3 Low Temperature Growth Yields High Crystal Quality and Lattice Constants Close to Theory 127
7.3.4 High Performance HEMT Structures Demonstrated With Metal Rich ScAlN Growth 129
7.4 Conclusion 130

CHAPTER 8. Investigation of Crystal Structure and Phase Purity of Wurtzite ScAlN Over a Wide Composition Range 132
8.1 Introduction 132

8.2 Experimental Details 134
8.3 Results and Discussion 136
8.3.1 Shift of Lattice Constants with Composition 136
8.3.2 Phase Transition From Wurtzite to Cubic ScAlN 140
8.3.3 Electrical Performance of ScAlN Films Over a Range of Wurtzite Compositions 145
8.4 Conclusion 147

CHAPTER 9. Summary and Future Direction 149
9.1 Low Temperature Epitaxy of In-Rich AlInN 149
9.2 Hyper Doping of AlGaN for Electrical and Optical Device Applications 150
9.3 Investigation of Formation Mechanisms for AlGaN Self-Assembled Superlattices 150
9.4 Metal Rich Epitaxy of ScAlN for HEMT Improvement 151
9.5 Contributions 152
9.6 Future Directions 154
9.6.1 Overcome PL Emission Pinning for AlInN Films 154
9.6.2 Fabricated LED Structures With AlGaN SASL Structures 155
9.6.3 Investigate Low Temperature Growth of ScAlN for Device Applications 155
9.6.4 Fabricate Full HEMTs with metal rich ScAlN 155
9.6.5 Examine Ferroelectric Properties of metal rich ScAlN 156

Citations 157

LIST OF TABLES

Table 2.1 XRD figures of merit comparing the MME grown film and previous reports in literature for similar compositions. 27

Table 2.2: XRD figures of merit for AlInN films grown with MME over a range of substrate temperatures. 32

Table 2.3: Primary emission level and well width for quantum confined like emissions in AlInN films. 40

Table 3.1: XRD figures of merit for low temperature, MME grown AlInN. 47

Table 3.2: Extracted bandgaps at each composition from Tauc plot extrapolation. 55

Table 5.1: Parameters extracted from XRD simulations where four AlGaN films grown with four different shutter open times are compared. 80

Table 5.2: Parameters extracted from XRD simulations where two AlGaN films grown with two different III/V ratios are compared. 85

Table 5.3: Parameters extracted from XRD simulations where two AlGaN films grown with two different instantaneous growth rates are compared. 87

Table 6.1: Growth rates for ScN and AlN at various substrate temperatures. 104

Table 7.1: XRD rocking curve FWHM values for the ScAlN films grown under metal rich conditions at various growth temperatures. 116

Table 7.2: Growth rate at various substrate temperatures for ScN and AlN. 119

Table 7.3: XRD rocking curve FWHM values for the ScAlN films grown under metal rich conditions at various III/V ratios. 126

LIST OF FIGURES

Figure 1.1: Lattice constants vs band gap for traditional III-Nitride Alloys.[12] 2

Figure 1.2: Top-down diagram of a typical MBE Chamber. 4

Figure 1.3: XRD 2θ-ω curves showing high quality InGaN grown over the entire composition range with MME.[34] 5

Figure 1.4: XRD 2θ-ω curve of phase separated InGaN.[52] 8

Figure 1.5: Plan-view electron micrograph image of a honeycomb structure in an AlInN film. . 11

Figure 1.6: EQE vs current for an AlGaN LED showing efficiency droop with increased current.[87] 12

Figure 1.7: EQE Vs. Wavelength for AlGaN-based UV LEDs.[105,108] 14

Figure 1.8: Polarization generated interface sheet charge for various III-Nitride heterostructures.126 17

Figure 2.1: Indium incorporation vs. substrate temperature for AlInN growth. 23

Figure 2.2: XRD 2θ-ω curve of nitrogen rich AlInN grown with established initial conditions.. 24

Figure 2.3 XRD scans of single phase InGaN grown with the MME technique.[156] 25

Figure 2.4: XRD 2θ-ω scan of AlInN grown with MME. 28

Figure 2.5: AFM scans comparing the surfaces for MME vs traditional n-rich MBE growth of AlInN showing a significant improvement when using MME. 29

Figure 2.6: XRD scans of AlInN grown over a range of substrate temperatures. 31

Figure 2.7: XRD reciprocal space maps of the AlInN films grown at different substrate temperatures. 33

Figure 2.8: AFM scans of the AlInN films grown at varying substrate temperatures showing smooth surfaces for low growth temperatures. 36

Figure 2.9: PL measurements taken for the AlInN films grown at varied substrate temperatures. 37

Figure 2.10: 4 peak fitting of the PL emission for the sample grown at 350 ^{o}C........ 38

Figure 2.11: Peak energy vs index squared for fitted peaks modelling the PL emissions. 38

Figure 3.1: XRD 2θ-ω scans of AlInN films grown via MME at different compositions........ 46

Figure 3.2: AFM scans of AlInN films grown over a wide composition range. 49

Figure 3.3: PL Emission spectra for AlInN films grown over a wide composition range showing significant variation in both peak energy and intensity with composition. 50

Figure 3.4: (Top) Fit of the Tauc-Lorentz oscillator model to the raw SE data for the $Al_{0.3}In_{0.7}N$ sample. (Bottom) Tauc plots for AlInN films with compositions between 10 and 50% Al. 54

Figure 4.1: (a) Electron Concentration, (b) Resistivity, and (c) Mobility for four $Al_xGa_{1-x}N$ films of different compositions. Doping efficiency decreases with increasing Al content. 61

Figure 4.2: (a) Hole Concentration, (b) Resistivity, and (c) Mobility for four $Al_xGa_{1-x}N$ films of different compositions. Doping efficiency decreases with increasing Al content. 63

Figure 4.3: Tunnel diode structure (left) and J-V curve of the $Al_{0.08}Ga_{0.092}N$ homojunction tunnel diode. 65

Figure 4.4: Structure of the control AlGaN homojunction PIN diodes (left) and the tunnel diode (right). 67

Figure 4.5: JV curves of the homojunction AlGaN tunnel diodes with compositions of 19 (left), 42 (middle), and 58 (right) % Al. 68

Figure 4.6: Structure of the test AlGaN based UV LED with a traditional p-GaN contact layer (left) and structure of an AlGaN based UV diode with an AlGaN tunnel contact. 69

Figure 4.7: EL spectra of the control and tunnel contacted LEDs, showing an increase in intensity for the tunnel contacted device. 70

Figure 4.8: Light output power for the control and tunnel contacted LEDs showing a significant increase in output power for the tunnel contacted device. 70

Figure 5.1: XRD 2θ-ω scan (left) of a SASL. Cross sectional TEM image of the same (right). Both show exceptional coherency and abrupt interfaces. 75

Figure 5.2: XRD 2θ-ω scans of four AlGaN films grown with varying metal doses used to control the SASL period. 79

Figure 5.3: Room Temperature PL spectra of AlGaN SASL structures grown with a 10, 14, and 20 s dose showing control of emission energy. 83

Figure 5.4: XRD 2θ-ω scans of two AlGaN films grown with varying III/V ratios showing control over the well to barrier ratio. 84

Figure 5.5: XRD 2θ-ω scans of two AlGaN films grown with varying instantaneous growth rates showing increased coherency with increased instantaneous growth rate. 87

Figure 6.1: SEM surface image of a (111) ScN film grown on wurtzite GaN showing growth distinct rotated domains. 92

Figure 6.2: XRD 2θ-ω scan of a 111 ScN film grown on wurtzite GaN. Due to the lattice constants of the ScN, the peak is located inside the GaN peak and cannot be isolated. 96

Figure 6.3: RHEED progression during growth for the three different initiation methods. 98

Figure 6.4: AFM scans of the end of growth surfaces for the ScN films grown using different initiation schemes.. 100

Figure 6.5: TEM images highlighting the differences between the standard initiation methods and the Sc Buffer initiation. 102

Figure 7.1: XRD 2θ-ω curves of ScAlN grown under metal rich conditions at various growth temperatures. Phase pure growth is observed for growth at and above 650 ºC. 115

Figure 7.2: AFM scans of the ScAlN films grown under metal rich conditions at varying growth temperatures. Roughness reduction is observed with reduced growth temperature, with large droplets appearing at 600 ºC. 120

Figure 7.3: XRD 2θ-ω curves of ScAlN before and after a 20 minute HCL etch. The unintentional Al_3Sc peak is eliminated post etch. 121

Figure 7.4: XRD 2θ-ω curves of ScAlN grown under metal rich conditions at varying III/V ratios. Single phase growth is observed at higher III/V ratios, with phase purity being lost at a III/V ratio of 1.2. 125

Figure 7.5: Representative RHEED transient for ScAlN growth. Defined regions for metal shutter open and thus, metal accumulation (I), metal adlayer consumption (II), and dead time (III). 127

Figure 7.6: AFM scans of the ScAlN films grown under metal rich conditions at 650 ºC at various III/V ratios. 127

Figure 7.7: AFM scan (left) and XRD 2θ-ω scan of a $Sc_{0.18}Al_{0.82}N$ film growth at a low substrate temperature of 400 ºC. 129

Figure 7.8: XRD 2ω-θ scan and AFM scan of the ScAlN/GaN HEMT structure showing excellent crystallinity and surface roughness. 130

Figure 8.1: XRD scans of ScAlN films grown via MME over a wide composition range. 139

Figure 8.2: Wurtzite lattice constants vs Sc content for the ScAlN films. 140

Figure 8.3: End of growth RHEED images for the ScAlN films showing a progression of surface features with changing Sc content, as well as in ideal wurtzite and rock-salt RHEED pattern,. 141
Figure 8.4: TEM diffraction patterns of a GaN film (left) and a $Sc_{0.35}Al_{0.65}N$ film (right) showing a shift from a pure wurtzite pattern to a pattern containing multiple phases. 143
Figure 8.5: End of growth RHEED pattern for a 20 nm thick (left) and 150 nm thick (right) $Sc_{0.41}Al_{0.59}N$ film. The 20 nm film retains pure wurtzite RHEED pattern while the thicker film shows a polycrystalline nature. 145
Figure 8.6: Sheet charge and sheet resistance of three ScAlN HEMT structures grown at different Sc compositions. 147

LIST OF SYMBOLS AND ABBREVIATIONS

eV	Electron volt
LED	Light emitting diode
LD	Laser diode
UV	Ultraviolet
MBE	Molecular beam epitaxy
MOCVD	Metal organic chemical vapor deposition
RF	Radio Frequency
InN	Indium Nitride
InGaN	Indium Gallium Nitride
AlInN	Aluminum Indium Nitride
RHEED	Reflection high energy electron diffraction
MME	Metal modulated epitaxy
PAMBE	Plasma assisted molecular beam epitaxy
XRD	X-ray Diffraction
Mg	Magnesium
θ	Theta
ω	Omega
Ga	Gallium
In	Indium
Al	Aluminum
Sc	Scandium
AlGaN	Aluminum Gallium Nitride

AlN	Aluminum Nitride
GaN	Gallium Nitride
Ȧ	Angstrom
NRC	Non-radiative recombination center
a.u.	Arbitrary units
MQW	Multi-quantum well
QW	Quantum well
EQE	External quantum efficiency
2DEG	Two dimensional electron gas
ScAlN	Scandium Aluminum Nitride
MOVPE	Metal organic vapor phase epitaxy
PL	Photoluminescence
RT	Room temperature
AFM	Atomic force microscopy
III/V	Three/five
RMS	Root mean square
FWHM	Full width at half maximum
RSM	Reciprocal space map
DI	De-ionized
SE	Spectroscopic ellipsometry
RC	Rocking curve
SIMS	Secondary ion mass spectroscopy
NDR	Negative differential resistance
TC	Tunnel contact
EL	Electro luminescence

SASL	Self-assembled superlattice
SL	Superlattice
DBR	Distributed Bragg reflector
TEM	Transmission electron microscopy
HVPE	Hydride vapor phase epitaxy
PM	Psuedomorphic
LC	Laterally contracted
ScN	Scandium Nitride
ScGaN	Scandium Gallium Nitride
UID	Unintentionally doped
EDX	Energy dispersive x-ray spectroscopy
RBS	Rutherford backscattering

SUMMARY

III-Nitride ternary alloys are used in a wide range of applications in modern technology. Despite being a relatively mature technology in many aspects, shortcomings still exist and challenges remain to be overcome, particularly owing to the limited alloy range for which existing commercial fabrication methods can produce single phase III-Nitride alloys. The goal of this thesis is to significantly expand the commercially viable alloy ranges and to demonstrate this capability with several device advances. Advancements need to be made in both red-infrared and deep UV emitting devices to improve efficiency for solid state lighting. Despite having a high absorption coefficient and the ability to achieve almost all desirable bandgaps for photovoltaics, thus far all demonstrated photovoltaic devices have been low efficiency. Further advancements in RF switching and power electronics can be made by transitioning to ultra-wide bandgap materials and improving the electrical characteristics of both bulk films and 2D sheet charges at heterointerfaces.

AlInN is studied for its potential applications for both long wavelength LEDs and general photovoltaic applications. Initially, optimization of $Al_{0.3}In_{0.7}N$ was performed using metal modulated epitaxy (MME) due to this composition's bandgap of 1.7 eV, the ideal bandgap for a tandem with silicon solar cell. Growth conditions were studied and crystal quality 11x better than previous literature values was demonstrated. When using photoluminescence to assess the optical quality of the films, a significant Stoke's shift was observed resulting in an emission energy of 1.45 eV compared to the theoretical value of 1.7 eV. Furthermore, fitting of the emission spectra suggested emission from a quantum confined structure within the bulk of the film. Subsequently, the same growth method was applied to grow AlInN with compositions between 10% and 50% Al. X-ray diffraction (XRD) showed excellent crystalline quality for the entire composition range

for this traditionally difficult to grow, In-rich alloy. Photoluminescence showed a similar Stoke's shift as observed previously for $Al_{0.3}In_{0.7}N$ for the entire range of compositions, with even $Al_{0.5}In_{0.5}N$ showing an emission energy near 1.5 eV, well below the theoretical bandgap value of ~2.1 eV. To assess the true bandgap of the films and determine the absorption coefficients, spectroscopic ellipsometry was performed. Bandgaps near theory were determined via ellipsometry and high absorption coefficients useful for solar applications were measured.

AlGaN is the most commonly used material for solid state UV lighting. However, efficiency in deep UV emission is still a critical issue to be dealt with. In order to overcome a significant challenge in this field, ultra-high doping of AlGaN was investigated. Using MME, Si and Mg were applied for n and p type doping, respectively, of AlGaN with compositions between 0 and ~60% Al. An electron concentration as high as ~$4x10^{19}$ cm^{-3} was obtained for $Al_{0.6}Ga_{0.4}N$, but a hole concentration of only ~$4x10^{15}$ cm^{-3} was obtained for a similar composition. Regardless, such doping levels enabled the fabrication of tunnel diodes which demonstrated high reverse bias tunneling current even up to 62% Al and negative differential resistance up to a composition of 19%. These tunnel diodes were applied as tunnel contacts to a UV LED emitting at ~270 nm and lead to an increased in light output power of over 110% due to a reduction in parasitic emission over traditional GaN contacts. To attempt to improve the uniformity of AlGaN superlattice structures, like the multi-quantum wells used in UV LEDs, a novel method for the growth of self-assembled superlattices was studied. Such a method would eliminate the need for growth interrupts to adjust growth conditions between layers and eliminate the unintentional accumulation of contaminants during such interrupts. Control of the individual layer and overall period thicknesses was demonstrated, as well as control over the composition of the well layer within the superlattice.

Finally, it was observed that utilizing higher growth rates during the process resulted in more coherent and uniform superlattices even with thicknesses as high as a micron.

Recently, ScAlN has generated great attention due to its extremely high polarization coefficients and its ability to be lattice matched to GaN. A $Sc_{0.18}Al_{0.82}N$/GaN heterostructure can produce a sheet charge as high as ~$6x10^{13}$ cm^{-2} due to the polarization discontinuity between the two materials. This gives the material great potential as a barrier layer for high electron mobility transistors with low sheet resistances and high charge density for RF switching applications. Despite the benefits in using metal rich conditions for MBE growth of III-Nitrides, all prior attempts have resulted in a loss of phase purity due to the inclusion of cubic ScAlN phases and/or intermetallic inclusions. Here, MME is applied to achieve phase pure, metal rich growth of ScAlN over a wide composition range. Compositions up to 24% Sc were demonstrated with state-of-the-art crystal quality. Thick films of higher compositions demonstrated the inclusion of non-wurtzite phases to the point of polycrystallinity at 41% Sc. Low temperature growth was observed to mitigate the inclusion of cubic phases. In addition, films with thicknesses of ~20 nm maintained a pure wurtzite crystal even with compositions as high as 41% Sc. The ScAlN films demonstrated state-of-the-art electrical properties in ScAlN/GaN heterostructures, with a sheet charge as high as $5.9x10^{13}$ cm^{-3} and a sheet resistance as low as 152 Ω/□.

CHAPTER 1. BACKGROUND

1.1 History and Development of III-Nitrides

In the past few decades, the III-Nitride material system, traditionally consisting of InN, GaN, AlN, and their alloys, has enjoyed significant attention and has seen major advancements. These materials have a number of useful properties that have allowed them to jump to the forefront in multiple fields and markets. Their large breakdown fields, high mobilities, and high drift velocities have allowed many advances to be made in power electronics.[1–3] The tunable bandgap spanning 0.65 eV for InN to 6.1 eV for AlN covers the wavelength ranges from infrared light to ultraviolet light) shown in Figure 1.1, and low sensitivity to defects has allowed the III-Nitride material system to produce high efficiency green and blue light emitting diodes (LEDs) and laser diodes (LDs), as well as make strong advancements in violet and ultraviolet (UV) emission.[4–12] Additionally, due to the large absorption coefficients, high radiation hardness, and the tunable bandgap of the system, the III-Nitrides show strong promise for solar blind photodetectors and solar cell applications.[13]

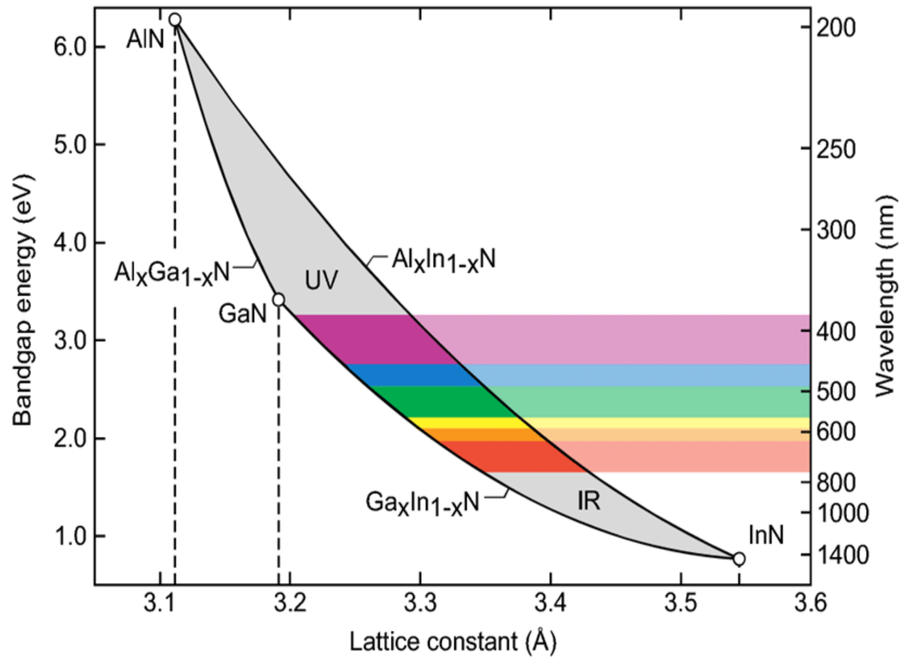

Figure 1.1: Lattice constants vs band gap for traditional III-Nitride Alloys.[12]

The years of research on the III-Nitride material system have seen the coming and going of various methods of synthesis, but the most common today are molecular beam epitaxy (MBE), metal organic chemical vapor deposition (MOCVD), and radio frequency sputtering (RF sputtering). All three of these methods provide active nitrogen and metal atoms in different ways. MBE provides metal atoms through a molecular (or atomic) beam of evaporated metal and active nitrogen is supplied either by the disassociation of ammonia on a hot substrate or by a RF plasma that provides a mixed stream of electrically excited molecular and atomic nitrogen to the surface and a diagram of a typical MBE chamber is shown in Figure 1.2.[14–16] MOCVD provides metal atoms and active nitrogen by flowing metalorganics, such as trimethylgallium, and ammonia onto a hot substrate where the molecules are broken apart and reformed as III-Nitride films on the surface.[17] In RF sputtering the metal atoms are sputtered onto a substrate and plasma activated nitrogen is provided.[18] MOCVD and RF sputtering are preferred by industry due to their high

scalability and the fact that these techniques can be performed at atmospheric pressure and low vacuum, whereas since MBE requires a large mean free path for the atomic beams it must be performed under ultra-high vacuum. However, MBE is not without its advantages. MBE has demonstrated an extremely fast growth rate of 9.6 μm/hr and, with the RF plasma method (known as plasma assisted MBE or PAMBE), it can grow at substrate temperatures far below that of MOCVD or even ammonia MBE. While the growth rate provides an advantage in speed, purity and throughput, the low growth temperature allows for the growth of high quality InN and indium bearing ternaries (InGaN and AlInN) as growth can be performed in temperature regimes that would prevent the decomposition of indium bearing materials and the desorption of indium metal.[19–21]

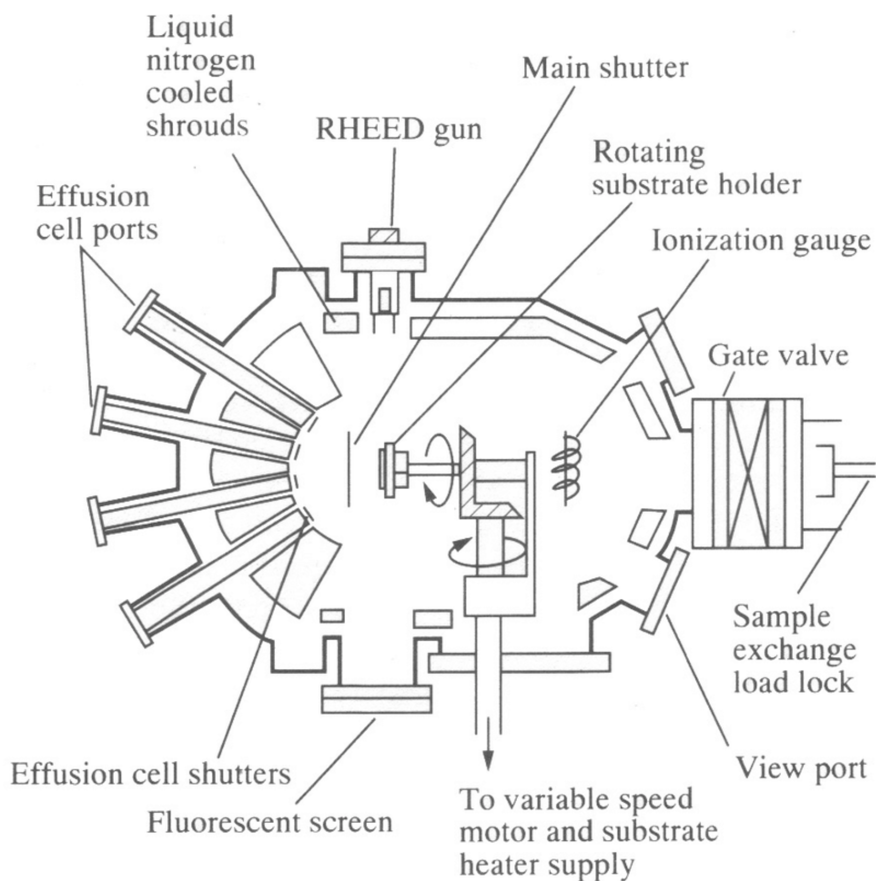

Figure 1.2: Top-down diagram of a typical MBE Chamber.

1.2 Metal Modulated Epitaxy – A Novel MBE Technique for Low Temperature Growth

A novel method of synthesis developed in recent years is Metal Modulated Epitaxy (MME). MME is a modified form of PAMBE which utilizes periodic (typically with periods less than ~30 s) shuttering of the metal fluxes whereas traditional PAMBE will not utilize shuttering during active growth, save for sparse interruption of growth to allow for the desorption of metal adlayers.[22] Additionally, MME will also use significantly metal rich fluxes, with ratios of metal flux to active nitrogen flux well over unity, typically 1.3 - 2. This is much higher than what is typically used for PAMBE, which is nitrogen rich or barely above stoichiometry (< ~1.05). This

technique has seen a number of advancements in the field of III-Nitrides, surpassing limitations present in more traditional growth techniques. Utilizing metal rich growth and high growth rates MME has demonstrated high quality InGaN over the entire composition range as demonstrated in the X-ray Diffraction (XRD) curves in Figure 1.3, Mg incorporation beyond the expected limits, and ultra-high doping of both electrons and holes, to list a few.[23–28] These advancements have allowed for the creation of III-Nitride based solar cells and homojunction GaN and AlGaN tunnel junctions to enhance solar cell and LED performance.[29–33]

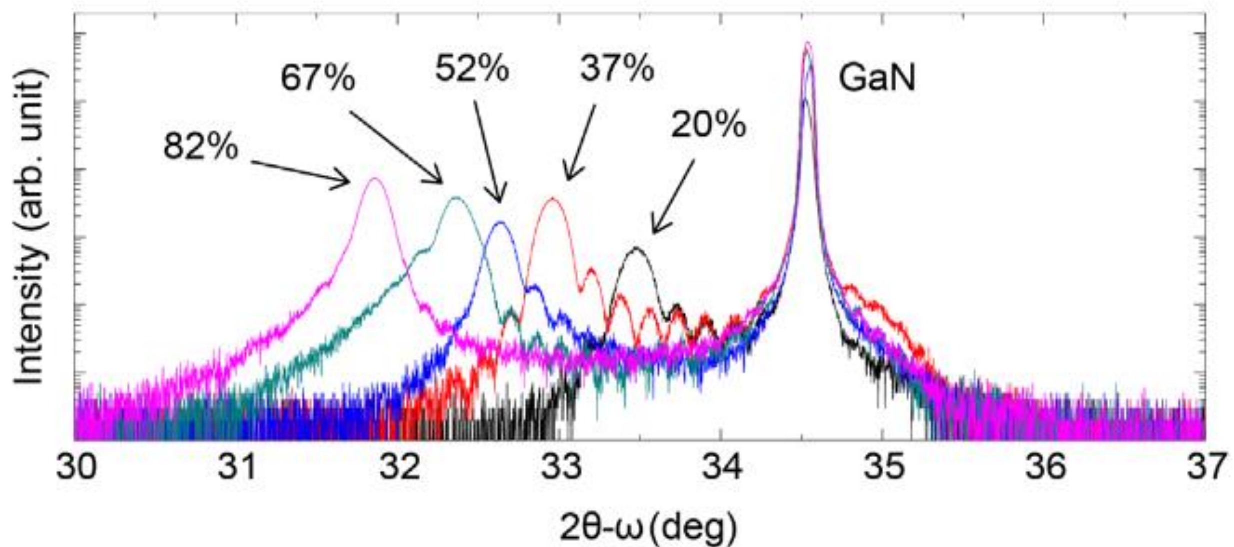

Figure 1.3: XRD 2θ-ω curves showing high quality InGaN grown over the entire composition range with MME.[34]

The improvement of films and doping via MME can be explained by enhanced growth kinetics. Two scenarios can be invoked to explain the improvement well: the growth of InGaN via MME; and Mg incorporation in GaN during MME growth. InGaN is a traditionally difficult material to grow. Several issues plague the material, such as a large lattice mismatch between the two binaries GaN and InN, a large difference in adatom diffusion rates between Ga and In, and In-N bond decomposition and In desorption at high temperatures.[23,24] As a result, InGaN has a

tendency to phase separate during growth and even when it doesn't, a high defect density is often observed unless the films are close in composition to either of the binaries. MME can mitigate the issues of divergent diffusion rates and thermal decomposition/desorption via low temperature, metal rich growth. Diffusion rates are controlled exponentially by temperature, but also by the energy of the diffusion barrier.[35] As a result, metal rich growth can replace the strong semiconductor bonds with weaker metal bonds, reducing the energy of the diffusion barrier and enhancing adatom mobility even at low temperatures, mitigating phase separation and surface segregation issues in InGaN.[36] Thermal desorption is also a challenge in the incorporation of Mg in films.[26] MME has demonstrated high Mg incorporation at the low temperatures facilitated by its metal rich nature. MME has further potential to improve AlGaN and AlInN growths.

Another challenge that has plagued the III-Nitride material system is the efficient p-type doping of the material. III-Nitrides typically have an intrinsic background donor level of 10^{16} to 10^{19} cm^{-3} which results in great difficulties in doping.[37] The most widely studied p-type dopant is magnesium and the most studied III-Nitride for p-type doping is GaN. Mg doping of GaN faces multiple challenges, such as a high activation energy and self-compensation by the formation of donor like defects. In traditional growth Mg has a high activation energy in GaN of about 170 meV which often leads to very low acceptor activation efficiencies, however, recently the MME technique demonstrated a great improvement in Mg doping of GaN, showing an activation energy of 43 meV and an acceptor ionization efficiency of 52%.[38] Even worse is the activation energy of Mg in AlN, which is as high as 510 meV.[39] A challenge that MOCVD faces in Mg doping is hydrogen passivation of acceptors due to the hydrogen used in the carrier gasses in MOCVD. This is resolved by a post growth anneal, however it makes it difficult to achieve buried p layers as hydrogen cannot diffuse through n layers.[40] Mg, in all growth methods, will also begin to self-

compensate if the concentration of acceptors is too high. Mg will form point defects as Mg interstitials in the GaN crystal, which combined with nitrogen vacancies will cause severe compensation of acceptors and reduce the Mg activation efficiency.[41,42] Mg can even precipitate in pyramidal defects and become electrically inactive.[43] As a result of these issues the Mg doping of GaN has been limited. Typical values for hole concentration in GaN range from 10^{17} to the low 10^{18} cm^{3} range and observed efficiencies for Mg activation range from 10% to below 1%.[44–47] MME however has achieved p-type GaN with hole concentrations exceeding $6x10^{19}$ cm^{-3} with significantly higher activation efficiencies.[28]

1.3 Optoelectronic Development and Applications

The material that allowed the III-Nitrides to jump into its dominant place in the solid-state lighting field and make strong advancements in the photovoltaics field was InGaN. For a long time InGaN was difficult to grow due to the material parameter differences between the two binary components, GaN and InN, and the energetics of the ternary. InN has an interatomic spacing in the a-plane of 3.56 Å and GaN has an interatomic spacing of 3.19 Å in the a plane. As a result of these differences, a large miscibility gap exists for this ternary.[48] Within this miscibility gap it is more energetically favorable for growth to occur in two phases rather than one, resulting in the phase separation of the ternary from a single phase into multiple phases similar to what is observed in Figure 1.4.[49–52] Now while it has been shown that some phase separation can actually be beneficial to LEDs by creating areas of lower bandgap materials that localize carriers away from Non-radiative Recombination Centers (NRCs), enhancing radiative recombination, when InGaN is grown thick with this phase separation occurring, defects are generated that can harm solar cell performance. [53–56] While MOCVD has been able to grow high quality InGaN with a low indium content, it struggles to grow with higher indium content due to high decomposition of In-N bonds

and In desorption at elevated temperatures. It has been shown that indium incorporation efficiencies decrease by more than half when increasing the growth temperatures from 800 to 840°C.[57] On the other hand, PAMBE has been able to demonstrate the growth of InGaN over the entire composition range at low growth temperatures.[24,34,36,58–60] Despite the strong ability of PAMBE to grow InGaN, it faces a problem that other growth techniques do not in the form of plasma damage. It has been shown that ionic species within the plasma during MBE growth can cause damage and defect formation within indium bearing films and can even damage GaN and thus, must be controlled.[14,61,62]

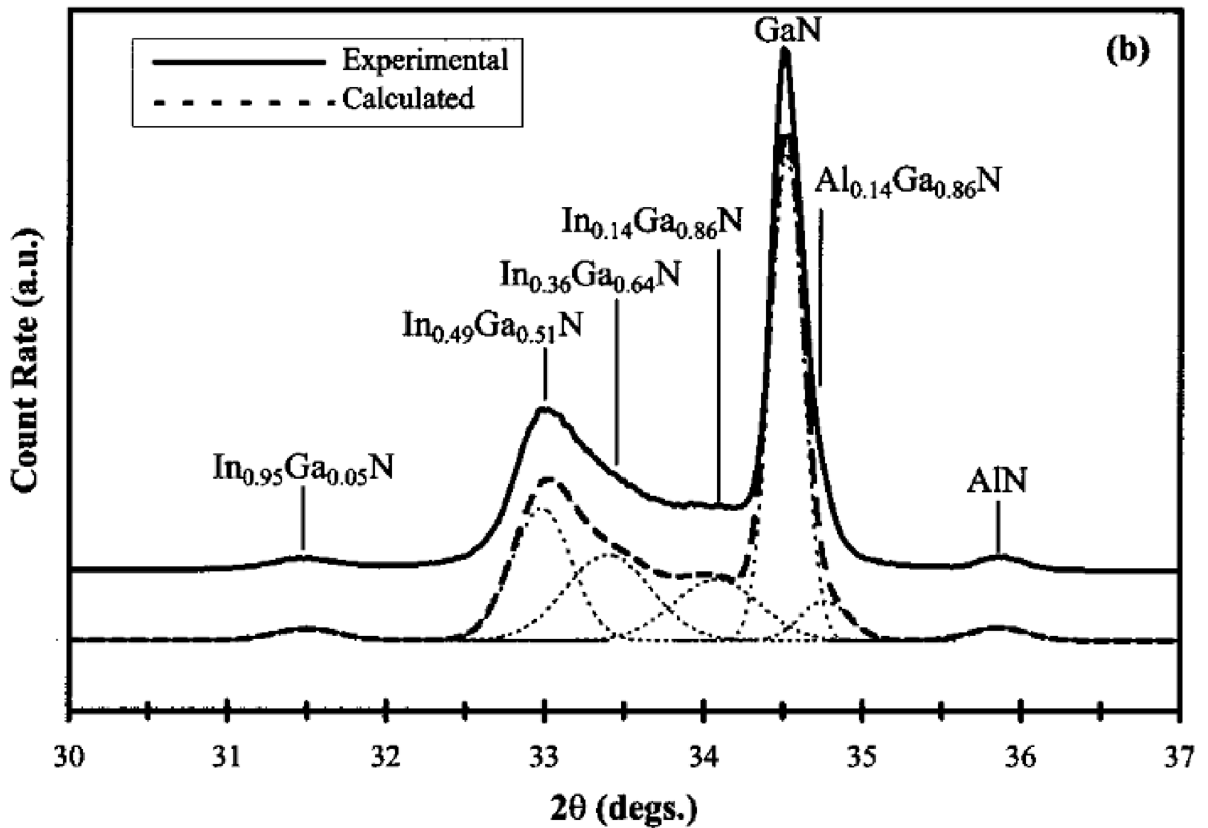

Figure 1.4: XRD 2θ-ω curve of phase separated InGaN.[52]

An additional benefit of PAMBE in the growth of InGaN is the precise control of metal adlayer accumulation for growth kinetics engineering. One method to improve the indium incorporation in the film is to grow in the nitrogen rich regime. In this regime the amount of active nitrogen supplied to the surface of the growing film is greater than that of the supplied metal flux. The excess of active nitrogen will quickly capture metal atoms hitting the surface and will mitigate the effects of decomposition and desorption. This, however, has been shown to cause low adatom mobilities and causes rough surface morphologies.[63] Even further exacerbating the problem is the fact that adatom mobilites are reduced at low growth temperatures, leading to a further deterioration of crystal quality.[64] Adatom mobility can be enhanced during InGaN growth by building up an adlayer of In and Ga atoms on the surface of the film during growth, as is done during MME growth, however building up more than a monolayer of metal can cause phase separation. It is the use of this surface adlayer that has allowed for the enhanced growth of InGaN films over the entire composition range at low temperatures in PAMBE.[23]

Another ternary alloy in the III-Nitride material system that shares many of the challenges of InGaN growth but is still in its infancy relative to InGaN and AlGaN, is AlInN. AlInN has been a topic of recent study due to its ability to be lattice matched to GaN at a composition of ~18% indium,[65] making it a strong candidate for power electronics, as a strain-free barrier layer on GaN in a high electron mobility transistor,[66] and optoelectronic applications such as distributed Bragg reflectors,[67,68] electron blocking layers,[69] and even AlInN/GaN multi quantum wells.[70] An area that has been largely unexplored thus far is the application of AlInN for photovoltaics. AlInN has a tunable, direct bandgap from 0.65 to 6.1eV spanning from the infrared to the ultraviolet wavelengths, including the entire visible and solar spectrum. With high indium content, AlInN can achieve a bandgap of 1.7eV, which is the optimal bandgap for a double junction tandem solar cell

with silicon.[71] However, many challenges exist when growing AlInN. One challenge is due to the large lattice mismatch between the binaries, AlN and InN, resulting in a large miscibility gap, greater even than InGaN, for the ternary.[72] In addition, the optimal growth substrate temperature for growth of InN is significantly lower by about 500° C than that of AlN. At the low temperatures required to incorporate indium into the crystal the aluminum adatoms have a low surface mobility, often leading to poor crystal quality.[64] Conversely, it has been reported that ifhigher temperatures or excessive metal surface coverage are used, the increased surface diffusivity results in enhanced phase separation driven by natural spinodal decomposition, similar to InGaN.[36,73] For these challenging reasons, high indium content AlInN has seen relatively few advances. Phase separation is commonly seen in the AlInN material in the form of a 'honeycomb' like structure illustrated in Figure 1.5.[74–76] In this structure the material phase separates into 'honeycombs' with indium depleted cores and indium rich walls that propagate vertically during growth. MBE[77,78] and metal organic vapor phase epitaxy (MOVPE)[79–83] have been utilized for epitaxy studies while sputtering techniques have been used to grow high indium content AlInN for solar applications.[18,84–86] However, all previous attempts have faced issues of poor crystallinity in compositions away from the lattice matched point. The advantages of growth kinetics control in low temperature MME growth with a controlled metal adlayer could perhaps be applied to grow high quality, indium rich AlInN.

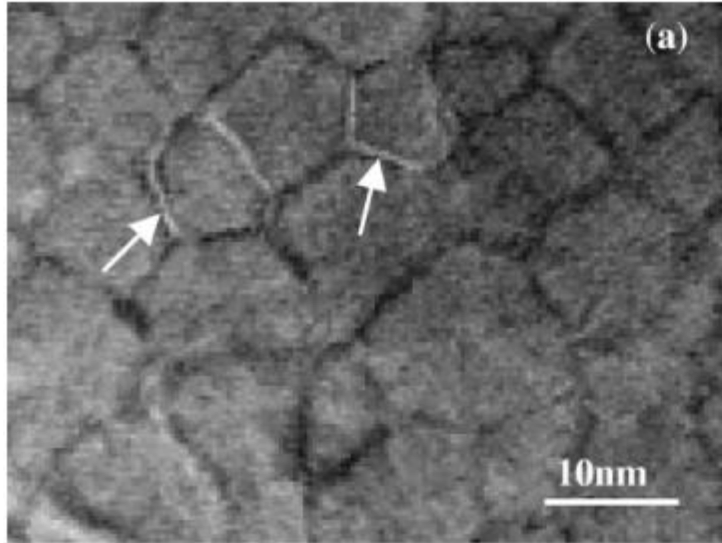

Figure 1.5: Plan-view electron micrograph image of a honeycomb structure in an AlInN film.

Advancements in III-Nitride growth have allowed the III-Nitrides to shoot into the forefront of the LED industry. Advancements in InGaN/GaN quantum well (QW) and multi quantum well (MQW) structures have allowed the development of high efficiency green and blue LEDs, and AlGaN/GaN structures have allowed the same for UV LEDs.[8–11] It was surprising to the field that high efficiency LEDs were even possible given the high dislocation density in III-Nitride materials. A dislocation density of 10^{10} cm^{-2} would have rendered an LED useless in the arsenide or phosphide material system, yet it didn't seem to hamper III-Nitride LEDs. There has been much debate and study in the field on why dislocations seem irrelevant to efficiency. It has been shown that some small phase separation in InGaN/GaN MQWs can form areas of carrier localization that trap carriers away from the NRCs at threading dislocations. Another largely abandoned but not disproven idea is that due to the inherent polarization due to the wurzite structure of the III-Nitrides that band bending occurs at dislocations, making it energetically unfavorable for carriers to enter these NRCs.[53–56] While these unique properties of III-Nitrides allow for the creation of efficient LEDs even with high dislocation densities, there are still

challenges plaguing III-Nitride LEDs. A common phenomenon in these LEDs is efficiency droop. Efficiency droop is defined as a reduction in light output efficiency with increasing current injection as shown in Figure 1.6.[87] This has been attributed to multiple factors, including asymmetric carrier injection due to the low hole concentration and mobility in the p layers of the LED and the leakage of carriers out of the active region due to a form of Auger recombination at high current densities.[88–91] Many steps have been taken to reduce the NRCs present in the LEDs and reduce efficiency droop. These include InGaN underlayers to trap and eliminate dislocations and defects and various layers to improve hole injection into the active region and reduce carrier overflow out of the active region.[92–101]

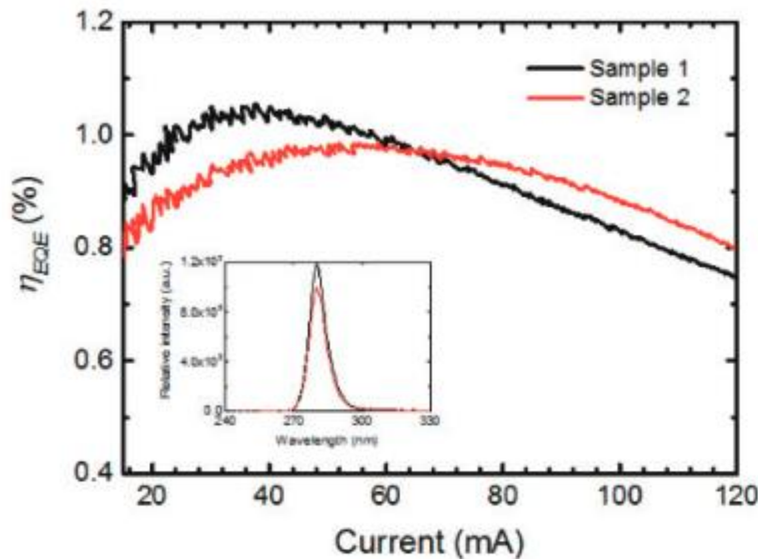

Figure 1.6: EQE vs current for an AlGaN LED showing efficiency droop with increased current.[87]

The III-Nitride material system also is at the forefront of the solid state UV emission field thanks to AlGaN. AlGaN has a bandgap ranging from 3.4 to 6.1 eV depending on composition. Thanks to this bandgap range, emission with the material can cover from the UVA range to deep

in the UVC range. This has allowed for the fabrication of high efficiency UV LEDs over a wide range of emission wavelengths, although the efficiency is rapidly reduced as the wavelength is pushed deeper into the UV range.[9,102–104] This is illustrated in Figure 1.7 where it is observed that reducing the emission wavelength from 300 to 260 nm sees a drop in EQE of over 70%.[105] Further decrease in emission wavelength has observed to cause a further, exponential, drop in EQE for AlGaN-based UV LEDs.[9] This loss in efficiency is driven by a number of compounding factors. One, intrinsic to the material system, is the lack of a native substrate for the AlGaN films. Lattice mismatch between the AlGaN layers needed for the UV LEDs and the underlying template, typically AlN or GaN, results in defect generation within the LED structures, leading to the generation of non-radiative recombination centers that greatly reduce light output from the devices.[105] Another issue is the poor efficiency of doping for the AlGaN films. Shifting the composition from GaN towards AlN results in a substantial increase in activation energy for the dopants commonly used for III-Nitride materials (Mg, Ge, and Si for example), resulting in poor carrier concentrations within the AlGaN films leading directly to reduced concentration of electron hole pairs for radiative recombination.[32,102] Recently, great success has been demonstrated in the doping of AlN with Be for p-type and Si for n-type material, but this success has not yet been translated to AlGaN.[106] This doping issue indirectly causes a third issue plaguing the development of deep UV LEDs in parasitic absorption of emitted light. Due to the poor doping efficiency of AlGaN, GaN is commonly used as a contact layer to improve carrier concentration within the devices. However, since GaN has a lower bandgap than the energy of the light emitted by an AlGaN UV LED, a portion of the emitted light will be absorbed by these GaN contact layers, reducing the total light output from the device.[32,102,107] This results in a loss in EQE for all UV LEDs utilizing such contacts, not just devices operating in the deep UV range. A final issue

hampering the efficiency of all AlGaN-based UV LEDs is the previously discussed phenomenon of efficiency droop.[87] While the mechanisms behind this effect are identical to what was previously discussed for InGaN based LEDs, this effect is worsened in deep UV LEDs due to the poor injection efficiency of carriers resulting from poor doping efficiency. All these challenges remain to be overcome and even small improvements in any of them can result in great increases in EQE for AlGaN-based UV LEDs.

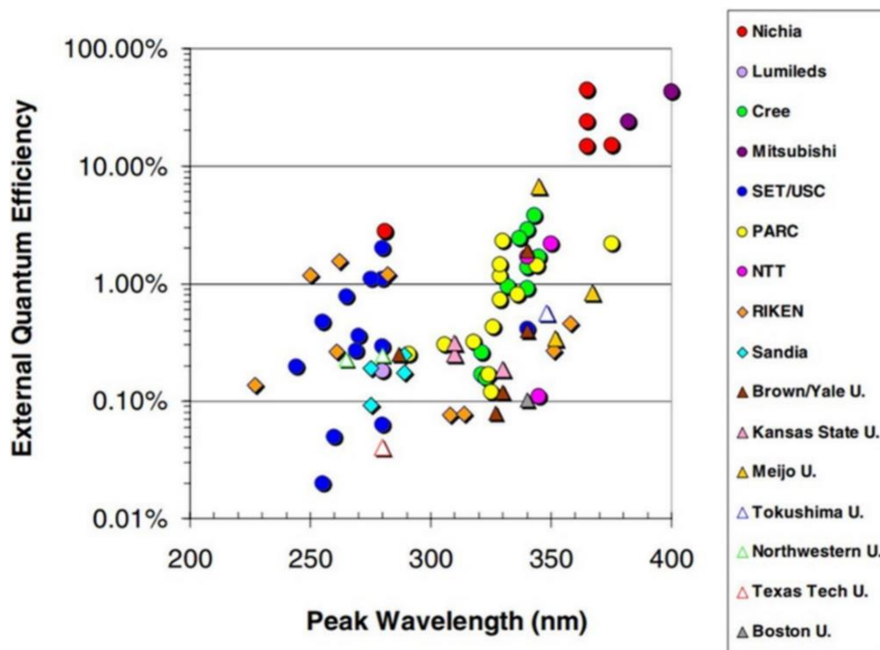

Figure 1.7: EQE Vs. Wavelength for AlGaN-based UV LEDs.[105,108]

White light can be generated in multiple ways, one of which is the fabrication of a RGB LED that when all three colors are driven together produce white light. The most common method of producing white light is using a high energy (blue-UV) LED to excite a phosphor and produce a color spectrum that emits as white light.[109,110] The III-Nitride system has had little success in creating monolithic RGB LEDs as despite the success of green and blue LEDs, red emitting devices have thus far been low efficiency.[111–113] The low efficiency has been largely attributed to

poor material quality. In order to achieve red emission InGaN would have to have an indium composition of ~40%, which is well within the miscibility gap of the material and growth of this composition is defective, leading to many NRCs and reduced device efficiency. AlInN also possesses the potential to be used for red emission, or any other color as its bandgap can span from 0.65 to 6.1eV, but this ternary alloy has received very little study and is in its infancy relative to the rest of the III-Nitride family.[114]

1.4 III-Nitride Photovoltaics

The III-Nitride material system has also generated interest in photovoltaic applications. Due to the bandgap range of the system, nearly all the ideal bandgaps for a multi junction solar cell can be achieved in a single material system.[115] Unfortunately, so far III-Nitride solar cells have been limited to low efficiencies.[31,116–119] InGaN has been the focus of study for solar cells as it can achieve the ideal bandgap for a single junction solar cell of 1.35 eV at a composition of 62% indium.[120] It could even achieve the ideal bandgaps for a triple junction solar cell of 0.67 eV, 1.4 eV, and 1.85 eV.[121] Unfortunately, the high indium content required to achieve these bandgaps causes the generation of many defects that reduce solar cell performance. Thick growth of high indium content InGaN also causes degradation in material quality which limits the thickness of the absorbing layer and further reduces the efficiency of the cells.[122–125] AlInN has also received some study in the photovoltaic field as it can achieve the same bandgaps as InGaN, but can achieve them at compositions further from the miscibility gap. AlInN has been grown atop various substrates to study is photovoltaic properties, but efficiencies haven been similarly low, only going as high as 2.5% for an AlInN on p-Si solar cell.[18,84,85] AlInN thus far has been an understudied material for optical devices and photovoltaics, despite its desirable properties. Further study and improvement

of the material via growth kinetic engineering could yield improvement in III Nitride LED and solar cell performance.

1.5 Application of III-Nitrides Towards Power Electronics and RF Transistors

A new III-nitride alloy that has gained great attention in recent years is ScAlN. The attention to this alloy has been caused by its high spontaneous and piezoelectric polarization and its ferroelectric properties, in addition to the fact that ScAlN has been reported to be lattice matched to GaN at a composition of ~18-20% Sc.[126–131] Due to the immense spontaneous polarization coefficients of the alloy, even in the case of being lattice matched to GaN where piezoelectric polarization will have no effect on the sheet charge, 2D electron gas (2DEG) densities as high as ~$6x10^{13}$ cm^{-2} have been predicted in literature and approached in experiment.[127,132] Figure 1.7 displays the calculated interface sheet charge generated due to polarization at various III-Nitride interfaces showing a significantly higher value for ScAlN over other materials in a wide composition range. Thanks to these favorable properties, a number of $Sc_xAl_{1-x}N$/(AlN)/GaN HEMT structures (parenthesis indicating optional AlN interlayers) have been demonstrated, achieving sheet resistances as low as 167 Ω/□ and mobilities as high as 1556 cm^2/vs.[132–136] Since ScAlN is primarily grown nitrogen rich and thus tends to roughen, most of the larger electrical mobility structures utilize an AlN and/or AlGaN interlayer that provide smooth interfaces while, in the case of AlN, minimizing random alloy scattering. A number of growth issues have plagued the alloy that must be overcome to achieve the theoretical potential of the system. Previously, ScAlN was deposited via radio frequency (RF) sputtering, which often yielded material that was polycrystalline and/or contained a high defect density, degrading device performance.[137–141] In recent years, nitrogen-rich MBE of single phase ScAlN has been demonstrated with improved crystal quality, allowing for HEMT properties to be advanced.[135,136] However, a challenge still

remains in MBE of ScAlN in the form of metal rich growth which is the preferred chemistry for MBE, providing enhanced atom surface diffusion. In traditional III-Nitride MBE, metal rich chemistry has led to an improvement of crystal quality, surface roughness, and interface roughness.[24,142–145] Due to multiple intermetallic Al_xSc_y phases being thermodynamically stable under metal rich conditions, thus far, attempts to grow ScAlN under these metal rich conditions have, lead to the inclusion of unintended metal and even rock salt phases.[132,135,146] Adding additional complication, the phase transition of ScAlN from wurtzite towards rock salt has been reported to occur around 40% Sc. Metal rich ScAlN has been investigated using Ga as a pseudo-surfactant but since Ga is soluble in ScAlN at all achievable growth conditions, Ga will incorporate into the films creating a ScAlGaN alloy.[147] Thus, pure phase ScAlN grown under the generally preferred metal rich condition has been elusive.

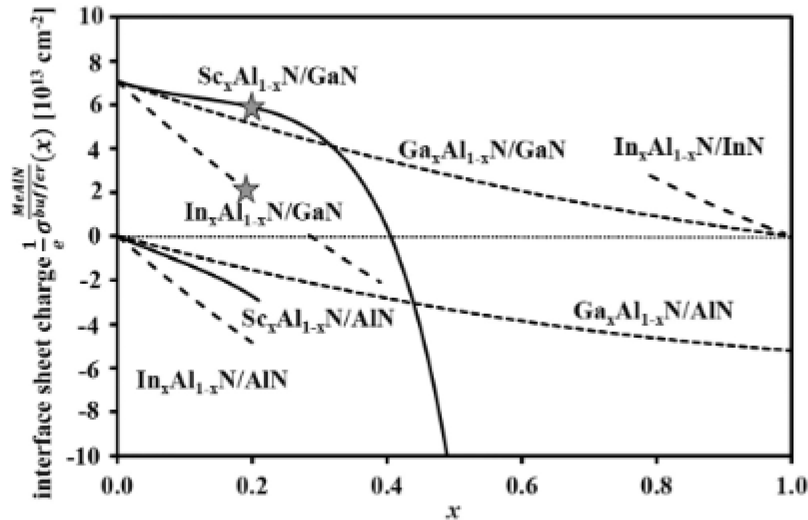

Figure 1.8: Polarization generated interface sheet charge for various III-Nitride heterostructures.126

A transition to metal rich growth of single phase, high quality ScAlN films will lead to a number of advantages and improvements in the performance of devices. A significant, noteworthy

improvement would be the reduction of interface roughness induced scattering to improve the mobility of the 2DEG generated at the interface of a ScAlN/GaN interface .[148–151] The use of ScAlN directly in contact with GaN could forgo the screening of the beneficially large ScAlN polarization by the less polar AlN or AlGaN. It is worth noting that the work of Frei *et al.* achieved close to the theoretical value of 2DEG density by not using an interlayer.[132] However, thus far no report of successful metal rich, phase pure growth has been reported for this alloy system.

Of the predominant III-Nitride epitaxy techniques, only molecular beam epitaxy (MBE) seems to have the potential to grow ScAlN under metal rich conditions. Metal organic vapor phase epitaxy typically uses heavily nitrogen rich growth for III-Nitride epitaxy, and faces the added issue of a lack of suitable precursors for Sc. Due to the poor volatility of Sc precursors, thus far ScAlN films have been limited to a maximum Sc content of ~30% and to even achieve such a concentration custom modifications to the chamber were needed and growth is limited by rates far slower than what can be achieved for other III-Nitride alloys.[152] Utilizing standard or high temperature effusion cells, MBE reactors are capable of producing the Sc fluxes required to grow under metal rich conditions. However, previous MBE studies of metal rich growth of ScAlN have demonstrated the inclusion of metallic or rock salt phases. Hardy *et al.* utilized traditional MBE of $Sc_{0.18}Al_{0.82}N$ over a range of III/V ratios, but observed that as the III/V ratio increased and approached stoichiometry and transitioned into metal rich, phase separation was observed in X-Ray Diffraction including intermetallic inclusions and what was theorized as rock salt phases.[135] Frei *et al.* utilized an alternating Al then Sc cyclic pulsed metal technique in MBE, but observed much the same.[132] However, neither study implemented a scheme to control the buildup of surface metal, likely enhancing phase separation as has been reported in other ternary III-Nitride materials.[153]

CHAPTER 2. APPLICATION OF LOW TEMPERATURE, METAL RICH GROWTH FOR IMPROVEMENT OF TRADITIONALLY DIFFICULT $AL_{0.3}IN_{0.7}N$ FILMS

2.1 Introduction

AlInN has been a topic of recent study due to its ability to be lattice matched to GaN at a composition of 18% indium, making it a strong candidate for power electronics as a strain-free barrier layer on GaN in a high electron mobility transistor[66] and optoelectronic applications such as distributed Bragg reflectors[67] and electron blocking layers.[69] An area that has been largely unexplored thus far is the application of AlInN for photovoltaic applications. AlInN has a tunable, direct bandgap from 0.65 to 6.1eV spanning from the infrared to the ultraviolet wavelengths, including the entire solar spectrum. With high indium content, AlInN can achieve a bandgap of 1.7eV, which is the optimal bandgap for a double junction tandem solar cell with silicon.[71] However, many challenges exist when growing AlInN. One challenge is due to the large lattice mismatch between the binaries, AlN and InN, and thus a large miscibility gap exists for the ternary.[72] In addition, the optimal growth substrate temperature for growth of InN is significantly lower than that of AlN in molecular beam epitaxy (MBE). At the low temperatures required to incorporate indium into the crystal the aluminum adatoms have a low surface mobility, often leading to poor crystal quality.[64] Conversely, when higher temperatures or excessive metal surface coverage are used, the increased surface diffusivity results in enhanced phase separation driven by natural spinodal decomposition, similar to InGaN.[36,73] For these challenging reasons, high indium content AlInN has seen relatively few advances. MBE[77,78] and metal organic vapor phase epitaxy (MOVPE)[79–81] have been utilized for epitaxy studies while sputtering techniques have been used

to grow high indium content AlInN for solar applications.[18,84–86] However, all previous attempts face the same issues of poor crystallinity and rough surfaces as tabulated in Table 1.

The metal modulated epitaxy (MME) growth technique offers an encouraging alternative to circumvent the traditional issues when growing AlInN. This flux modulated technique utilizes metal-rich surfaces to enhance the adatom kinetics even at low growth temperatures, where the thermal contribution to the diffusion length is low. Additionally, a nitrogen plasma in PAMBE provides active nitrogen species even at low growth temperatures that would normally be insufficient to thermally disassociate nitrogen compounds in other techniques, such as ammonia-based MBE and MOVPE. As a result, plasma-assisted MME permits growth temperatures sufficiently cold to improve indium incorporation by preventing unwanted decomposition, while still giving enough control over the adatom kinetics to improve diffusion lengths and improve film quality.

2.2 Experimental

All films in this study were grown in a Riber 32 MBE reactor using the MME technique, the details of which are similar to those for InGaN and can be found elsewhere.[24] All samples were grown on 1x1 cm semi-insulating MOVPE-grown GaN-on-sapphire templates. The substrates were single-side polished and 2 μm of tantalum was sputtered on the backside to facilitate uniform heat conduction during growth. Prior to growth the substrates were cleaned using a 3:1 solution of H_2SO_4:H_2O_2. This clean was followed by a rigorous rinse with DI water and a brief dip in dilute HF to reduce surface oxides, after which the sample was again rinsed with DI water and dried with N_2. After the chemical cleaning procedure, the samples were loaded into an introductory vacuum

chamber in which they were outgassed at 200 °C for 20 minutes. Prior to growth, the samples were further outgassed at 650 °C for 10 minutes in the growth chamber.

During growth, all metal fluxes were provided by conventional effusion cells. Nitrogen was provided by a Veeco UNI-Bulb radio frequency (RF) plasma source with an RF power of 350 W and a gas flow of 2.5 sccm. A 100nm GaN layer was grown prior to the AlInN layer using MME for all samples and is described elsewhere.[154] The AlInN films were grown using MME with a metal rich III/V ratio of 1.3. The shutter cycle consisted of a repeated 2.1 s open and 2.1 s closed cycle for both the In and Al shutters simultaneously with a constant nitrogen plasma impinging on the surface during both the open and the closed metal cycles. This shuttering scheme was designed to limit the metal adlayer buildup to 1 monolayer and limit phase separation. This approach is similar to a previous work limiting phase separation in InGaN and AlGaN.[24,155] The substrate temperature for the AlInN film growth was varied from 300 to 425 °C. These temperatures are below the In desorption temperature in our system and will achieve full indium incorporation into the film. Additionally, with the absence of desorption and the constant supply of nitrogen, the growth rates and accumulated metal adlayer thickness in all cases are the same, limited to 1 monolayer. All of the MME-grown AlInN layers had a thickness of 100 nm and metal fluxes were selected to achieve a target composition of 70% indium. At low growth temperatures, the target composition matched the measured actual composition due to full indium incorporation.

In situ surface monitoring was performed using reflection high energy electron diffraction (RHEED) and post-growth x-ray diffraction (XRD) analysis was performed with a Philips X'pert Pro MRD. The XRD used a Cu anode and the Kα1 incident beam was monochromated by a hybrid Ge crystal and mirror. Photoluminescence (PL) measurements were taken using a Renishaw Qontor dispersive Raman spectrometer at room temperature (RT) using a 50 mW 488 nm laser

operating at 1% power. Surface morphology was analyzed using a Veeco Dimension 3100 atomic force microscope (AFM).

2.3 1.3 Results and Discussion

2.3.1 Establishment of Epitaxy Conditions

Critical to the development of growth conditions for AlInN, or any In bearing III-Nitride, is overcoming the thermal decomposition of In-N bonds. This decomposition occurs at relatively low temperatures and is expected to happen in a relatively low temperature range of 400 to 500 ^{o}C. In a method of growth like MOCVD, where substrate temperatures of 1000 ^{o}C or higher are commonly used, this thermal decomposition is mitigated with an enormous nitrogen over pressure, supplying the growth surface with enough reactive nitrogen that In-N bonds will reform as soon as they break. This in combination with an excess supply of In atoms to compensate for evaporation of In from the surface allows for MOCVD to successfully grow InGaN and AlInN, despite extremely high growth temperatures. MBE however can overcome this differently. Due to the nitrogen source in MBE being a plasma source, reactive nitrogen can be supplied to the growth surface without the requirement of thermal cracking of molecules. As a result, growth temperatures below the In-N decomposition regime can be used.

As growth conditions can vary between MBE reactors based on a multitude of factors, it is necessary to calibrate the conditions in our experimental setup. To facilitate this, a series of AlInN films were grown over a range of substrate temperatures from 550 to 425 ^{o}C. For these films a III/V ratio of 0.9 was used to prevent the accumulation of metal adlayers and an equal amount of Al and In flux was used, resulting in an $Al_{0.5}In_{0.5}N$ film when all In is incorporated into the film. Figure 2.1 shows the indium incorporation percent vs growth substrate temperature for the films.

The indium incorporation increases linearly with decreasing substrate temperature, interpolating to a substrate temperature of 420 ºC for 100% indium incorporation efficiency. As a result, in order to overcome thermal decomposition of In-N bonds and ensure full indium incorporation, a substrate temperature below 420 ºC must be used in the reactor. This is an invaluable calibration for future development of AlInN growth.

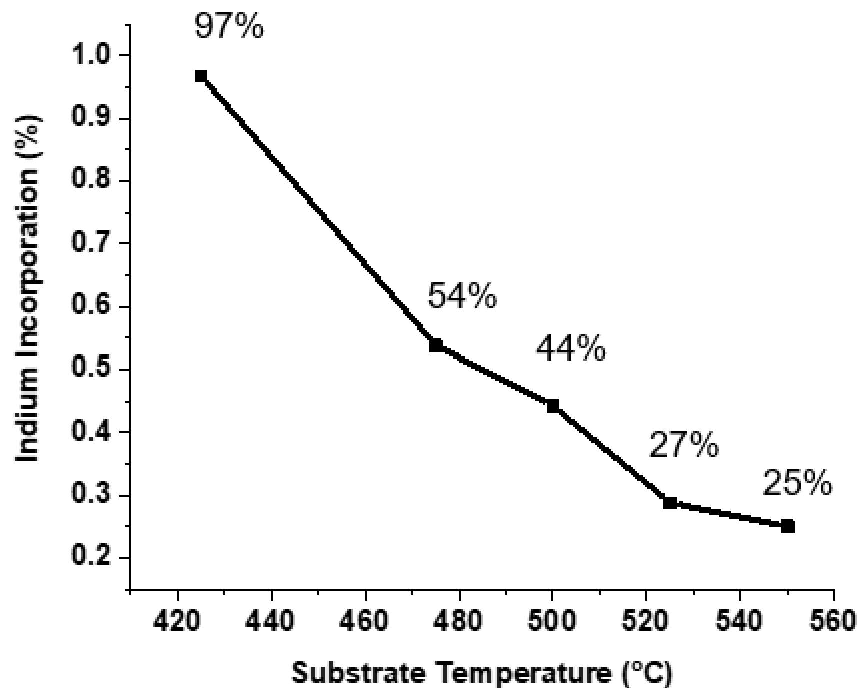

Figure 2.1: Indium incorporation vs. substrate temperature for AlInN growth.

With the substrate temperature requirements established, the next step was to move on to the target composition of $Al_{0.3}In_{0.7}N$. Using a substrate temperature of 375 ºC, selected well below the established 420 ºC limit established to avoid In-N bond decomposition, the flux ratios were adjusted and an $Al_{0.3}In_{0.7}N$ film was grown with a III/V ratio of 0.9. Figure 2.2 displays the 2θ-ω scan of the resulting sample. The film had a content of 76% In, likely the result of an error in flux conditions, but was single phase and had XRD figures of merit of 783 arcsec for the (0002) rocking

curve and 2456 arcsec for the (10-15) plane, suggesting good crystal quality, but showing room for improvement.

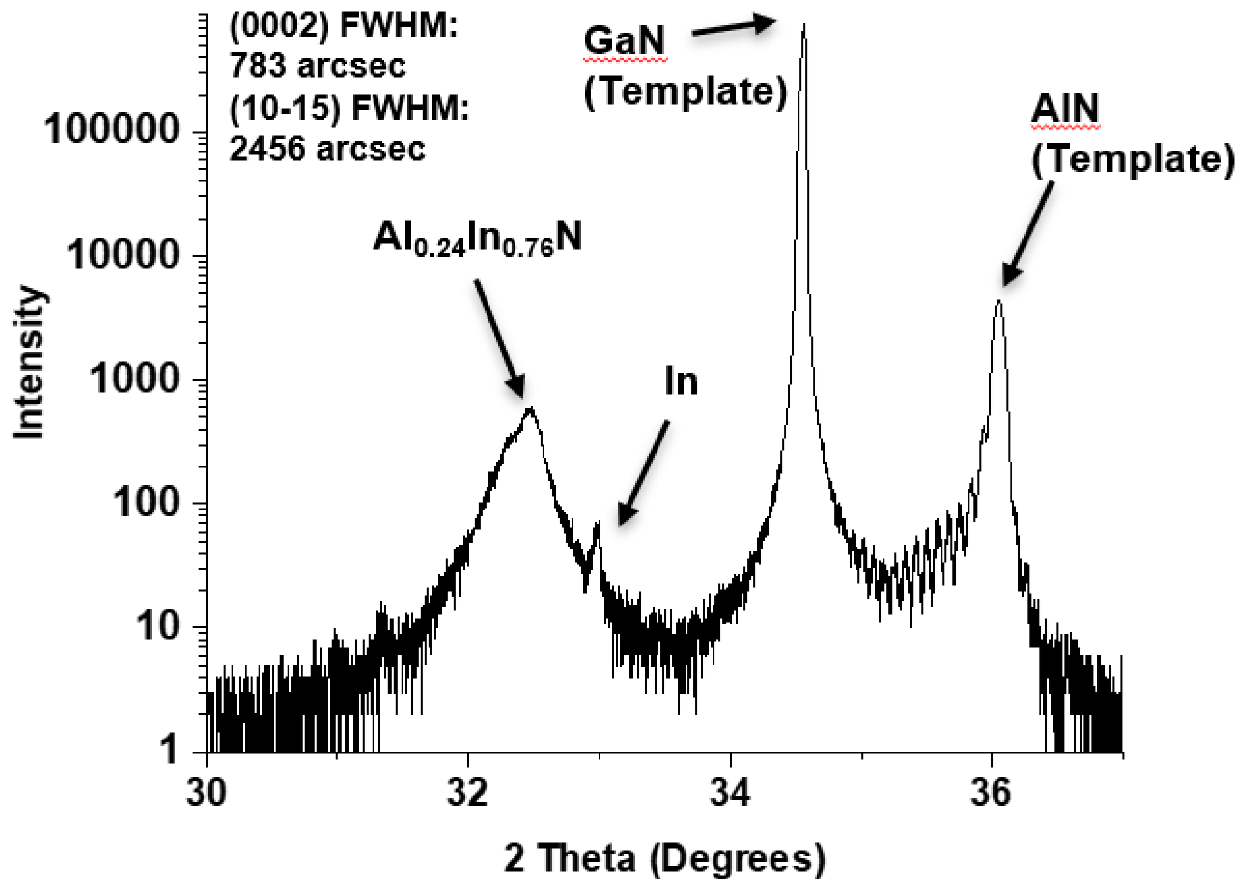

Figure 2.2: XRD 2θ-ω curve of nitrogen rich AlInN grown with established initial conditions.

2.3.2 Establishment of MME Conditions

With initial growth conditions for $Al_{0.3}In_{0.7}N$ being established, further development must happen to transition to metal rich, MME growth of the alloy. Previous observations for both InGaN and AlGaN have demonstrated that uncontrolled accumulation of surface metal results in severe phase separation or surface segregation. Figure 2.3 shows an example of this in the case of InGaN.

In this case the surface accumulation of metal was controlled via dose, with figure a using a high dose and figure b using a low dose. It is clearly seen that utilizing a high dose for InGaN growth results in degradation of surface and crystal quality, as well as phase separation. All of these factors are mitigated by reducing the metal dose resulting in improvement in all structural properties.

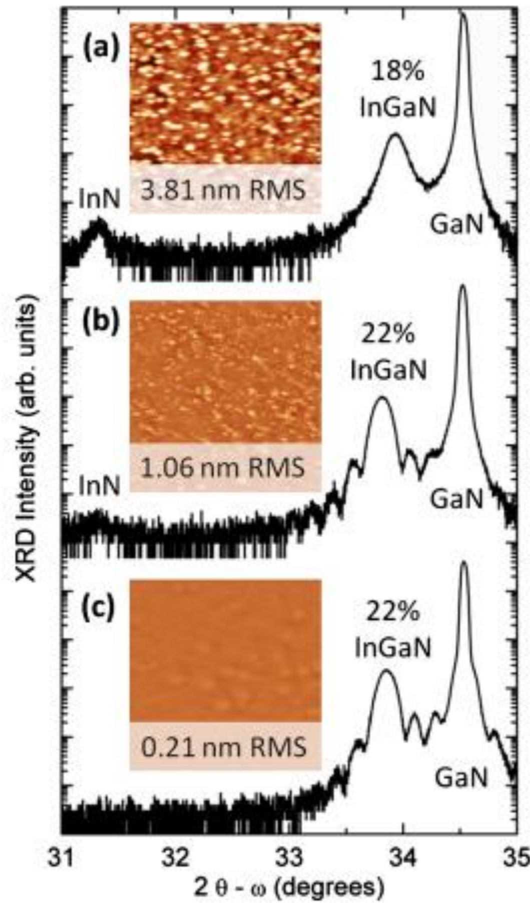

Figure 2.3 XRD scans of single phase InGaN grown with the MME technique.[156]

The same principal used in InGaN and AlGaN MME growth is applied to AlInN. In a method similar to previous work within the Doolittle group by Moseley *et al.* RHEED analysis was performed on AlInN to determine the metal dose necessary to limit metal accumulation to a single monolayer. In a RHEED transient, constructive and destructive interference results in

oscillation of intensity. A complete layer will have the highest RHEED intensity due to constructive interference, while a partial layer will see a dimming of the RHEED due to destructive interference. Thus, when metal accumulates on the surface an initial drop in RHEED intensity will be observed, reaching a minimum at half surface coverage, followed by a rise in intensity as the first monolayer of metal is formed and reaching its peak intensity with a complete monolayer of metal. Immediately following will be a drop in intensity as a second monolayer of metal begins to form. By studying this RHEED oscillation one can find the time difference between the initiation of the metal dose and the completion of the first monolayer of metal. In the case of $Al_{0.3}In_{0.7}N$ with a III/V ratio of 1.3, this was determined to be 2.1 seconds. With all growth conditions now being found, MME was applied to grow 100 nm of $Al_{0.3}In_{0.7}N$. Figure 2.4 displays the XRD 2θ-ω curve of the AlInN film. While the composition was slightly off target, the AlInN XRD peak displays a significantly narrower peak and greatly improved figures of merit compared to the film grown under nitrogen rich conditions, with an improvement of over 4x for the (0002) FWHM. It should be noted that both an In metal and InN show up in the curve as well. This is the result of surface decomposition post growth. During cooling of the sample once growth is finished, surface bonds can decompose, especially in the presence of an energetic plasma. While no metal is hitting the surface at this time, the nitrogen plasma is still active on the surface. As a result, some of the decomposed In-N bonds with reform as InN on the surface, leaving a mixture of In metal and InN. Additional improvement compared to the N-rich case is observed in the surface roughness, shown in Figure 2.5. Nitrogen rich growth of AlInN yielded a surface RMS roughness of 1.5 nm, but transitioning to MME growth resulted in a decrease in surface roughness to 0.88 nm. Table 2.1 shows a comparison of XRD figures of merit for the MME grown AlInN film vs others in literature

at a similar composition. It can be seen that using MME to grow high In content AlInN yields an improvement in XRD (0002) FWHM of more than 11x compared to other previous reports.

Table 2.1 XRD figures of merit comparing the MME grown film and previous reports in literature for similar compositions.

Author	Technique	Substrate	(0002) FWHM (arcsec)
This Work	MME	GaN:Fe on Sapphire	135
Núñez-Cascajero	RF Sputtering	Sapphire	5040
Terashima	MBE	N-Polar GaN	2700
Hums	MOVPE	GaN on Si	3570
Kang	MOCVD	Sapphire	1692

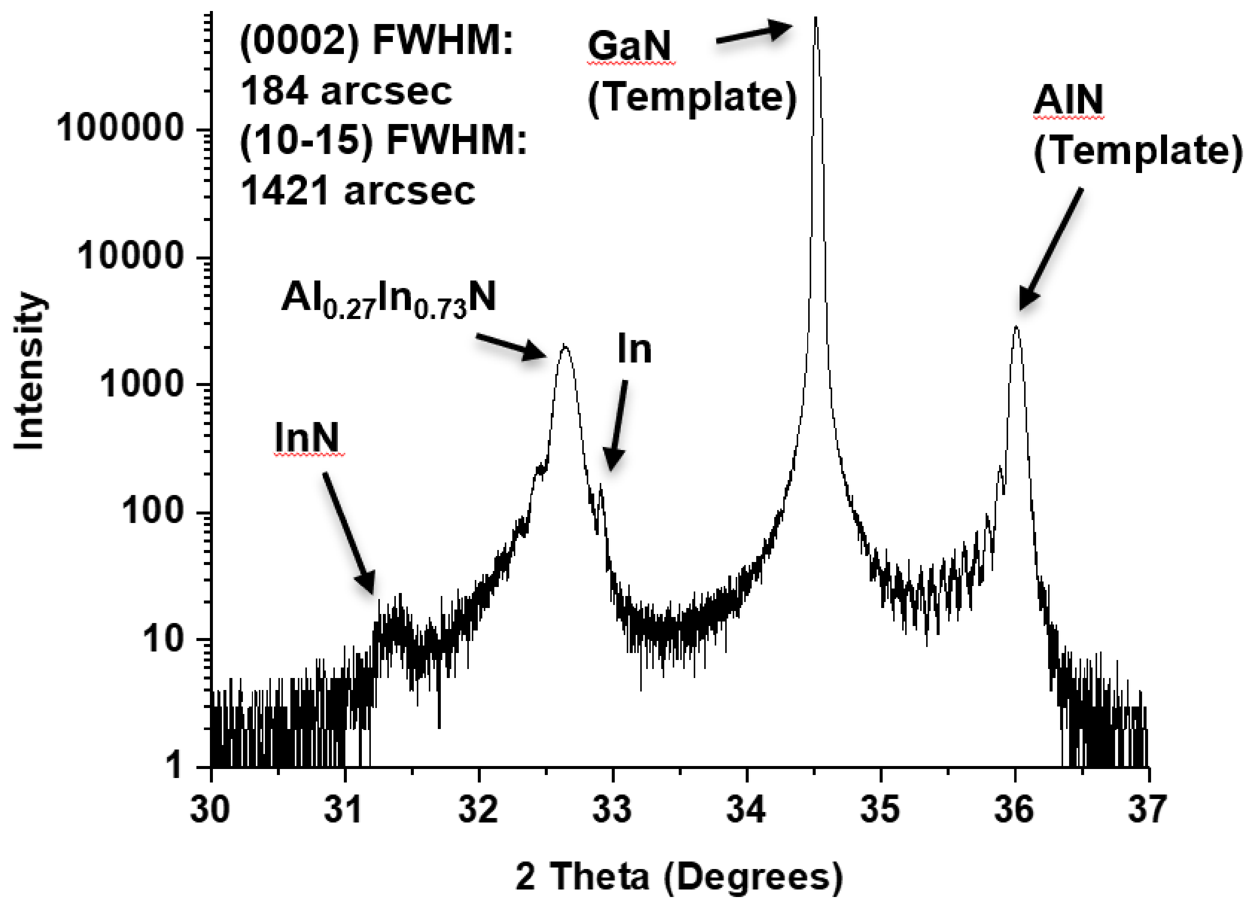

Figure 2.4: XRD 2θ-ω scan of AlInN grown with MME.

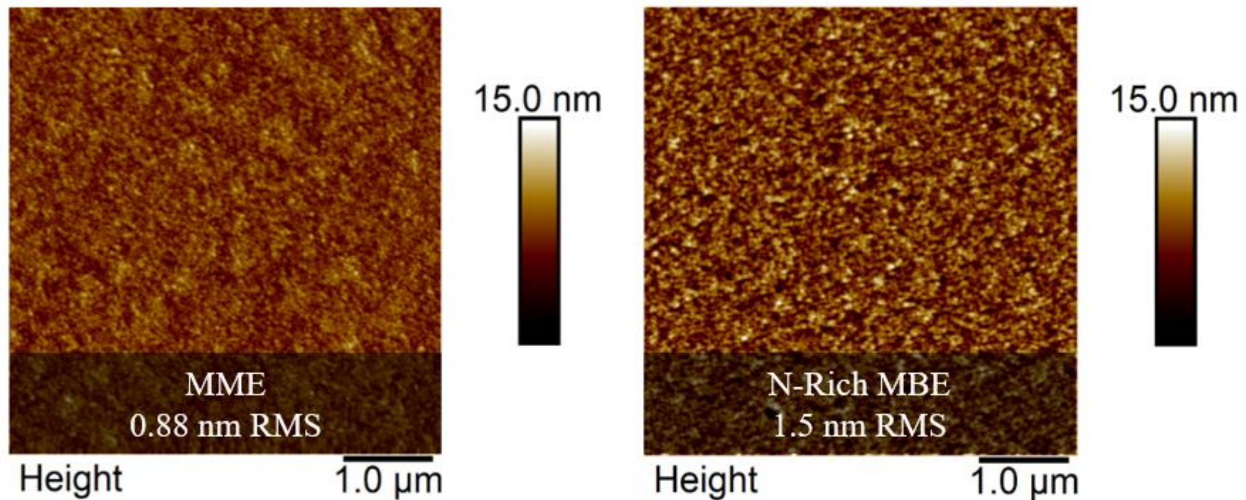

Figure 2.5: AFM scans comparing the surfaces for MME vs traditional n-rich MBE growth of AlInN showing a significant improvement when using MME.

2.3.3 Optimization of MME Growth Conditions

With initial conditions established and verifying that MME has the potential to grow excellent quality AlInN, further study was performed on the effect of substrate temperature on the films. Figure 2.6 shows the XRD 2-theta-omega scans of the AlInN samples grown at various substrate temperatures. Significant phase separation is observed in the sample grown at 425 °C displaying more than one AlInN peak along with evidence of InN at 31.4°. All samples grown at or below 400 °C show predominantly a single-composition AlInN peak at an angle of about 32.5° corresponding to 70% indium (when fully relaxed on GaN). It should be noted that the peak at 36° is an AlN buffer layer used by the substrate manufacturer, and the peak at 34.6° is the GaN peak measuring the substrate and MME buffer regrowth layer. XRD rocking curves were taken for the (0002) and $(10\bar{1}5)$ reflections, excluding the sample grown at 425 °C, and the full-width at half maximum (FWHM) values are displayed in Table 2.2. The (0002) FWHM values are low for all samples, with the lowest value being 126 arcsec at a growth temperature of 300 °C. XRD reciprocal

space maps (RSM), shown in Figure 2.7, taken around the asymmetric $(10\bar{1}5)$ reflections of the films show a primarily single AlInN peak for all films grown at or below 400 °C. The films grown below 400 °C are all fully relaxed. The rocking curve FWHM for these films is tabulated in Table 2 and detail a $(10\bar{1}5)$ rocking curve minimum value of 886 arcsec for a growth temperature of 350 °C where the (0002) FWHM value is 135 arcsec, close to the minimum for 300 °C. The $(10\bar{1}5)$ FWHM increases at temperatures below 350 °C, suggesting deteriorating crystal quality and perhaps more columnar growth at too low of growth temperatures.[157] The film grown at a too high growth temperature of 425 °C is phase separated with multiple low intensity peaks at reciprocal lattice values between GaN and InN. The combination of XRD 2-theta-omega curves and RSMs suggest that ~350 °C is the optimal growth temperature as it displays a low (0002) FWHM and shows the lowest figure of merit for the $(10\bar{1}5)$ reflection. In some cases, a surface InN layer was present in the XRD scans which is common in MBE where a thin portion of the top ternary layer thermally decomposes and reforms into a thin InN surface layer upon cooldown because it is exposed to the nitrogen plasma.[58] Only the 425 °C sample grown above the InN decomposition temperature shows clear evidence of In metal remaining and clearly showed In droplets by the naked eye, presumably due to constant buildup of In throughout the entirety of the growth. While thin indium can be converted to InN on cooldown under the plasma and appear as such in the XRD, thick layers or droplets cannot be converted to InN and result in in signatures in the XRD.

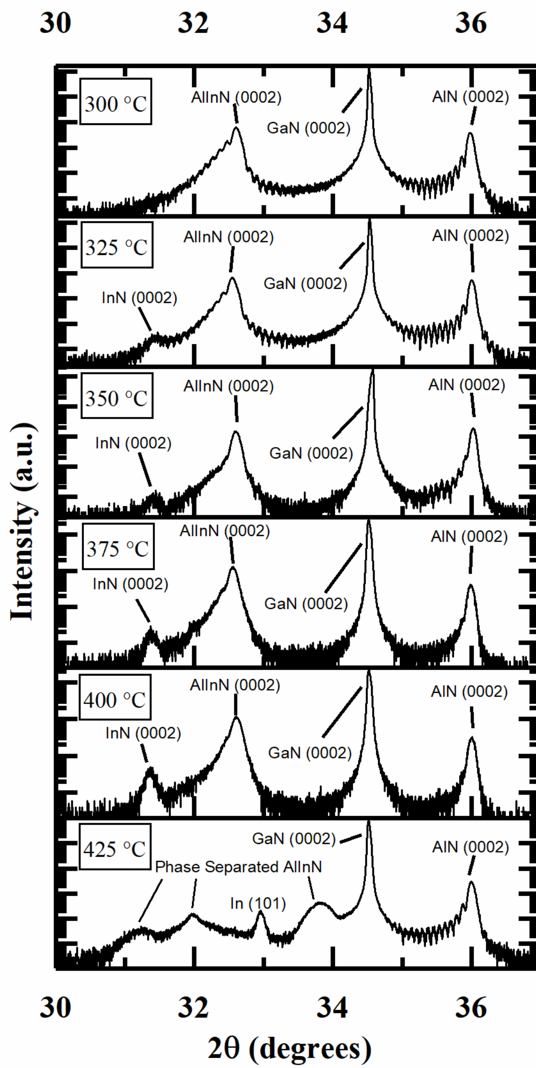

Figure 2.6: XRD scans of AlInN grown over a range of substrate temperatures.

Table 2.2: XRD figures of merit for AlInN films grown with MME over a range of substrate temperatures.

Growth Temp ($^{\circ}$C)	(0002) FWHM (arcsec)	$(10\bar{1}5)$ FWHM (arcsec)
400	304	1350
375	478	1320
350	135	886
325	148	1030
300	126	1320

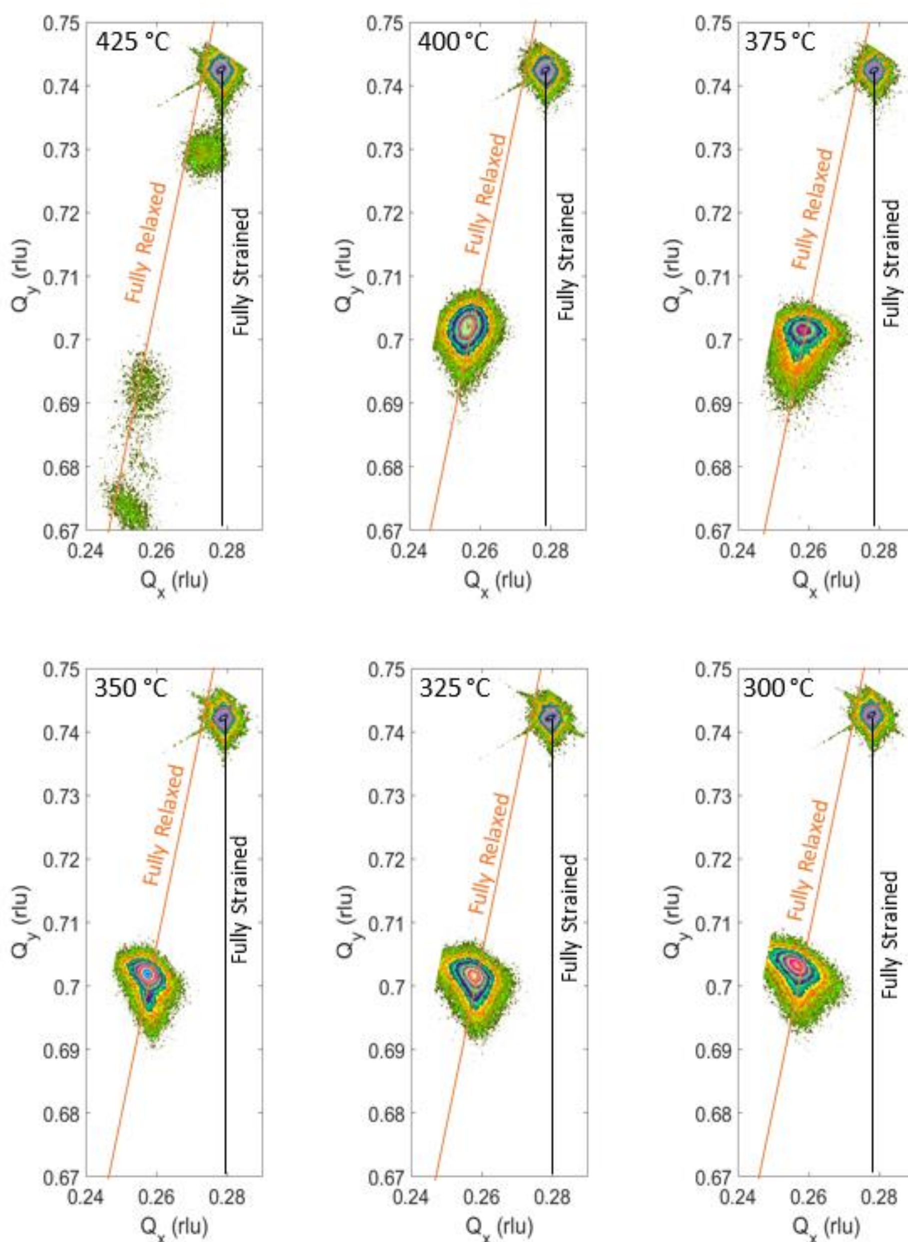

Figure 2.7: XRD reciprocal space maps of the AlInN films grown at different substrate temperatures.

The increase in crystal quality with a reduced growth temperature is likely due to the control of surface atom kinetics, enabling enhanced surface diffusion via the metal rich surfaces achieved during MME growth. Since phase separation and crystal quality both result from long

diffusion lengths, there are two methods of tuning the optimal surface diffusion length so as to optimize crystal quality without incurring phase separation. These two methods are control of the substrate temperature and metal adlayer coverage. If temperature is to be optimized, the exponential relationship of diffusion coefficients versus temperature leads to difficulty in the control, optimization, and repeatability of the surface condition that balances crystal quality with low phase separation. Conversely, if strong semiconductor bonds are replaced with weaker metallic surface bonds, atomic diffusion increases.[59] For metallic enhancement of surface diffusion, the surface diffusivity is a linear combination of the diffusivity of In and Al on the growing film. Thus, the use of metal modulated epitaxy adds an additional element of control with this linear combination, tempering the exponential nature of the temperature variations and kinetically enhancing diffusion lengths even at these low growth temperatures which kinetically inhibits diffusion. This results in a more controlled growth window and the possibility of improved crystal quality and repeatability.

Given the diverse optimal substrate temperatures for AlN (> ~750 °C) and InN (< ~425 °C), the high metal coverage of MME aids in lowering the optimal temperature range for aluminum bearing materials. Indeed, it has been shown that even small additions of In surfactants improve surface mobility for Al bearing films.[158] For the films with high indium (~70%) compositions, these results demonstrate substantial suppression of the optimal growth temperature window compared to the AlN binary. This suppression is necessary for AlInN since it must be grown below the decomposition temperature for InN otherwise surface accumulation of In will occur.[14,159]

Furthermore, precise control with the MME shuttering scheme randomizes the nucleation points for epitaxy which can be useful for preventing Oswald ripening of phase separated regions. AlInN MME provides a “dry” nitrogen terminated surface every ~1.2 nm under these conditions

(1.6 um/hr growth rate and 2.8 seconds of growth time, 1.4 seconds of nitrogen terminated time per cycle). With a III/V ratio of 1.3, the nanoscopic metal islands that form each cycle form, ripen in size and then are consumed during the metal-off portion of the cycle. Thus, every ~1.2 nm of film thickness, the nucleation points for lateral phase separation are randomized by the random spontaneous nucleation of new metal rich nanoscopic islands.

Figure 2.8 shows 5x5 μm AFM scans of the five films grown below 425 °C, as well as corresponding RMS roughness values. All samples show smooth surfaces, varying in RMS roughness from 1 nm to 0.44 nm. A significant reduction in roughness is observed with reduced growth temperature. At the higher growth temperatures of 375 and 400 °C the samples display roughness values around 0.9 to 1.0 nm RMS, however with reduced growth temperatures we observe low roughness values of about 0.44 nm RMS. The lower temperature growths also display spots similar in appearance to the spiral hillocks often seen in very smooth MBE-grown GaN,[154] which could indicate a two-dimensional growth mode leading to these smooth surfaces.

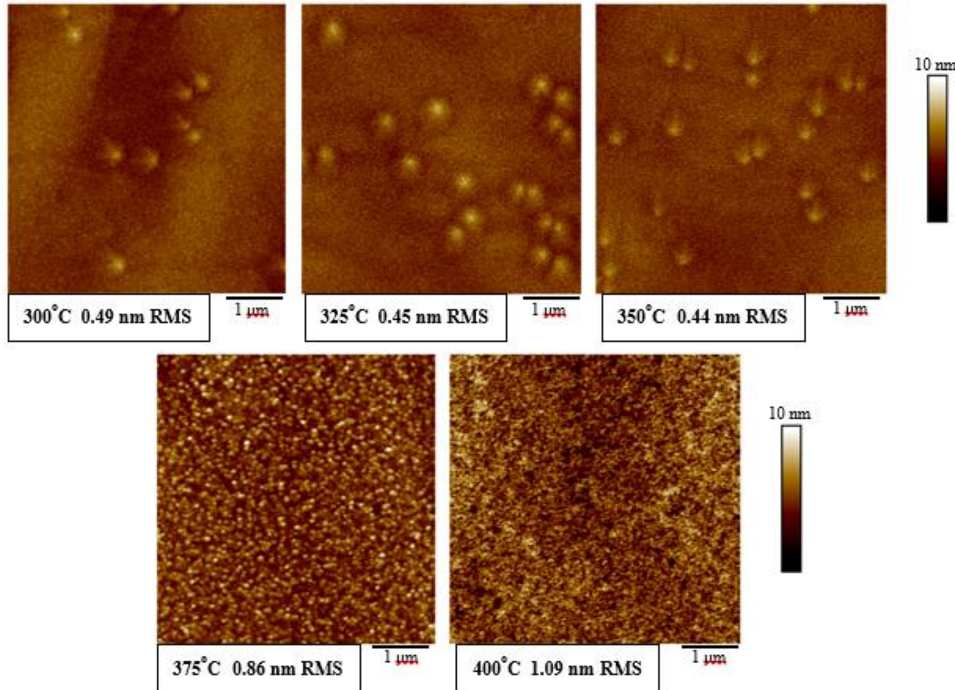

Figure 2.8: AFM scans of the AlInN films grown at varying substrate temperatures showing smooth surfaces for low growth temperatures.

2.3.4 Quantum Well Like Emissions Observed From Bulk Films

In addition to structural and morphological measurements via XRD and AFM, the optical response of the films is measured via PL to examine the material quality and viability for future optoelectronics. Figure 2.9 displays RT PL spectra of the AlInN samples. The PL measurements for samples grown below 425 °C show the same primary peak centered near 1.45 eV. All PL scans exhibit a similarly shaped spectra, except the film grown at 425 °C. For the film grown at 425 °C, significant phase separation occurs, as previously observed in XRD, and a shift of 0.13eV occurs in the primary peak to a lower energy as well as a loss of intensity. Interestingly, the measured spectra for films grown below 425 °C can be fitted with a four peak model, allowing four emission energies to be extracted, as shown in Figure 2.10 for the sample grown at 350 ºC. Since several quantum well, dot, or wire structures have similar energy relationships, these emission energies

are plotted relative to the peak number squared and exhibit a linear fit as displayed in Figure 2.11. This fit suggests that the emission levels within these curves could be the result of quantum well emissions where energies vary with the quantum confined structure index squared as represented for example by the equation,

$$E = \left(\frac{\pi^2\, \hbar^2}{2m}\right)\left(\frac{n_x^2}{L_x^2} + \frac{n_y^2}{L_y^2}\right) \quad n_x, n_y = 1, 2, \ldots \qquad (1)$$

for a quantum wire where n is the quantum well index, ħ is the reduced Planck's constant, m is the effective mass, and L_x and L_y are the well lengths. The slope of the data in Figure 6 is used to calculate the widths of the quantum confined structure and the y intercept corresponds to the band gap. The actual dimensionality of the modeled quantum confined structure, whether dot, wire or well, will modify the extracted dimensions but the y intercepts all yield a value that is nominally the same for the band gap.

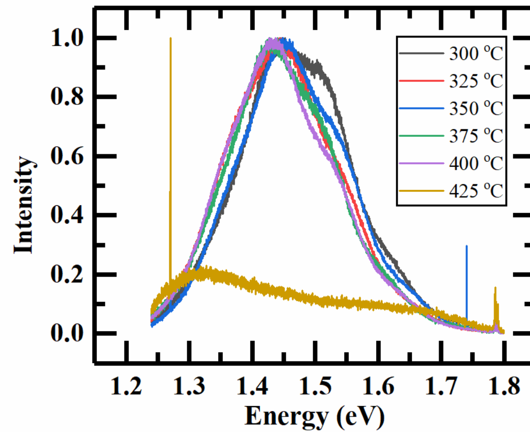

Figure 2.9: PL measurements taken for the AlInN films grown at varied substrate temperatures.

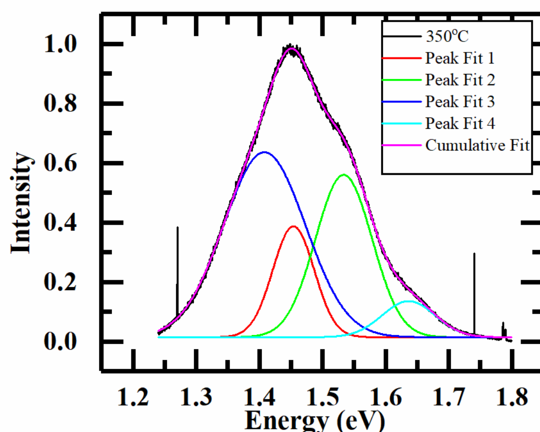

Figure 2.10: 4 peak fitting of the PL emission for the sample grown at 350 °C.

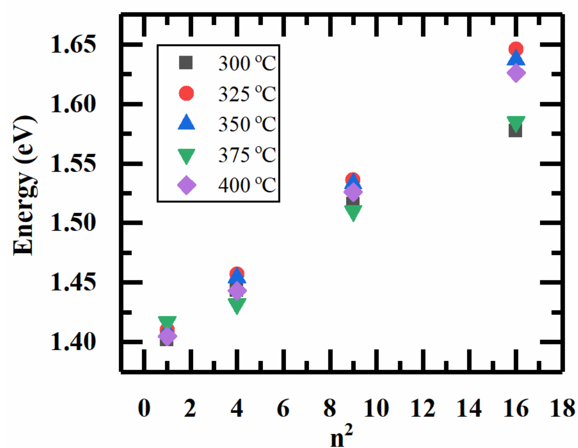

Figure 2.11: Peak energy vs index squared for fitted peaks modelling the PL emissions.

All forms of quantum confined structures, whether wells, wires or dots vary in confined energies by factors involving n^2 where n is the index of the energy state. While we do not have direct evidence to support whether the emission is due to a well, wire or dot, we point out that the PL peak energy positions track very well with n^2 and the base energy bandgap extracted from the regression analysis matches the targeted indium composition. Thus, there is confidence the emission results from some quantum confined state in a lower dimensional structure formed

through nano-phase separation. Future structural analysis is needed to confirm the presence of specific quantum confined structures. Further support for this quantum-wire like emission in AlInN is the in-plane compositional fluctuations that are commonly observed in the literature and described as a honeycomb structure. The honeycomb structure consists of Al-rich columns surrounded by In-rich borders.[74,75] It is possible that these columns could form vertical quantum wires/sheets with discrete energy levels in the high indium and low bandgap border regions which may explain the quantum wire-like features of the PL spectra. Modeling the emission as a quantum wire with a square shape results in well widths between 15 and 18 nm using equation 1 and assuming L_x is equal to L_y.[160] Table 2.3 shows the calculated well widths, and the energy bandgap which is constant at 1.395 ± 0.005 eV for all the spectra. The positions of the primary PL peaks, as well as the calculated base bandgap emission energies, align with the expected value given for a bowing parameter for AlInN of 4 ± 0.2 eV for 70% In.[114] Interestingly, the approximate minimums and trend in the well widths derived from the PL correspond with the minimum and trends in the XRD figures of merit suggesting the crystal quality and possibly strain plays a factor in the size of the phase separated region. Given the low temperature well widths are similar to higher temperature widths, it is unlikely thermal variation in the diffusion coefficients are responsible for the differing well widths. These photoluminescence properties suggest that AlInN is promising as an optical material for III-nitrides in this challenging bandgap range.

Table 2.3: Primary emission level and well width for quantum confined like emissions in AlInN films.

Growth Temp (°C)	Band Gap (eV)	Well Width (nm)
300	1.40±0.01	17.9±0.5
325	1.39±0.01	15.5±0.5
350	1.39±0.01	15.7±0.5
375	1.40±0.01	17.9±0.5
400	1.39±0.01	15.9±0.5

2.4 Conclusion

In summary, we have demonstrated a method for growing high quality, indium rich AlInN where thermally driven diffusion is suppressed at low temperatures and compensated by increased adatom diffusion via metal rich surfaces. XRD rocking curve measurements display excellent crystallinity in both the symmetric and asymmetric reflections and suggest defect reduction with reduced growth temperatures down to 350 °C with greatly reduced phase separation which leads to optical emission with repeatable peak energy position over a wide range of deposition temperatures. The optical emission spectra suggest emission from a quantum confined structure,

which when modelled as a quantum wire yields an inferred wire sizes between 15-18 nm for a wide range of growth temperatures, promising for optoelectronic and photovoltaic device applications.

CHAPTER 3. APPLICATION OF MME TOWARDS HIGH INDIUM CONTENT ALINN OVER A WIDE COMPOSITION RANGE

3.1 Introduction

The past couple decades have seen rapid advancement in III-Nitride materials and devices based on the same. AlN, InN, GaN, and their alloys have taken the forefront in many fields, including light emitting diodes (LEDs), high electron mobility transistors (HEMTs), and power electronics.[1-19] These advancements have largely been made thanks to swift progress in epitaxy of GaN and its ternary alloys with InN and AlN. InGaN has become a dominant material in the field of blue and green LEDs and laser diodes, and AlGaN has achieved the same with UV LEDs in addition to transistors and high power devices.[8,9,107,164–166,172–175] However, despite having equal or superior properties in many aspects, AlInN has seen significantly less study. In addition to having a tunable bandgap ranging from 0.65 eV (InN) to 6.1 eV (AlN), AlInN has the unique property among the traditional III-Nitride ternaries of being lattice matched to GaN at a composition of ~18% indium.[77,78,114,143,176] This, in combination with the high spontaneous polarization values of the alloy, have given AlInN a distinct advantage in high performance HEMT devices, achieving some of the best performance metrics in literature.[66,114,127,162,163] Additionally, this lattice matching has allowed for advancements in structures like strain free buffers for defect reduction and

distributed Bragg reflectors.[67,173] However, outside of the specific lattice matched composition there has been minimal study relative despite the theoretical potential of the alloy system.

Two of the greatest challenges remaining for the III-Nitride field are long-wavelength emission and photovoltaics. While InGaN can achieve high efficiency blue emission and has made strong advances in green emission, strain related defect generation has limited red emission from this material.[111–113] For much the same reason, photovoltaic development has been limited in InGaN. With a composition of ~42% Al AlInN can achieve a bandgap of 2 eV for red emission and quantum dot like emission has been reported for AlInN thin films, making it a promising material for long wavelength emission. Additionally, AlInN can achieve nearly all useful bandgaps for photovoltaic applications which, paired with an exceptionally high absorption coefficient, gives it promise for high efficiency solar cells and photodetectors.[176,177] However, to take advantage of these properties high indium contents must be used in the films, which comes with significant growth challenges.

Due to the large differences between the binaries InN and AlN, a number of challenges exist for growth of the ternary alloy. For one, the optimal growth temperatures for InN and AlN are vastly different.[159] Elevated substrate temperatures can cause the disassociation of In-N bonds so a compromise must be used, resulting in substrate temperatures lower than ideal for an Al bearing alloy and low surface mobility for Al atoms.[64] Second, a large lattice mismatch exists for the binary alloys, with the a lattice constants for InN and AlN being 5.445 and 5.118 Å respectively. As a result of this mismatch, a large miscibility gap exists for the ternary, exasperating issues of phase separation during growth. The issue of phase separation is made even more difficult by a third issue: the difference in the atomic radius of In and Al. These issues, along

with the lack of a suitable native substrate for the alloy with high indium contents, results in growth difficulties that must be overcome.

Recently, great success has been demonstrated in the growth of high In content AlInN via the modified molecular beam epitaxy (MBE) technique metal modulated epitaxy (MME).[143] Via engineering of surface kinetics to improve adatom mobility, low temperature growth was utilized in order to grow $Al_{0.3}In_{0.7}N$, demonstrating significant improvements in the structural and surface quality of the alloy as displayed in Chapter 2. Such a method is well suited for the low temperature required to prevent In-N bond decomposition and could be expanded to traditionally difficult to grow high indium compositions. In this paper we demonstrate the growth of AlInN in a composition range between 50 and 90% In grown with high crystal quality, low surface roughness, and strong absorption via MME.

3.2 Experimental

All films in this study were grown in a Riber 32 MBE reactor using the MME technique, the details of which can be found elsewhere.[23,142,143,153] All samples were grown on 1x1 cm semi-insulating hydride vapor phase epitaxy (HVPE) grown GaN-on-sapphire templates. The substrates were single-side polished and 2 μm of tantalum was sputtered on the backside to facilitate uniform heat conduction during growth. Prior to growth the substrates were cleaned using a 3:1 solution of H_2SO_4:H_2O_2. This clean was followed by a rigorous rinse with DI water and a brief dip in dilute HF to reduce surface oxides, after which the sample was again rinsed with DI water and dried with N_2. After the chemical cleaning procedure, the samples were loaded into an introductory vacuum chamber in which they were outgassed at 200 °C for 20 minutes. Prior to growth, the samples were further outgassed at 650 °C for 10 minutes in the growth chamber.

During growth, all metal fluxes were provided by conventional effusion cells. Nitrogen was provided by a Veeco UNI-Bulb radio frequency (RF) plasma source with an RF power of 350 W and a gas flow of 2.5 sccm. A 100nm GaN layer was grown prior to the AlInN layer using MME for all samples and is described elsewhere.[38,154] The AlInN films were grown using MME with a metal rich III/V ratio of 1.3. The shuttering scheme is detailed in our previous work and was selected to limit metal buildup.[143] The substrate temperature for the AlInN film growth was selected to be 350°C based on previous optimization. These temperatures are below the In desorption temperature in our system and will achieve full indium incorporation into the film. All of the MME-grown AlInN layers had a thickness of 100 nm and metal fluxes were varied to change the AlInN composition between 10 and 50% Al.

In situ surface monitoring was performed using reflection high energy electron diffraction (RHEED) and post-growth x-ray diffraction (XRD) analysis was performed with a Philips X'pert Pro MRD using a Cu Kα1 anode. Atomic force microscopy (AFM) images were taken with a Bruker Icon AFM in tapping mode. Spectroscopic ellipsometry (SE) was performed using a Woollam M2000 ellipsometer operating at 370-1700 nm. SE modelling was performed using the Woollam Complete EASE software.

3.3 Results and Discussion

3.3.1 Structural Properties of High In Content AlInN

MME has previously demonstrated great benefit in the growth of $Al_{0.3}In_{0.7}N$, improving XRD figures of merit by 11x over previous literature values. While this composition is useful for potential applications in tandem on silicon solar cells, the applications of high indium content AlInN can be expanded if other compositions can be grown with similar quality. Thus, MME was

applied to grow a series of AlInN films grown in a composition range of 10 to 50% Al. Figure 3.1 shows the XRD 2θ-ω curves of AlInN films grown over a composition range of 10 to 50% Al. All compositions show a distinct AlInN peak as labeled in Figure 3.1, along with GaN and AlN peaks from the HVPE template. Table 1 shows the XRD (0002) and (10-15) ω rocking curve full width at half maximum (FWHM) values for the films. All films show excellent figures of merit, ranging from 135 to 180 arcsec for the (0002) peak and 759 to 1250 arcsec for the (10-15) plane. It should be noted that the (0002) RC values are such that the crystal quality in this case is substrate limited and growth on low defect density GaN substrates would likely see even further improvement in crystal quality. Composition was determined via XRD reciprocal space map analysis. The AlInN peaks show a fading lower angle shoulder, especially at the 42 and 50% compositions, suggesting these films may have a higher compositional variation than the remaining films.. Additionally, some samples display an In metal and/or an InN peak due to surface decomposition of the film and subsequent re-nitridation post-growth that was shown previously for InGaN to be eliminated if the film was capped with GaN.[178]

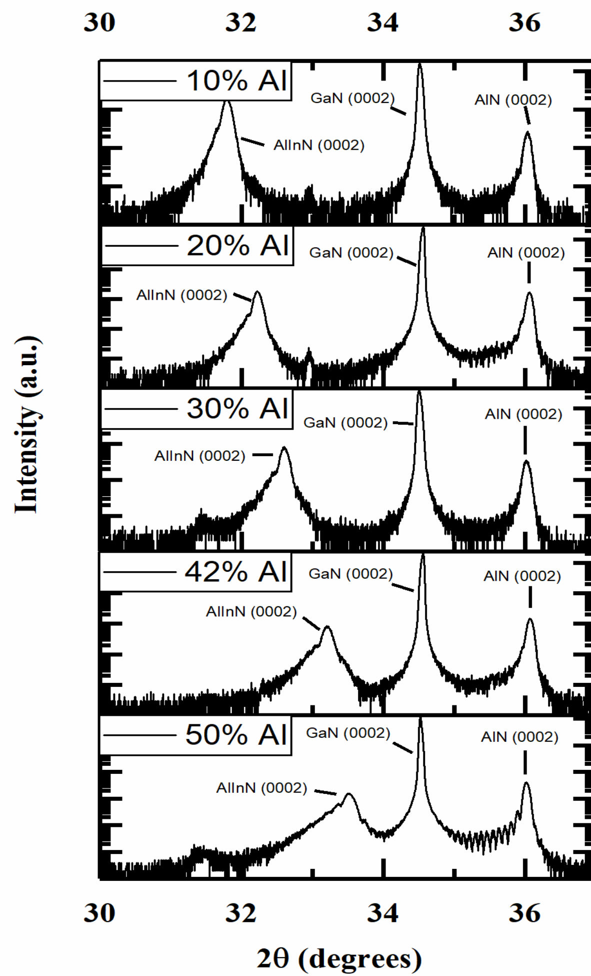

Figure 3.1: XRD 2θ-ω scans of AlInN films grown via MME at different compositions.

Table 3.1: XRD figures of merit for low temperature, MME grown AlInN.

Composition	(0002) RC FWHM (arcsec)	(10-15) RC FWHM (arcsec)
10% Al	180	855
20% Al	148	759
30% Al	180	761
42% Al	135	798
50% Al	148	1250

This material quality was enabled by low temperature, metal rich growth of the AlInN films. Traditionally, low Al content AlInN films are grown by MBE in the substrate temperature range of 500-600 ^{o}C, however this is above the expected temperature for In-N bond decomposition and In desorption.[159] As a result, growth in this higher temperature range will result in film degradation and potential phase separation. By growing at low temperatures, 350 ^{o}C in this case, the issue of In related degradation can be mitigated or eliminated increasing crystal quality. However, by traditional understanding such a low growth temperature would also render surface Al atoms nearly immobile, an issue that can be overcome via metal rich growth.[64,142,143] By

accumulating an adlayer of metal on the growth surface, the energy of the diffusion barrier height for adatom hopping can be greatly reduced, resulting in an exponential increase in the adatom diffusion rate even in a low thermal energy environment. Thus, combining low temperature growth and a metal rich surface the issues traditionally limiting quality in this material system can be overcome.

Figure 3.2 shows the AFM scans of the five AlInN samples grown over a wide composition range. All compositions show excellent surface roughness, with the highest being 1.13 nm RMS, and the inclusion of spiral hillock like features, commonly seen as a result the growth progressing in a Frank-van der Merwe growth mode. Interestingly, despite the low growth temperature, increasing the Al content does not initially cause an increase in the surface roughness. At the lowest Al content the surface shows one of the highest RMS roughnesses of 1.08 nm. Adding further Al leads to an initial decrease in surface roughness, down to 0.60 nm at 20% Al and then further to 0.44 nm at 30% Al, which matches well with the roughness observed in our previous work on $Al_{0.3}In_{0.7}N$.[143] However, increasing the Al content further and moving into the center of the composition range and the miscibility gap leads to an increase in surface roughness. This trend is to be expected as the growth conditions here were derived from the optimized conditions for the prior $Al_{0.3}In_{0.7}N$ study and also phase separation will be the most difficult to control near the center of the composition range, resulting in degradation of the material. The trend in roughness also aligns well with the FWHM of the XRD (10-15) rocking curves. Initially increasing the Al content results in both a reduction in the FWHM and the surface roughness, while increasing the Al content past 30% Al leads to both an increase in the FWHM and surface roughness.

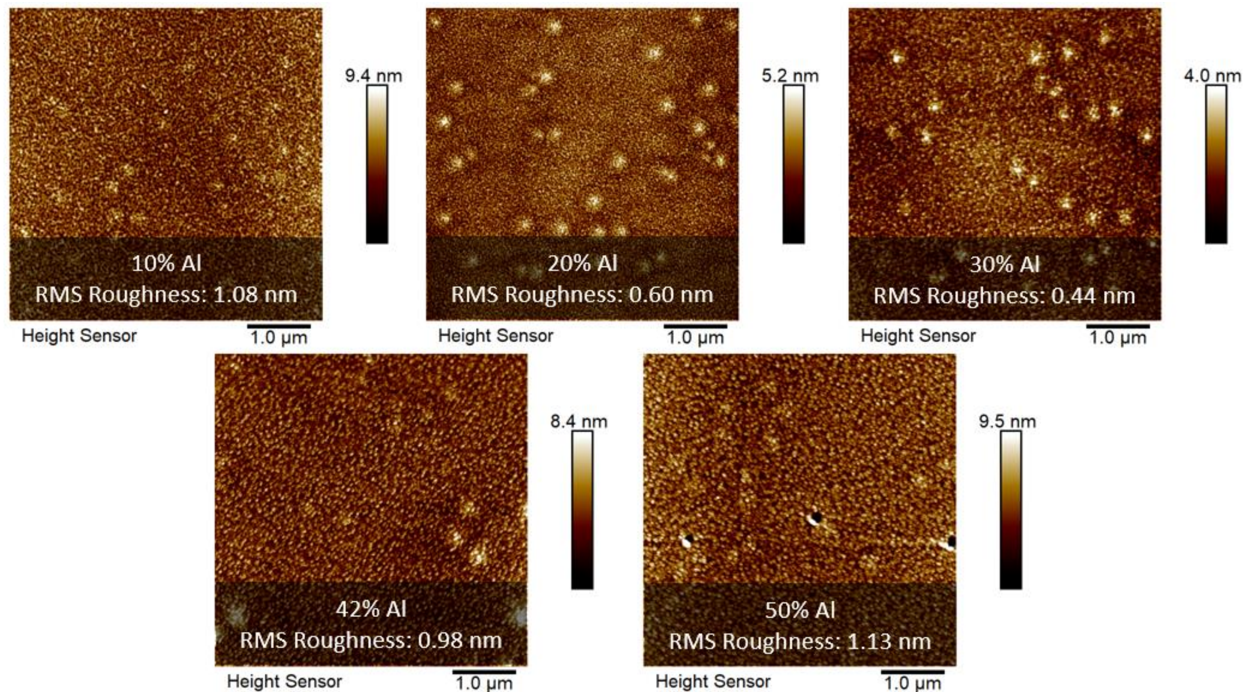

Figure 3.2: AFM scans of AlInN films grown over a wide composition range.

3.3.2 Strong Stokes Shift in the Photoluminescence of AlInN

For thick films of a semiconductor, the emission spectra from a technique like photoluminescence (PL) can be used to assess both the optical performance of the material and the bandgap, especially for a direct bandgap semiconductor like AlInN. In order to do so, PL emission was measured from the 5 different composition AlInN films and is shown in Figure 3.3. Several key observations can be seen from the PL spectra. First is the odd shift in emission energy with the composition variation. The emission energy should shift from about 1.2 to 2.1 eV, assuming a bowing parameter of 4 eV. While the emission energy from the 10 and 20% Al samples align reasonably well with the theoretical values, the 30, 42 and 50% Al samples do not, showing emission energies between 1.4 and 1.5 eV, well below theory, and significant reduction in emission

intensity. Obvious oscillations are also present in the 42 and 50% Al samples, but these are the result of Fabry-Perot interference with the underlying GaN substrate. These oscillations can only be seen in certain samples with low intensity emission but presumably would be present in all samples.

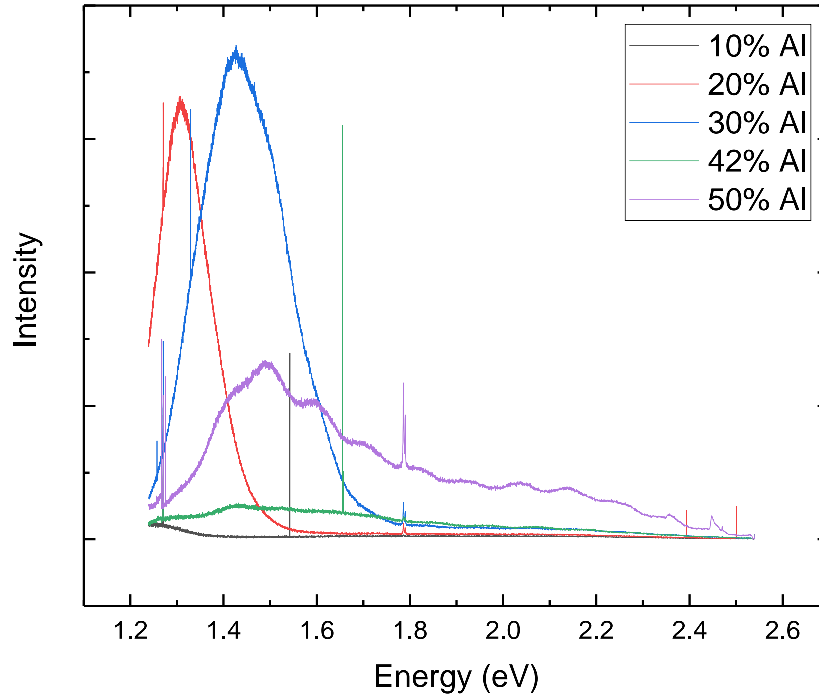

Figure 3.3: PL Emission spectra for AlInN films grown over a wide composition range showing significant variation in both peak energy and intensity with composition.

There are several factors that can explain a shift in emission energy from theory. The Quantum-confined Stark effect is a commonly found phenomenon in nitride based optical devices, but typically applies to low dimensions structures such as quantum wells and is unlikely to apply to a 100 nm thick film. A Moss-Burnstein shift can be observed in heavily doped films, which may be the case for these high In content relaxed films, but typically results in a blue shift as carriers

fill energy states and cause and effectively cause a widening of the energy for a band to band transition and would not explain the downward shift in emission energy present in the 42 and 50% Al samples. There are two causes for such a significant shift in emission from theory that may explain the results here. The first is emission from a defect state within the film. The most likely source of an emission dominating "defect" state here is nanoscale phase separation. In this case growing close to the center of the composition range could drive phase separation and the formation of nanoscale inclusions of high In content AlInN. This nanoscale phase separation has long been believed to be the reason for the high efficiency of InGaN based LEDs, despite the high defect density of the material. The formation of these nanoscale In rich inclusions would in effect act as quantum confined structures, trapping carriers for high efficiency radiative recombination and driving carriers away from non-radiative recombination centers (NRC) like threading dislocations.[53,90] This results in high efficiency emission at an energy lower than what would be expected from the bulk film composition. However, in the case of InGaN this results in emission that is still close to the band edge. In the case of AlInN this phase separation appears to create states that are far deeper in the band than the shallow states observed for InGaN. Given the fact that the peak emission energy for both the 42 and 50% Al samples are near that of the 30% Al sample and the fact that the growth condition optimization performed leading into this study were based around a composition of 30% Al, it is not unlikely that the given growth conditions lead to favorable formation of regions of ~$Al_{0.3}In_{0.7}N$ within the film. With growth condition optimization for each given composition it is possible that this issue could be mitigated or eliminated entirely and each composition would yield emission peaks closer to the bandgap instead of being seemingly limited to about 1.4 to 1.5 eV.

The second mechanism to explain the shift in emission energy would be a pinning of the emission level. A surface pinning of the fermi level has been observed for InGaN in the past and may also be present in these films. In this case the high surface defect concentration of the film results in the pinning of the fermi level to a constant energy state, even with shifting compositions. This may explain not only the shift in emission energy, but also the fact that all the samples between 30 and 50% Al show emission energies between 1.4 and 1.5 eV. Both the nanoscale phase separation and emission energy pinning explain the shift in emission energy from theory and may both be present. It should also be noted that such a shift is not unprecedented, with Stokes shifts up to 1 eV being observed in previous AlInN studies.[179] Regardless, these results show that another method must be used to assess the bandgap and optical properties of the films.

3.3.3 Spectroscopic Ellipsometry – An Alternate Method of Determining Optical Properties

For SE analysis, a model was built for both the substrate and the AlInN layers. First, a layer structure was built for the substrate including the sapphire substrate, the AlN initiation layer, the GaN layer, and a surface layer. For the sapphire, AlN, and GaN layers pre-existing oscillator models within the Woollam Complete EASE software were utilized and a good fit to the substrate thickness and optical constants was obtained. For the AlInN layers a custom double oscillator model was built and fit for each different composition. The double oscillator model consisted of two Tauc-Lorentz oscillators using equation 1. Here, A gives the amplitude, E_0 is the center energy, and B represents the damping. The Complete EASE^{TM} software fit these three parameters to best match the ellipsometry raw data and an example fit is shown in the top part of Figure 3.4. Fitting the oscillator functions in the Tauc-Lorentz oscillator model to the ellipsometry data provides the imaginary part of the dielectric function (ε_2) and the real part (ε_1) is determined by the software using the Kramers-Kronig relationship, yielding the full complex dielectric function over the entire

measured wavelength range. Since we are concerned with the absorption of the film to derive bandgap, we focus on ε_2 herein. From this, the optical constants were extracted and were found to agree well with previous literature values for similar compositions.[177] From this, the absorption coefficients were calculated and the Tauc plots for AlInN are shown in the bottom part of Figure 3.4. Table 2 shows the extracted bandgap vs the Al content of the AlInN films. The bandgap of the films align well with previous reports of AlInN in this composition range and show excellent absorption coefficients, suggesting strong promise for optical and photovoltaic applications.[114,180]

Equation 1: Tauc-Lorentz oscillator equation.

$$\varepsilon_2(E) = \frac{A}{E_0^2 - E^2 - iBE}$$

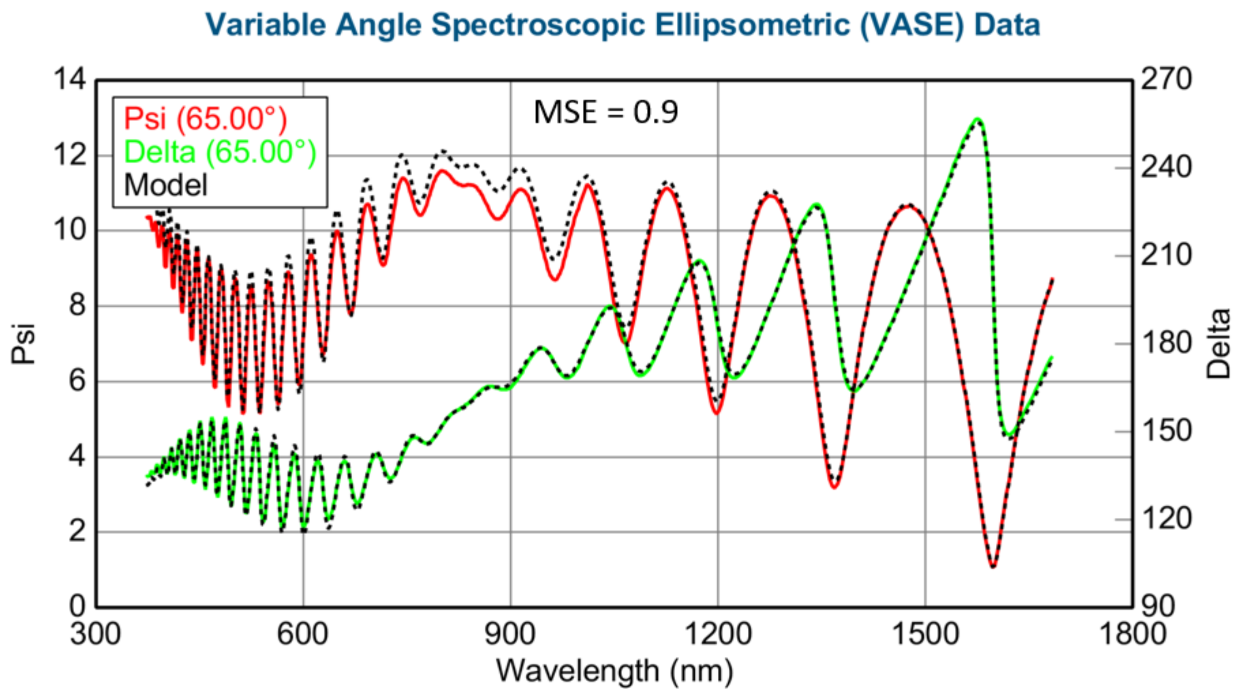

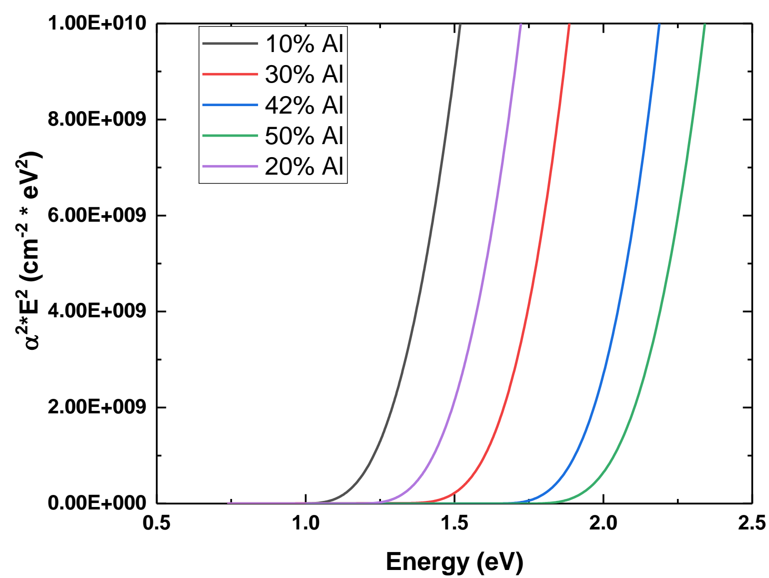

Figure 3.4: (Top) Fit of the Tauc-Lorentz oscillator model to the raw SE data for the $Al_{0.3}In_{0.7}N$ sample. (Bottom) Tauc plots for AlInN films with compositions between 10 and 50% Al.

Table 3.2: Extracted bandgaps at each composition from Tauc plot extrapolation.

Composition	Extracted Bandgap (eV)
10% Al	1.21
20% Al	1.46
30% Al	1.66
42% Al	2
50% Al	2.18

3.4 Conclusion

Metal modulated epitaxy was applied to grow high quality AlInN over a wide, indium rich, composition range. Low temperature, metal rich growth was applied to overcome traditional kinetic limitations and demonstrate films with high crystal quality and low surface roughness. X-ray diffraction figures of merit show substrate limited crystal quality and atomic force microscopy show surface roughness at or below 1 nm. Spectroscopic ellipsometry measurements show high absorption coefficients and film absorption edges that align well with theoretical material bandgaps and previously observed experimental values. While phase separation and quantum

confinement dominated luminescence were not eliminated, these results demonstrate strong promise of this growth method for the growth of high quality, In-rich AlInN for long wavelength absorption and emission applications.

CHAPTER 4. HYPER DOPING OF ALGAN FOR IMPROVEMENT OF DEEP UV OPTOELECTRONICS

4.1 Introduction

AlGaN has been a major factor in the ability of the III-Nitride material system to enter the forefront of the optoelectronics, power electronics, and RF transistor fields.[171-180] The bandgap of AlGaN ranges from 3.4 to 6.1 eV, allowing emission to range from UVA to UVC.[8-11] As a result, material and device advancements have allowed AlGaN to rank among the most promising materials for UV solid state emission.[9,11,166] Due to the fact that breakdown voltage for a direct bandgap semiconductor scales with $\sim E_g^{2.5}$ the wide bandgap nature of AlGaN also has allowed for the fabrication of high reverse breakdown voltage power diodes.[106] High performance RF transistors have been enabled due to the high polarization sheet charge generated at an AlGaN/GaN interface. These heterostructures have allowed for the development of HEMT stacks with 2DEG densities above 10^{13} cm^{-2} and have pushed forward next generation RF switching devices.[126,127]

A challenge still remaining in the development of all the AlGaN based devices listed above is efficient doping of the materials.[102,181,182] This is especially true in the case of optoelectronics. A severe limiting factor in the development of high efficiency UV LEDs has been carrier injection into the active region of the device. Due to both the poor doping efficiency of AlGaN and the low hole mobility, asymmetric carrier injection has caused efficiency reduction in AlGaN based LEDs, especially at high injection currents in a phenomena known as efficiency droop.[98,171,183] At high injection currents poor hole injection can result in spillover of electrons from the active region, leading to recombination outside of the desired areas within an LED. Further issues are caused by

this asymmetry when attempting to use multi-quantum well structures. Poor hole injection results in emission from a MQW structure being limited to only one or two wells closest to the p doped region, as electrons will be captured and recombine with holes before they can move to wells further from the anode region.[70,183,184] While only limited increase in hole mobility can be achieved, this issue can be mitigated or eliminated if the hole concentration is significantly increased. However, significant challenges exist to be overcome for p-type doping of AlGaN.

One challenge limiting doping of AlGaN is the increase in dopant activation energy as the aluminum content increases. For Si doping, the activation energy increases from 24 meV to 211 meV when increasing the Al content from 85 to 96% and a similar trend is expected for Mg.[106] In traditional MBE growth, the activation energy for p-type doping Mg is ~170 meV for GaN and increases to as high as 630 meV for AlN.[38] As doping efficiency scales exponentially with activation energy, this almost 4x increase in activation energy will severely limit the hole concentration within AlGaN films. MME has shown great potential in improving the doping efficiency of III-Nitrides. Gunning *et al.* demonstrated a reduction in activation energy from the traditionally accepted value of 170 meV to 43 meV.[38] This was determined to be the result of the formation of an impurity band for acceptor as opposed to a single acceptor level. This resulted in an high activation efficiency and hole concentrations as high as 6×10^{19} cm^{-3}. The same was recently applied to Be doping of AlN, reducing the activation energy from ~330 meV to 37 meV.[106] This same technique could be applied to Si and Mg doping of AlGaN to greatly increase the doping of the materials and lead to improved device performance.

4.2 Experimental Details

All films in this study were grown in a Riber 32 MBE reactor using the MME technique, the details of which can be found elsewhere.[142,143,153] All samples were grown on 1×1 cm^2 metal organic chemical vapor deposition (MOCVD) grown AlN on sapphire templates. The substrates were single-side polished and 2 μm of tantalum was sputtered on the backside to facilitate uniform heat absorption during growth. Prior to growth the substrates were cleaned using a 3:1 solution of H_2SO_4:H_2O_2. This clean was followed by a rinse with de-ionized (DI) water and a brief dip in dilute HF to reduce surface oxides, after which the sample was again rinsed with DI water and dried with N_2. After the chemical cleaning procedure, the samples were loaded into an introductory vacuum chamber with a base pressure of $\sim 1 \times 10^{-9}$ Torr in which they were outgassed at 200 °C for 20 minutes. Prior to growth, the samples were further outgassed at 800 °C, as measured via thermocouple, in the growth chamber.

During growth, aluminum, gallium, and silicon fluxes were provided by conventional effusion cells and the magnesium flux was provided by a Veeco corrosive valved cracker. Nitrogen was provided by a Veeco UNI-Bulb radio frequency (RF) plasma source with an RF power of 350 W and a gas flow of 1.25 SCCM. For the initial doping study, n-AlGaN films were grown with a thickness of 500 nm and p-AlGaN films were grown with a thickness of 100 nm. For the diode growths, 100 nm of AlN was grown initially to bury remaining contaminants and then the diode structure was grown, with the structural details being provided in the relevant sections below.

For Hall Effect measurements, standard In dot contacts were applied to the corners of each sample and the measurement itself was performed with a LakeShore M91 FastHall system. SIMS measurements were performed by Evan's Analytical Group. For the diodes, mesa the mesa defining etch was performed with an ICP plasma etch tool using a Cl based plasma chemistry. Contact metal stacks were deposited via e-beam evaporation and IV measurements were taken on

a standard probe station. LED growth and fabrication was performed by the Asif Khan group at the University of South Carolina.

4.3 Results and Discussion

4.3.1 Hyper doping of AlxGa1-xN thin films

While MME has been successful in improving doping of GaN and AlN, a further study must be performed to investigate how well the extreme doping capability of MME translates to AlGaN. A series of $Al_xGa_{1-x}N$ films were grown either p doped with a Mg concentration of 3.4E20 cm^{-3} or n doped with a Si concentration of 1.3E20 cm^{-3}. For each dopant, four films were grown with an Al concentration between 0% and ~60% Al. The 0% Al (GaN) films were the same films used in the previous study to establish compensation limits.

Figure 4.1 displays carrier concentration (a), resistivity (b), and mobility (c) of the silicon doped $Al_xGa_{1-x}N$ films. Secondary ion mass spectroscopy (SIMS) measurements showed a silicon concentration of 1.3E20 cm^{-3} for this silicon condition, as discussed above. Electron concentration is shown in Figure 4.1a and decreases from 1.84E20 cm^{-3} for n-GaN to 3.8E19 cm^{-3} for $Al_{0.64}Ga_{0.36}N$, a decrease of about a factor of 5. The resistivity values (Figure 4.1b) trend the opposite of the carrier concentrations, increasing by over two orders of magnitude between x=0 and x=0.64. Mobility also decreases by over an order of magnitude over the same compositional shift. These resistivity and mobility trends match well with the expectations that films will become generally more resistive as one moves away from GaN and more towards AlN. The silicon

activation efficiency decreased from ~100% for x=0 to ~29% for x=0.64, yielding high electron concentrations and highly conductive n-$Al_xGa_{x-1}N$ films.

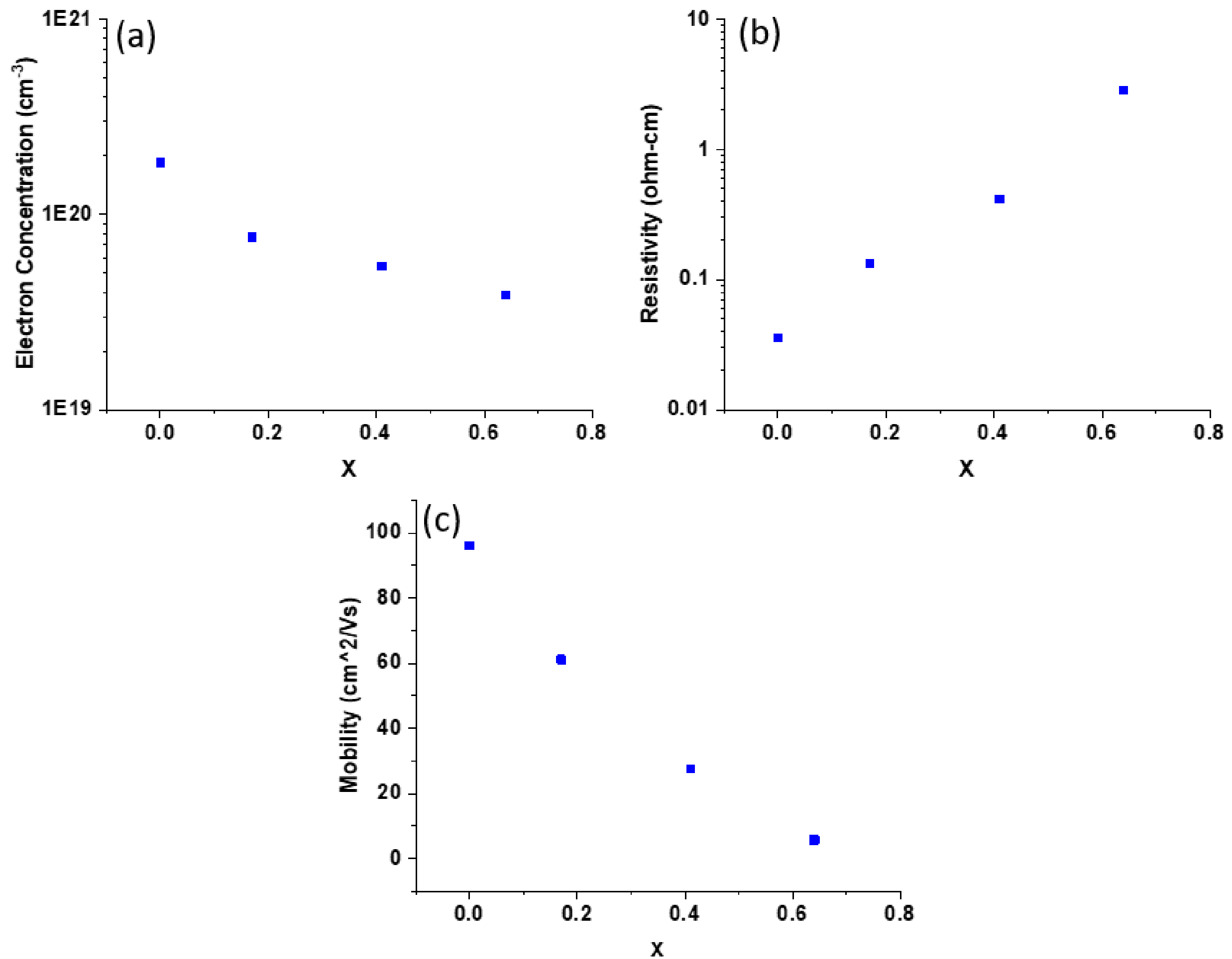

Figure 4.1: (a) Electron Concentration, (b) Resistivity, and (c) Mobility for four $Al_xGa_{1-x}N$ films of different compositions. Doping efficiency decreases with increasing Al content.

Figure 4.2 shows the hole concentration (a), resistivity (b) and mobility (c) of the Mg doped series. Secondary ion mass spectroscopy measurements yield a Mg concentration of 3.4E20 cm^{-3}

as discussed above. The hole concentrations, as shown in Figure 4.2a, range from 1.5E20 cm^{-3} at x=0 to 3.6E15 cm^{-3} for x=0.52, a decrease of nearly 4 orders of magnitude, a drop far steeper than the electron concentrations for the Si doped series. with an activation efficiency ranging from 44% at x=0 to 0.001% at x=0.52. Due to the atomic radius of Mg (145 pm) it is expected that it will be more difficult to include Mg as Mg_{Al}, a substitutional impurity which is the acceptor impurity form of Mg, as one shifts from GaN (Ga atomic radius of 136 pm) to AlN (Al atomic radius 118 pm). Furthermore, the activation energy is expected to increase 3-4x as the composition shifts from GaN to AlN. Thus the steep decrease in activation efficiency for Mg in AlGaN matches the expected trend from theory.[185] The resistivity (Figure 4.2b) increases by nearly 2 orders of magnitude when changing the composition from x=0 to x=0.52, and the mobility decreases by nearly 75% from x=0 to x=0.41. The x=0.52 sample shows an increase in mobility over the x=0.41 sample, but this data point must be looked at with skepticism because van de Pauw measurements were plagued by high contact resistance, but Hall measurements were not (see reference 25 for details for a similar Hall study). The presence of such high contact resistance hinders van de Pauw resistivity measurements making the extraction of the mobility from unaffected Hall Measurements prone to error. The significant inclusion of non-activated Mg within the film accounts for the increased resistivity and decreased mobility for the Mg doped series vs the Si doped series.

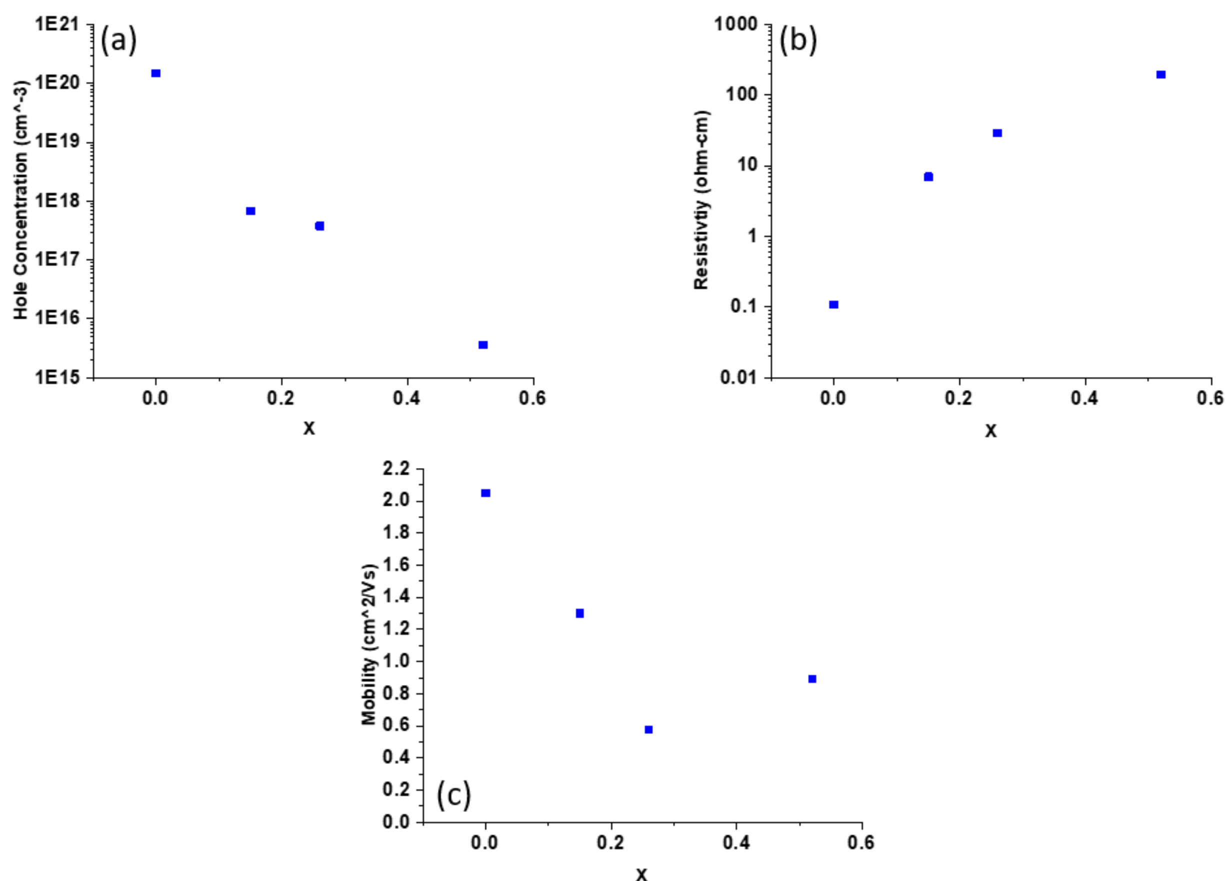

Figure 4.2: (a) Hole Concentration, (b) Resistivity, and (c) Mobility for four $Al_xGa_{1-x}N$ films of different compositions. Doping efficiency decreases with increasing Al content.

4.3.2 Realization of an AlGaN Homojunction Tunnel Diode

Having demonstrated the ability to achieve high doping levels in AlGaN, it is now desirable to assess the application of this doping in devices. To facilitate this, an $Al_{0.08}Ga_{0.92}N$ pn diode structure was grown, illustrated in Figure 4.3. This structure was selected to assess the IV characteristics for potential tunneling behavior, a phenomenon only possible with ultra-high n and p type doping levels within the junction. The band to band tunneling probability within a diode is expressed by equation 2. There are three variable material based factors within this equation. These are: the effective mass of the carrier (electrons in this case), which is an intrinsic material property

determined by the AlGaN compositions, the built-in voltage of the junction, again a material property determined by the AlGaN composition, doping concentrations and thus, the depletion width. For a given AlGaN composition the effective carrier mass is constant, therefore in order to increase the tunneling probability the depletion width and built-in voltage, both dependent on doping, must be improved. I note that the built-in voltage is a slowly varying logarithmic function of doping. Thus, I focus on the depletion width. Increasing the dopant concentration, both n and p type, within a junction will decrease the depletion width, resulting in an exponential increase in tunneling probability. Thus, if the doping is high enough in the $Al_{0.08}Ga_{0.92}N$ junction, tunneling behavior should be observed.

Equation 2: Tunnelling probability for carriers in a junction.

$$T = exp\left(\frac{-4\sqrt{2m_e q(V_{bi} - V)}}{3w\hbar}\right)$$

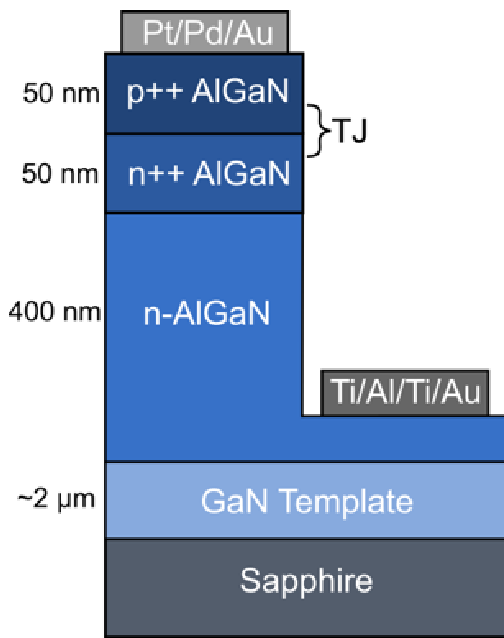

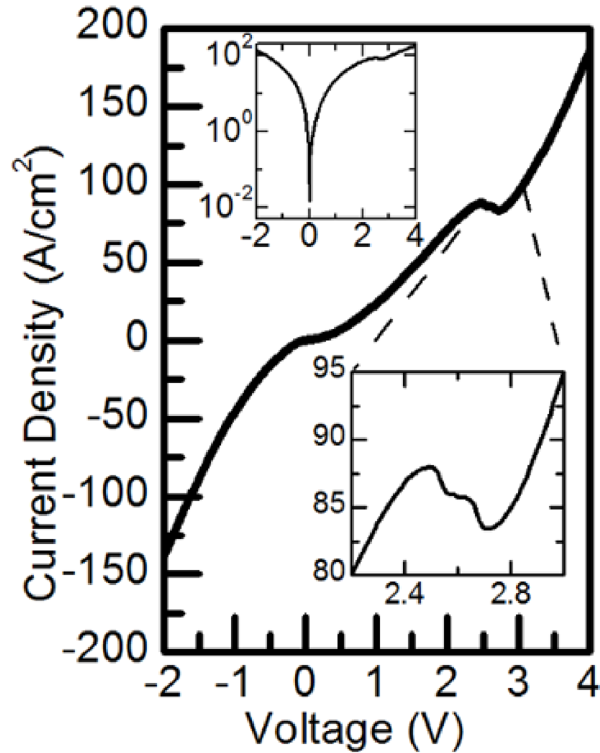

Figure 4.3: Tunnel diode structure (left) and J-V curve of the $Al_{0.08}Ga_{0.092}N$ homojunction tunnel diode.

Figure 4.3 shows the J-V curve of the $Al_{0.08}Ga_{0.92}N$ pn diode shown to the left. The J-V curve shows two distinct signs of tunneling. The first is negative differential resistance (NDR) in forward bias and the second is high reverse bias current. Negative differential resistance appears as a direct result of tunneling. As forward bias is applied the band alignment in the junction will shift. At low voltages current will conduct via tunneling, resulting in a standard diode IV curve to start. As the voltage increases, the band will enter a state of misalignment in which tunneling is more difficult, resulting in an increase in resistance and a reduction in current, represented in the forward bias NDR region. As voltage is increased further normal diode operation will take over and the current will resume increasing. Therefore, the presence of NDR in the J-V curve is a clear sign of tunneling in the diode. The reverse bias behavior provides even more evidence to this

tunneling behavior. As a result of tunneling pathways for current, within a tunnel diode high reverse bias current is observed, higher at -1.5 volts than for forward bias at +1.5 volts. This diode result confirms the ultra-high doping level within AlGaN, although this initial study only investigates a low Al content of 8%.

4.3.3 Investigation of Tunneling Behavior in High Al Content Devices.

While the initial study demonstrated tunneling behavior as a result of ultra-high doping in an 8% Al tunnel diode, it is desirable to push this tunneling application towards higher Al contents. While this was the first demonstration of a homojunction AlGaN tunnel diode, $Al_{0.08}Ga_{0.92}N$ would correspond to an emission wavelength of only ~340 nm. Modern AlGaN optoelectronic devices are pushing as deep into the UVC range and therefore require high Al content films. Section 4.3.1 demonstrated the application of MME in pushing ultra-high doping of AlGaN films, even in high Al content ranges. In order to assess the application of this doping in higher Al content devices, a series of pn and pin diodes were grown and fabricated, with the structures being illustrated in Figure 4.4. Structure A is a control pin diode intended to provide baseline data on rectification, reverse bias leakage, and forward bias characteristics. Structure B is a pn tunnel diode intended to assess tunneling characteristics of the ultra-high doped AlGaN devices. Each structure was grown with a composition of 19, 42, or 58 % Al, with one of A and B being growth at each composition for comparison.

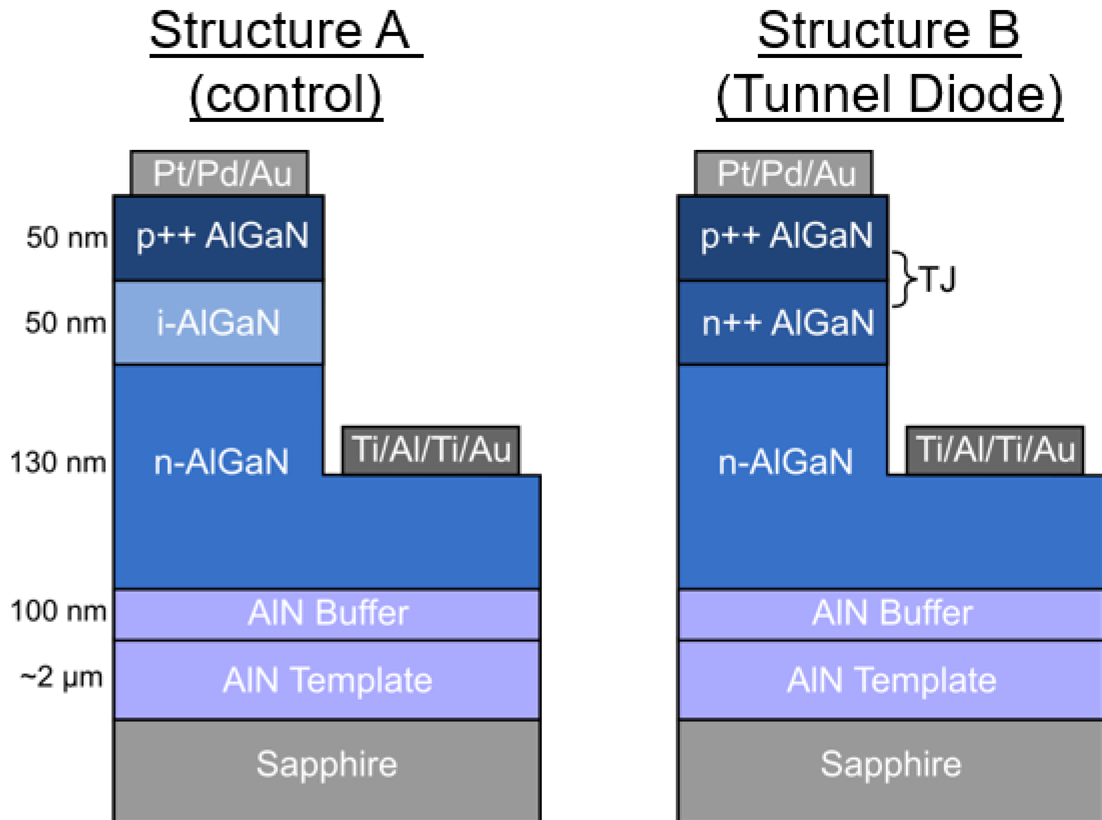

Figure 4.4: Structure of the control AlGaN homojunction PIN diodes (left) and the tunnel diode (right).

Figure 4.5 shows the J-V curves for the 6 diodes, separated by composition. In all cases the two types of diodes show greatly different characteristics, although the behavior of the diodes changes with composition. At the lowest Al content of 19 %, the pn diode shows the clearest signs of tunneling, with high reverse bias tunneling current and NDR in the forward bias, similar to the previously discussed $Al_{0.08}Ga_{0.92}N$ tunnel diode. In contrast, the pin diode shows significantly different characteristics, with 3-4 orders of magnitude rectification and reduced current at lower forward voltages. The characteristics shift when increasing to 42% Al. The pn diode in this case still shows high reverse bias tunneling current. In forward bias, the diode does not show full NDR, but does show a kink suggesting a change in resistance as a result of tunneling behavior. In

addition, the control pin diode shows ~2 orders of magnitude higher rectification in reverse bias, suggesting that the reverse bias current of the pn diode is indeed the result of tunneling. Further change is observed when moving to 58 % Al. At this point the forward bias no longer shows any signs of NDR, but the reverse bias still shows high current. While one could suggest this to be the result of leakage current, the control pin diode shows ~4 orders of magnitude of rectification over the pn diode, suggesting that the reverse bias current is indeed the result of tunneling current. These results show that ultra-high doping of AlGaN can enable new device applications even up to an Al content up to nearly 60% Al.

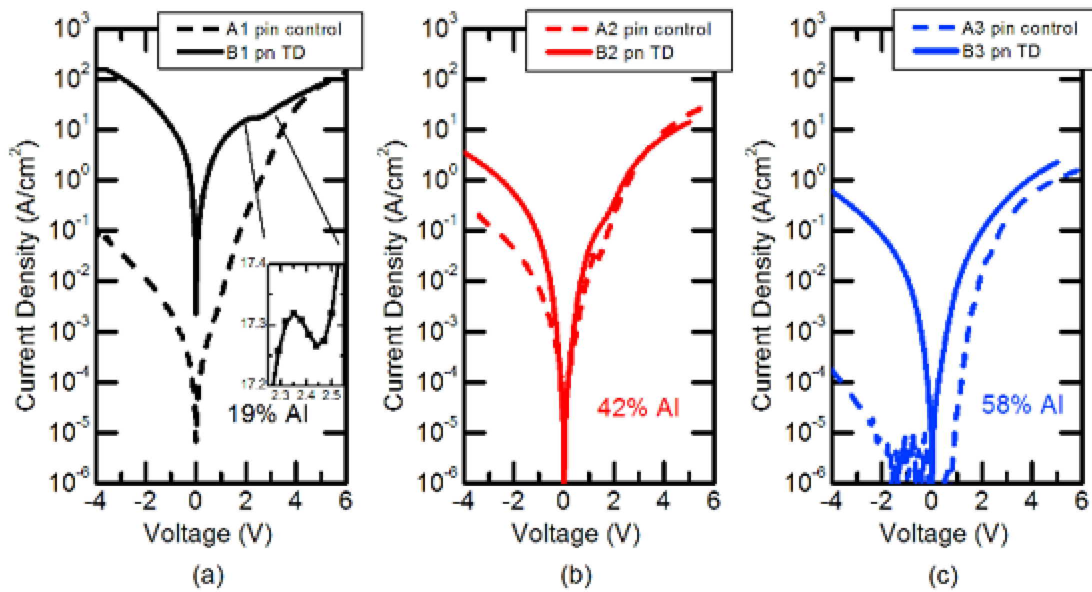

Figure 4.5: JV curves of the homojunction AlGaN tunnel diodes with compositions of 19 (left), 42 (middle), and 58 (right) % Al.

4.3.4 Utilizing AlGaN Tunnel Contacts to Improve UV LEDs

To prove the utility of the AlGaN tunnel junctions, they were applied to AlGaN based UV LEDs as contacts to assess the performance of such a contact over traditional GaN contacts where it is expected that the utilization of AlGaN based contacts will improve emission over GaN based contacts by reducing or eliminating parasitic absorption. In this case, two LEDs were grown by the group of Dr. Asif Khan at USC. One of the LEDs was fabricated as is with a traditional p-GaN top contact, while for the other I deposited an AlGaN tunnel contact pre-fabrication, with the structures being shown in Figure 4.6. Post-fabrication, electroluminescence was performed on both the LED structures to measure the light output. Figure 4.7 displays the EL spectra showing sharp emissions at 273 and 276 nm for the control and TC LED respectively. The difference in emission wavelengths is likely the result of minor growth variations and not the contact schemes. Figure 4.8 displays the light output power curve of the two LEDs. A significant improvement can be seen when using a tunnel contact over the traditional p-GaN contact, with a doubling of the output power at 7.5 mA. This result shows that the use of an AlGaN based tunnel contact indeed reduces output loss due to parasitic absorption and results in great improvement over GaN based contacts.

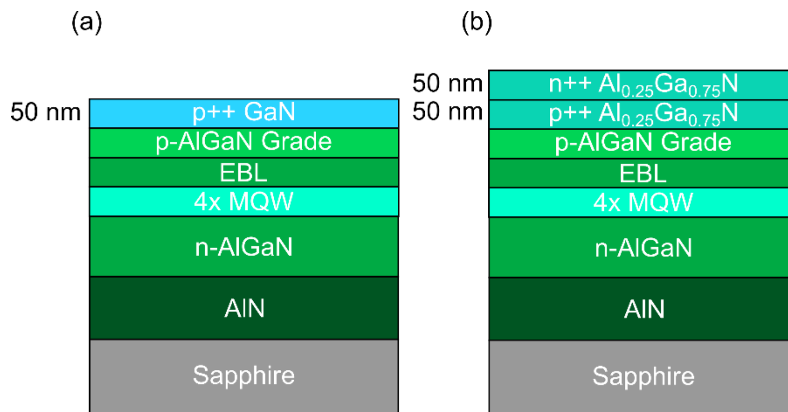

Figure 4.6: Structure of the test AlGaN based UV LED with a traditional p-GaN contact layer (left) and structure of an AlGaN based UV diode with an AlGaN tunnel contact.

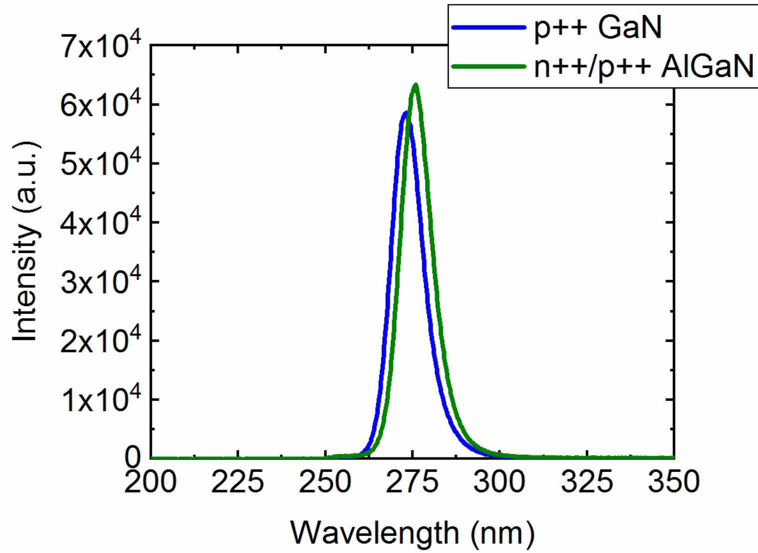

Figure 4.7: EL spectra of the control and tunnel contacted LEDs, showing an increase in intensity for the tunnel contacted device.

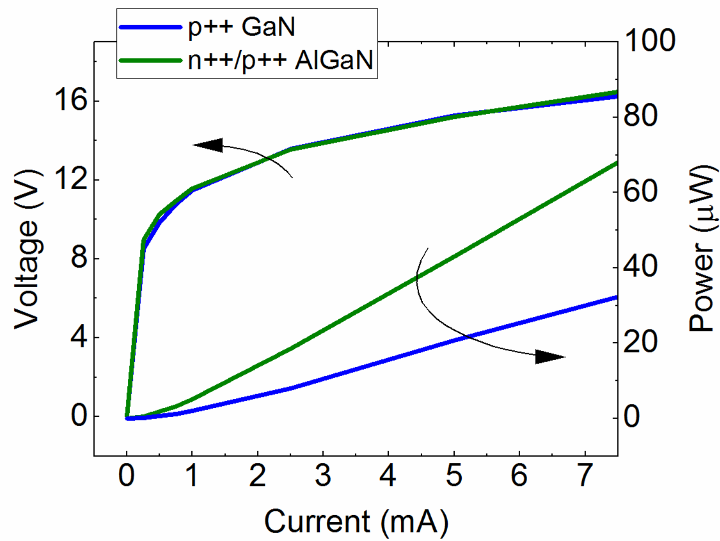

Figure 4.8: Light output power for the control and tunnel contacted LEDs showing a significant increase in output power for the tunnel contacted device.

4.4 Conclusion

Hyper doping of AlGaN was enabled via metal modulated epitaxy. A decrease in electron concentration from n-GaN of less than an order of magnitude was observed via Si doping when increasing the Al content to 64%, reducing from 1.8×10^{20} to 3.8×10^{19} cm^{-3}. On the other hand, hole concentrations decreased from 1.5×10^{20} to 3.6×10^{15} cm^{-3} when shifting from p-GaN to $Al_{0.52}Ga_{0.48}N$. This hyper doping of AlGaN enabled tunnel junctions to be fabricated with Al contents up to 58%, with NDR being observed up to 19% Al. Even lacking NDR, higher Al content tunnel diodes demonstrated significant reverse bias tunneling current. Finally, such structures were applied as tunnel contacts to a UV LED emitting at 273 nm, resulting in an increase in output power of over 110% compared to a traditional p-GaN contact at 7.5 mA.

CHAPTER 5. ADLAYER CONTROL FOR TUNABLE ALGAN SELF-ASSEMBLED SUPERLATTICES

5.1 Introduction

In recent years the $Al_xGa_{1-x}N$ material system has received significant study due to its many desirable traits, such as a tunable and wide band gap, high polarization in AlGaN/GaN and AlGaN/AlN heterojunctions, strain mitigation as a buffer layer, and high radiation hardness.[184,186–189] The quality of $Al_xGa_{1-x}N$ films has rapidly improved and is most commonly grown using metal organic chemical vapor deposition (MOCVD) and molecular beam epitaxy (MBE), allowing the creation of state-of-the-art devices such as high performance high electron mobility transistors (HEMTs) and high performance ultraviolet (UV) light emitting diodes (LEDs) and laser diodes (LDs).[190–194] The tunable bandgap of AlGaN from 3.4 eV (GaN) to 6.1 eV (AlN) allows the fabrication of light emitting devices in the range of ~365-200 nm, deep into the UV spectrum. Indeed, many have demonstrated high performance UV LEDs, operating even into the UVC range[8–11] which has led to considerable interest for these devices due to their ability to sterilize against viruses and bacteria.

$Al_xGa_{1-x}N/Al_yGa_{1-y}N$ ($x \neq y$) superlattices (SLs) have seen substantial research and development as well. Significantly, $Al_xGa_{1-x}N/Al_yGa_{1-y}N$ ($x \neq y$) superlattices have been used as a buffer layer to produce crack free, thick AlGaN films in heteroepitaxy.[189,195] $Al_xGa_{1-x}N/Al_yGa_{1-y}N$ ($x \neq y$) SL structures have also been used as electron blocking layers in UV LEDs[183,196] , as well as current injection and multi-quantum well layers for the same.[103,107,175,197] Further, while not technically superlattices, $Al_xGa_{1-x}N/Al_yGa_{1-y}N$ ($x \neq y$) periodic structures with thicker layers can be

applied to form high reflectivity distributed Bragg reflectors (DBRs).[198–200] Additionally, the polarization within such structures has been engineered to generate 2-dimensional hole gasses (2DHGs) to create polarization-doped structures.[182,187,201] $Al_xGa_{1-x}N/Al_yGa_{1-y}N$ ($x \neq y$) SLs have also been applied to improve the quality of GaN layers grown on non-native substrates.[202] However, despite the wide benefits and usage of $Al_xGa_{1-x}N/Al_yGa_{1-y}N$ ($x \neq y$) SLs, they pose several epitaxial challenges.

Since superlattices consist of two separate materials, it is often difficult to optimize the fabrication of both layers. If one were to traditionally grow an $Al_xGa_{1-x}N/Al_yGa_{1-y}N$ ($x \neq y$) superlattice, each layer would require different metal fluxes and, potentially, different thermal conditions to grow an optimal combination. Thus, if one does not have two separate sources for each Al and Ga, to achieve an atomically abrupt interface, a growth interrupt would be required between each SL layer to adjust flux, and substrate temperature if necessary. It is well known that growth interrupts lead to unintentional accumulation of contaminants at the interface at which the interrupt occurred and can lead to a loss of optical emission or even introduction of structural defects.[203] A second problem with growth interrupts during the formation of such a SL is the introduction of strain. While this strain can be beneficial in buffer layers where bending of dislocations outward through strain relaxation is desirable, it can also result in plastic deformation that periodically introduces new defects along the structure. Given the tendency of increased relaxation during annealing, the use of growth interrupts exaggerates the plastic deformation problem. If a method can be developed to create a repeated and consistent superlattice through uninterrupted growth, these issues can be eliminated. In this paper we apply metal modulated epitaxy (MME) to demonstrate the formation of self-assembled superlattice (SASL) AlGaN structures, providing such a method with a simple epitaxial technique.

Using metal rich growth methods, like MBE and MME, additional metal adlayers are known to form.[142] When growing ternary compounds with MME, we have observed the spontaneous formation of SASL structures when the excess metal dose exceeds that necessary to form a single monolayer. For example, Figure 5.1 shows a bright-field transmission electron microscopy (TEM) image in a two-beam condition g = [0 0 0 2] and corresponding X-ray diffraction (XRD) 2θ-ω scan of a large, exceptionally coherent SASL of 830 nm thickness grown with a III/V ratio of 1.3 (excess metal flux of 30% compared to nitrogen), a shutter open time of 14 s per cycle, and an instantaneous growth rate of 2.4 μm/hr**.** The TEM image shows clearly defined wells of higher gallium content (dark regions) and barriers of higher Al content (light region) with abrupt interfaces between the two. The coherence is substantial. The period thickness in the TEM image is about ~11 nm, close to the thickness acquired by XRD simulation of the structure of 10.2 nm. Combined, these prove that this MME technique is capable of rapidly growing abrupt, coherent superlattice structures with no growth interruptions. The purpose of this study is to develop the supporting design criteria to control the period, well and barrier thicknesses, and compositions, and to define the limitations of this approach.

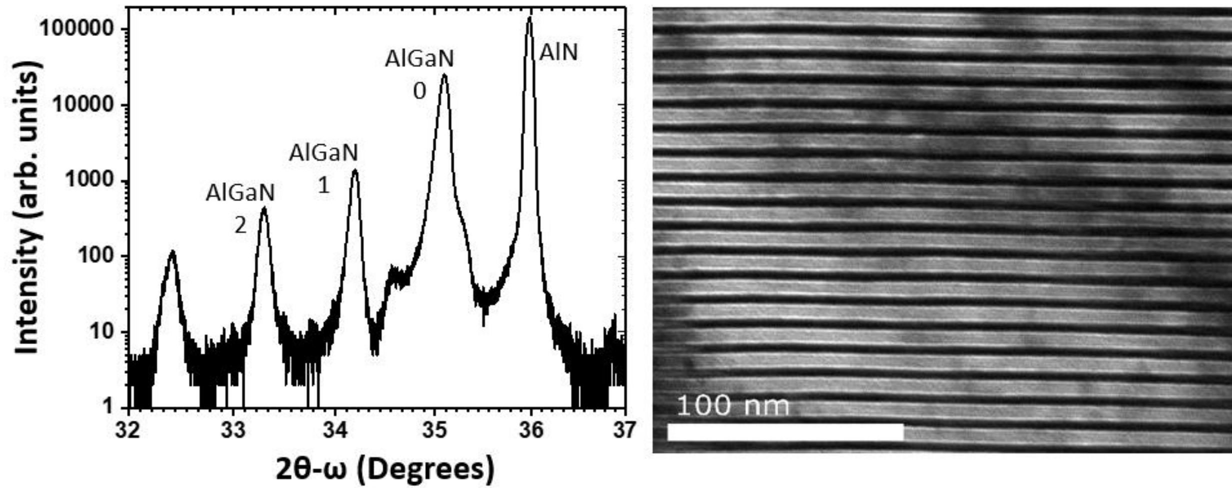

Figure 5.1: XRD 2θ-ω scan (left) of a SASL. Cross sectional TEM image of the same (right). Both show exceptional coherency and abrupt interfaces.

5.2 Experimental

All films in this study were grown in a Riber 32 MBE reactor using the MME technique, the details of which can be found elsewhere.[142,143,181] All samples were grown on 1 cm × 1 cm hydride vapor phase epitaxy (HVPE) AlN on sapphire templates. The substrates were single-side polished and 2 μm of tantalum was sputtered on the backside to facilitate uniform heat absorption during growth. Prior to growth the substrates were cleaned using a 3:1 solution of H_2SO_4:H_2O_2. This clean was followed by a rinse with DI water and a brief dip in dilute HF to reduce surface oxides, after which the sample was again rinsed with DI water and dried with N_2. After the chemical cleaning procedure, the samples were loaded into an introductory vacuum chamber with a base pressure of ~1×10^{-9} Torr in which they were outgassed at 200 °C for 20 minutes. Prior to

growth, the samples were further outgassed at 800 °C in the growth chamber. Following the outgas, the samples were further cleaned using three cycles of gallium adsorption and desorption to further remove oxygen from the surface.[142]

During growth, aluminum and gallium were provided by a conventional effusion cell. An AlN buffer layer was grown prior to the AlGaN layers using MME with a III/V ratio of 1.3 and a shutter open/close scheme of 21s/11s. MME is described in detail in references 29, 32, and 33.[23,142,204] During AlGaN growth the Al and Ga shutters were shuttered synchronously. All AlGaN films were grown using the MME technique with varying III/V ratios, shuttering timing, and instantaneous growth rates with a fixed substrate temperature of 725 °C. The global average growth rate is the film thickness divided by the total growth time. But since there are periods of no growth in each cycle (called the dead time and observed in reflection high energy electron diffraction (RHEED) as a predominantly flat specular spot intensity described in detail in reference 29, 32, and 34)[23,24,142], we define an instantaneous growth rate as the thickness grown while metal is exposed to the surface divided by the time metal is exposed to the surface. The metal is exposed to the surface while the shutter is open and while excess accumulated metal is being consumed after shutter closing. Said another way, the instantaneous growth rate is (the deposited material thickness per cycle) / (the cycle time minus the dead time per cycle). For each MME shutter cycle where desorption can be ignored this instantaneous growth time is the shutter open time multiplied by the III/V ratio. The thickness of the AlGaN SASL layers are rather thick, being ~400 nm when grown with an instantaneous growth rate of 1.3 μm/hr and ~910 nm when grown at 2.8 μm/hr unless specifically stated otherwise. Nitrogen was provided by a Veeco UNI-Bulb radio frequency (RF) plasma source with an RF power of 350 W and a gas flow of 2.5 sccm for instantaneous growth rates of 1.3 μm/hour and 6 sccm for 2.8 μm/hour instantaneous growth rates.

In situ surface monitoring was performed using (RHEED) to calibrate III/V ratio and metal doses and post-growth XRD analysis was performed with a Philips X'pert Pro MRD using a Cu Kα1 anode. XRD simulations were performed with the X'pert Epitaxy and Smoothfit software. TEM measurements were performed using an F30 FEI Tecnai. Photoluminescence (PL) measurements were performed at room temperature with a Renishaw Raman Spectrometer with an excitation wavelength of 266 nm.

5.3 Results and Discussion

5.3.1 Effects of Metal Dose on SASL Formation

For comparison, a number of AlGaN films were grown under otherwise identical growth conditions with a III/V ratio of 1.3 and an instantaneous growth rate of 1.3 μm/hr, varying only the metal dose, via shutter open time, to study the effect of metal adlayer build up on the formation of SASLs during the growth. The assumed mechanism for SASL formation being any metal not consumed during the shutter open period will be consumed during the shutter closed period. Since Ga and Al have different incorporation rates owing to different chemical bond strengths of Ga-N and Al-N bonds in AlGaN, the composition of the film grown in the open period will differ from the composition grown in the closed period (further discussed below). Figure 5.2 displays four XRD 2θ-ω scans AlGaN films grown with a metal dose varying from 3 s to 20 s. Simulations were generated for all XRD 2θ-ω scans to determine the superlattice period, the individual layer thickness, and the individual layer composition. The sample grown with a 3 s metal dose produces a single phase $Al_{0.55}Ga_{0.45}N$ film which closely matched the flux ratio between Al and Ga within the error expected for Ga surface desorption (~5% at these temperatures). In this case, the metal dose is too low to accumulate excess metal on the surface beyond a single monolayer and thus, too

low to allow the formation of a superlattice in the film. The 10 s to 20 s films show satellite peaks corresponding to superlattice formation. The periods of the superlattices are 4.6 nm, 6.4 nm, and 9.1 nm for a metal dose of 10 s, 14 s, and 20 s, respectively. The individual layer thicknesses and compositions are shown in Table 1. In analogy to a simple quantum well, the thinner, lower Al composition layer in the superlattice will be referred to as the well and the thicker, higher Al composition layer will be referred to as the barrier. It should be noted the ratio of well thickness to barrier thickness remains constant for the 10 s to 20 s metal doses, with the well being about 30% the thickness of the barrier as shown in Table 1. This is set by the III/V ratio of 1.3. One metal dose cycle consists of two sections: first a "shutter open phase" in which Al and Ga metal fluxes are simultaneously applied to the surface for a specified time resulting in a total metal dose (flux x time) along with an active nitrogen source also impinging; and second a "consumption phase" in which the metal fluxes are cut off and the nitrogen is allowed to consume the remaining surface metal into the semiconductor film. At a III/V ratio of 1.3 the metal flux applied during the shutter open phase will be 1.3x that of the nitrogen flux. As a result, the consumption phase will last for 30% of the time of the metal open phase. The ratio of well thickness to barrier thickness along with this fact suggests that the well is grown during the consumption phase and the barrier is grown during the shutter open phase, and thus the thickness of the well is controlled by III/V ratio. We note that the compositions of the well and barrier are different because Al is preferentially grown into the film compared to Ga because the Al-N bond strength in AlGaN is stronger than the Ga-N bond strength in AlGaN. Thus, the metal remaining on the surface after the barrier is grown (at the end of the shutter open time) is Ga-rich leading to a lower Al composition well as described in more detail below.

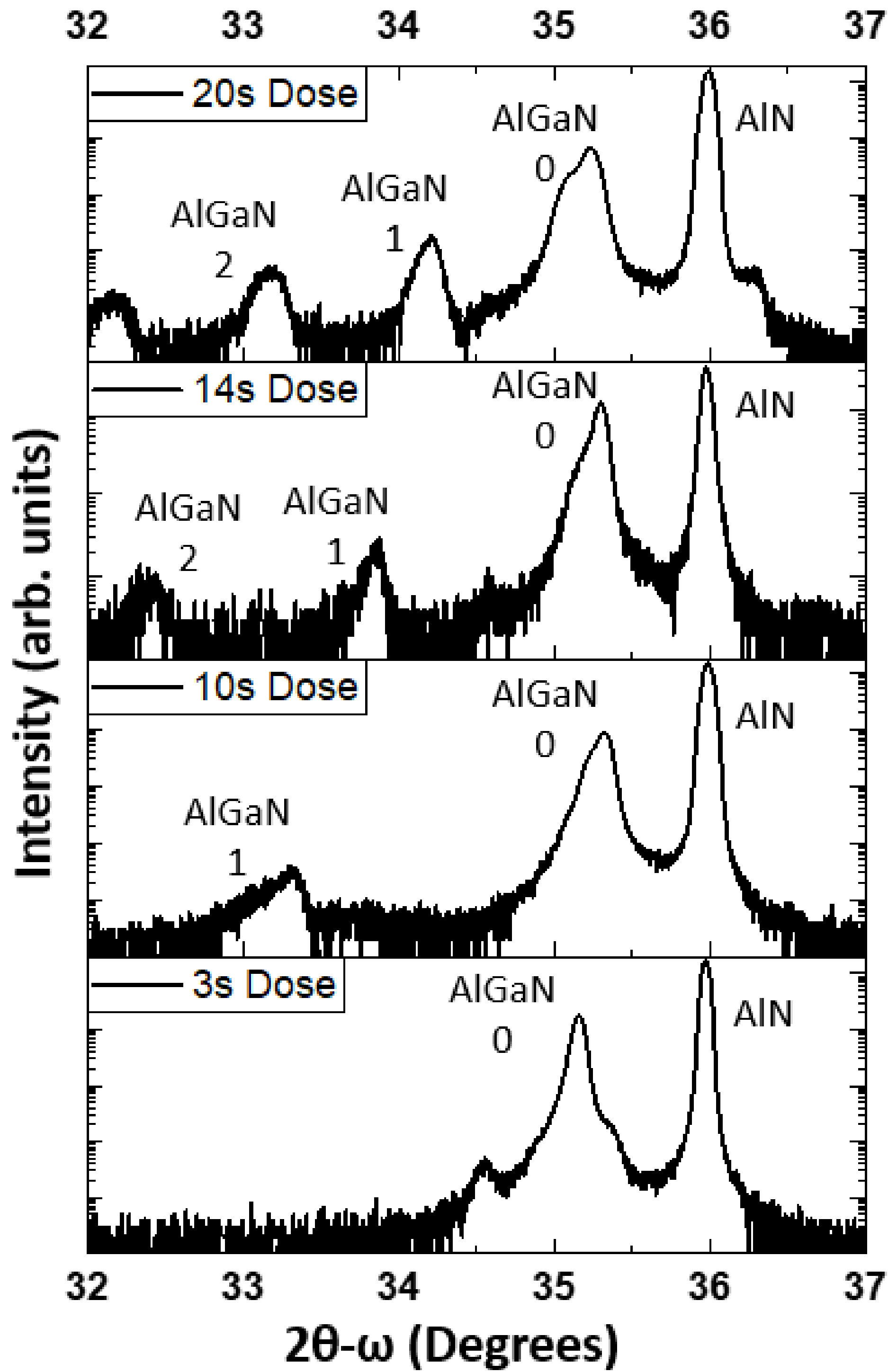

Figure 5.2: XRD 2θ-ω scans of four AlGaN films grown with varying metal doses used to control the SASL period.

Table 5.1: Parameters extracted from XRD simulations where four AlGaN films grown with four different shutter open times are compared.

Sample ID	Shutter Open Time (s)	Average Well Al %	Well Thickness (nm)	Average Barrier Al %	Barrier Thickness (nm)	SL Period (nm)	$T_{well}/T_{Barrier}$
D1	3	N/A	N/A	N/A	N/A	N/A	N/A
D2	10	31	1.0	66	3.5	4.5	0.29
D3	14	18	1.5	70	4.9	6.4	0.31
D4	20	8	2.1	67	7	9.1	0.30

The formation of these superlattices is due to an excess buildup of metal layers and cation exchange between them. During an MME cycle, three metal "layers" can be built up, depending on the total metal dose supplied: An initial pseudomorphic (PM) monolayer, a secondary laterally contracted (LC) monolayer, and at high doses, a three dimensional random droplet layer.[142,205,206] The semiconductor film forms when nitrogen diffuses down to the PM/substrate interface and

forms a bridging bond, solidifying the AlN or GaN molecule into the growing semiconductor film. Due to the higher bonding strength of the Al-N bond vs. the Ga-N bond in AlGaN, Al-N bonds will be preferably formed, leaving the Ga to accumulate in concentration in the PM layer. However, the lattice constant of the PM layer should closely match the lattice constant of the underlying semiconductor film. When Ga accumulates in the PM layer, the liquid-like PM layer becomes strained to the substrate and the rejection of Ga to the LC layer through segregation is energetically preferred. Metal atoms can move between the three surface metal layers and as a result, aluminum atoms will be pulled into the PM monolayer, being the one at the growth front, depleting the aluminum within the LC monolayer and the droplets. Once the metal shutters are closed and the metal supply is cut off, gallium rich layers are incorporated by the nitrogen flux consuming all remaining surface metal as evidenced by the superlattice fringes present in Figure 5.2 for the 10 to 20 s metal dose samples. This vertical phase segregation can be eliminated in MME by limiting the metal dose in the shutter open phase which eliminates the LC and droplet layer formation. The amount of metal build up, and thus which layers are formed, can be varied by controlling the metal dose. If the metal dose is limited so that only a PM monolayer can be formed, there will be no other layers for metal atoms to transfer between and thus the semiconductor growth will homogeneously proceed by building up a single PM monolayer and then consuming it, growing a single composition layer per MME cycle and negating any potential for vertical phase separation, as is seen in Figure 5.2 for the 3 s dose sample. Thus, one can control whether or not the SASL forms at all, and the layer thickness and period of a SASL in MME by precise control of the metal buildup in the shutter open phase.

Of further interest is the effect of the metal dose on the Al content of the well and barrier layers. It can be observed that the effect of dose on the barrier layer is minimal, with there only

being a change of 4% between the lowest and highest composition barrier. This near constant Al composition can be understood by the lattice matching and thus, minimal strain, of the PM layer and the underlying film. This minimal strain condition forces Ga upward into the LC and droplet layers while pulling Al downward to replace the Ga in the PM so as to maintain a constant PM lattice constant closely matching the underlying film. This Al pulling effect results in a near constant barrier composition as long as Al flux is resupplied at a sufficient rate to satisfy the downward flux of Al from upper layers toward the PM layer. However, there is a significant change in the Al composition of the well layer, with the 10 s dose SASL having an Al content of 31%, decreasing to 8% for the 20 s dose SASL. This sudden change in composition results when the replenishing supply of Al is interrupted upon shutter closing. During the shutter closed period, the accumulated Ga-rich LC and Droplet layers are consumed into the film by the nitrogen flux and in the process a strained PM layer (Al deficient compared to the underlying barrier film) momentarily forms and is consumed into the solid. Thus, in the case of metal rich growth, the composition of the barriers is set by the rate of growth (determined by the N flux) versus the rate of Al supply, with the Ga simply filling in what is needed to complete the PM layer.

In order to assess the optical quality of the wells formed by the SASL growths, room temperature photoluminescence (PL) measurements were performed on the 10, 14, and 20 s dose structures, as displayed in Figure 5.3. As expected, the emission peak shifts consistently with the composition of the well. The peak shifts from ~4 eV with a 10 s dose (31% Al well), to ~3.7 eV with a 14 s dose (18% Al well), to ~3.5 eV with a 20 s dose (8% Al well). All three spectra additionally show strong Fabry-Pérot interference fringes resulting from a cavity thickness between 4 and 5 microns, corresponding well to the thickness of the underlying AlN substrate. The PL linewidth is broadened by the large number of wells present and though the number of wells is

beyond that which would be typically applied in a multi-quantum well (MQW) LED or LD structure (44, 63, and 88 wells for 20, 14, and 10 s dose respectively), such emission energy control for SASL formation would be useful for such devices at lower well numbers.

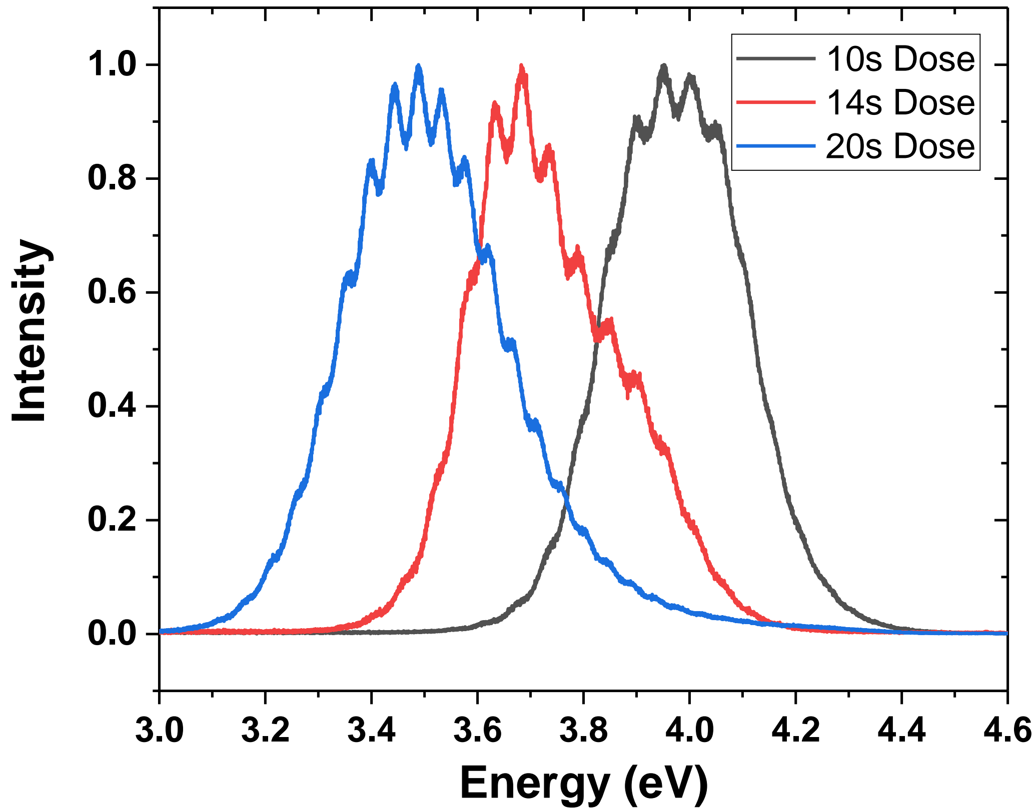

Figure 5.3: Room Temperature PL spectra of AlGaN SASL structures grown with a 10, 14, and 20 s dose showing control of emission energy.

5.3.2 Effects of III/V Ratio on SASL Parameters

To investigate the effect of the III/V ratio, and thus the ratio of shutter open time to consumption time, on the ratio of well thickness to barrier thickness, another set of films were grown using the same shutter open time of 14 s and instantaneous growth rate of 1.3 μm/hr but varying the III/V ratio from 1.3 to 1.8. The XRD 2θ-ω scans are displayed in Figure 5.4. Again, XRD simulations were performed to extract the SL period, layer thickness, and layer composition

and the results are shown in Table 2. It can be seen that the thickness of the well increases from 30% of the barrier at a III/V ratio of 1.3 to 80% of the barrier at a III/V ratio of 1.8. The increase in well thickness without any significant change in barrier thickness confirms that the barrier is formed during the shutter open time and the well forms during the consumption time.

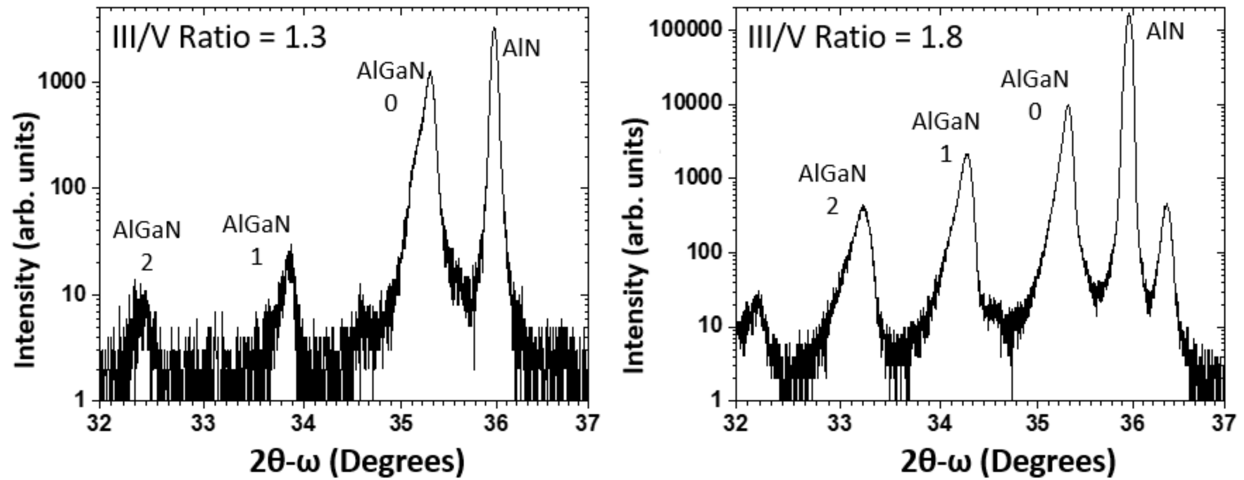

Figure 5.4: XRD 2θ-ω scans of two AlGaN films grown with varying III/V ratios showing control over the well to barrier ratio.

Table 5.2: Parameters extracted from XRD simulations where two AlGaN films grown with two different III/V ratios are compared.

Sample ID	III/V Ratio	Average Well Al %	Well Thickness (nm)	Average Barrier Al %	Barrier Thickness (nm)	SL Period (nm)	$T_{well}/T_{Barrier}$
TF1	1.3	18	1.5	70	4.9	6.4	0.31
TF2	1.8	40	4	70	5	9	0.80

A significant change is seen in the composition of the well layers with the change in III/V ratio. Given that the barrier composition changed minimally with the change of III/V ratio, this is due to the cation exchange rate of Al atoms being independent of the III/V ratio. In other words, since the lattice-matched condition resulting in minimal strain between the semiconductor and the PM layer determines the Al composition in the PM, the amount of atomically smaller nitrogen atoms diffusing through the metal layers is of no consequence. Thus, changing from a low to a high III/V ratio changes little in the barrier. An increase in III/V ratio is purely an increase in the metal flux entering the upper two adlayers on the surface of the sample. When the Al flux entering the LC and droplet layers increases, while the cation exchange rate of Al remains constant dictated

by the minimal strain condition, then the depletion of Al in the well layer will be significantly reduced, leading to an increase in the Al content of the well, as is clearly seen in Table 2.

5.3.3 Effects of Growth Rate on the Coherency of SASL Structures

An additional study was performed to investigate the effect of instantaneous growth rate on the SASL layers. Here, two samples were grown with the same shutter open time of 14 s and III/V ratio of 1.3, but at instantaneous growth rates of 1.3 μm/hr and 2.8 μm/hr. The growth time was kept the same for both structures, yielding a thickness of ~400 nm and ~910 nm for the lower and higher instantaneous growth rate structures respectively. The XRD 2θ-ω scans are shown in Figure 5.5, with the XRD simulation extracted parameters being shown in Table 3. It can be observed that the thickness of the superlattice period and that of each individual layer scales proportionally with the instantaneous growth rate increase, an increase of about 2.2x for both instantaneous growth rate and thickness. Here, we see insignificant change in the compositions of the well and barrier layers as the shutter open time and III/V ratio are constant between the two, suggesting that the cation exchange rate does indeed scale with instantaneous growth rate. The symmetry of the peaks in the XRD scan appears to improve for the higher instantaneous growth rate SASL. In many of the previous SASL structures grown at 1.3 μm/hr, the x-ray diffraction peaks, especially the lower order SL fringe peaks, show a low angle tail, suggesting a less coherent structure due perhaps to compositional or thickness fluctuations throughout the structure. It has even been shown that such a tail can be caused by a small drift in metal flux throughout growth[207]. The higher instantaneous growth rate SASL structure appears to lack that tail, suggesting minimal variations in composition and thickness throughout the structure and good coherency, possibly due to a faster consumption of excess metal during the shutter closed cycle resulting in less vertical (along growth direction) compositional fluctuation

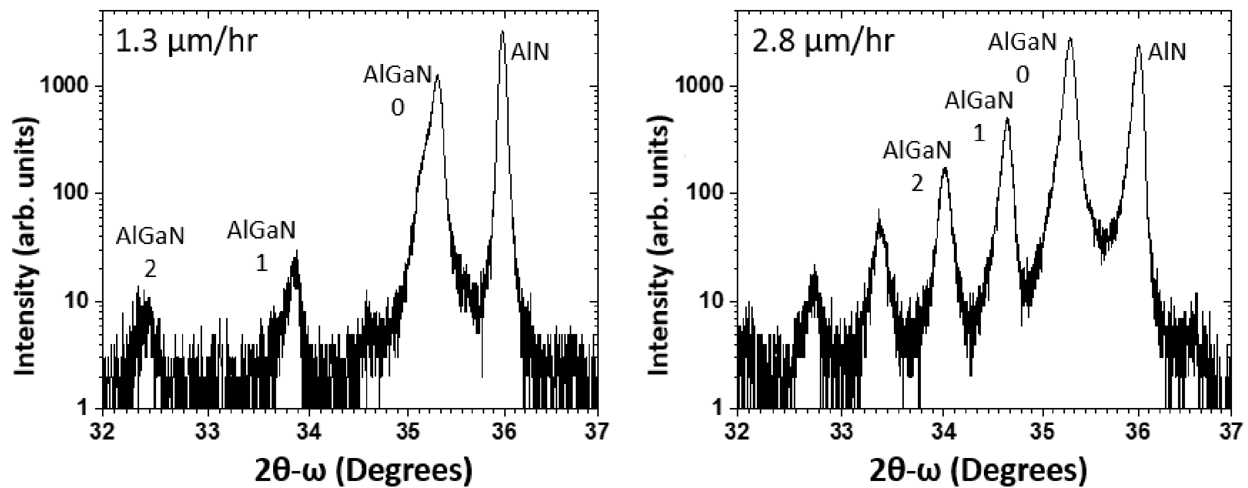

Figure 5.5: XRD 2θ-ω scans of two AlGaN films grown with varying instantaneous growth rates showing increased coherency with increased instantaneous growth rate.

Table 5.3: Parameters extracted from XRD simulations where two AlGaN films grown with two different instantaneous growth rates are compared.

Sample ID	Instantaneous growth rate (µm/hr)	Average Well Al %	Well Thickness (nm)	Average Barrier Al %	Barrier Thickness (nm)	SL Period (nm)
GR1	1.3	18	1.5	70	4.9	6.4
GR2	2.8	14	3.3	67	11.1	14.4

5.3.4 5.3.4 Methods for Control of SASL Structure Parameters

Given the above results we can specify any arbitrary SASL geometry by controlling III/V ratio, total metal dose, and instantaneous growth rate. The total SASL period is determined by the instantaneous growth rate and total metal dose as given by Equation 1

$$t_{period} = (Instantaneous\ Growth\ Rate)(Shutter\ Open\ Time)\left(\frac{III}{V}\right) \quad (1)$$

where t_{period} is the total thickness of the superlattice period. Likewise, the barrier thickness is given by Equation 2

$$t_{Barrier} = (Instantaneous\ Growth\ Rate)(Shutter\ Open\ Time) \quad (2)$$

and the well thickness is determined by the Equation 3.

$$t_{well} = \left(\left(\frac{III}{V}\right) - 1\right)(Instantaneous\ Growth\ Rate)(Shutter\ Open\ Time) \quad (3)$$

where t_{well} is the well thickness, $t_{barrier}$ is the barrier thickness, and (III/V) is the III/V ratio. It should be noted that SASL formation can only occur when the III/V ratio is greater than 1.

The compositions of the well and barrier layers possess far more factors, both in number and complexity, in their control. During the initial formation of the PM, the Al to Ga effective flux ratio ("effective" accounts for desorption) and lattice constant of the PM layer, in part, controlled by strain from the semiconductor will play a factor in the barrier composition as well as the rate of exchange of Ga and Al atoms between the PM layer and the above LC and droplet layers. For example, while the composition of the barrier was approximately fixed for all cases in Table 1, it was not equal to the set flux ratio (50%) even though Ga desorption at 725 °C is small (a few percent at most). Instead, the barrier composition was ~70% owing to 1) the exchange rate of Al/Ga and 2) the desire of the liquid crystalline PM to strain closer to the underlying AlN

substrate's lattice constant. All these factors will have a strong influence of the composition of the barrier, but are also each effected by the instantaneous composition and strain state of the barrier. The excess Al accumulated during the barrier will be the only factor in the composition of the well. This implies that the Al percentage in the barrier and well can be a function of time/distance and is best expressed with a constraint, not an equality. For example, Equation 4 applies to the balance of Al distributed between the well and barrier.

$$\frac{\text{Effective Flux of Al}}{\text{Effective Flux of Ga + Effective Flux of Al}} = \frac{1}{t_{period}} \int_0^{t_{Well}} Al_{Well}\%(x)dx + \int_0^{t_{Barrier}} Al_{Barrier}\%(x)dx \quad (4)$$

While Equation 4 establishes a constraint on the conservation of Al in the well and barrier, the determination of the expressions for the distance dependent well and barrier compositions, $Al_{Well}\%(x)$ and $Al_{Barrier}\%(x)$ are beyond the scope of such an experimental study. Thus, further modelling efforts are underway and will be published at a later date.

5.4 Conclusion

The cyclic nature of metal modulated epitaxy was applied to grow self-assembled superlattices without requiring growth interruptions, to adjust metal flux and substrate temperature between layers of the superlattice, preventing the buildup of contaminants at the interface of the superlattice layers. TEM, XRD and PL show excellent SASL quality. Fine control of the superlattice period and individual layer thickness was demonstrated via control of the metal dose and III/V ratio during the SASL structure growth. High coherency of the superlattice structure was achieved utilizing an instantaneous growth rate of 2.8 μm/hr and highly coherent SASL structures were demonstrated even with a thickness as high as ~910nm. Design parameters to customize the

layer thicknesses and compositions are presented but control over the average barrier composition, which in turn controls the average well composition, was substantially more complex. This technique shows promise for the growth of high quality, coherent superlattice structures, with tunability that would allow for applications that range from requiring thin individual layers for MQW structures to applications that require thick individual layers, such as DBRs with consistent repeatability over many periods.

CHAPTER 6. DISCOVERY OF A SIGNIFICANT CATYLITIC EFFECT FOR ScN GROWTH AND IMPROVED NUCLEATION OF CUBIC (111) ScN FILMS ON WURTZITE (0002) GAN

6.1 Intro

In recent years, ScN has gained interest as a novel transition metal nitride semiconductor due to its promising electronic, thermoelectric, and ferroelectric properties. ScN has an indirect bandgap of 0.9 eV and a direct bandgap of 2.2 eV and typically, undoped, demonstrates a resistivity in the range of 10^{-4} Ω-cm and a high carrier concentration of 10^{20}-10^{21} cm^{-3} due to the high affinity of Sc for scavenging oxygen.[208–212] The combination of a low electrical resistivity and a high Seebeck coefficient result in a promising thermoelectric power factor, giving the material an advantage in heat to power conversion applications. Additionally, when allowed with AlN strong ferroelectric properties have been demonstrated for switching and tuning applications.[129–131,140,146] Favorably for epitaxy, the (111) ScN and (002) GaN in plane lattice parameters are very close, resulting in minimal strain for growth of (111) ScN on (002) GaN or vice versa. This property has been utilized to create ScN buffer layers for the reduction of defect density in GaN epilayers.[209]

A commonly observed issue in ScN epitaxy on GaN is the formation of twinned domains during growth, resulting in the formation of a columnar film structure of triangular domains rotated 180° relative to each other. An example of this can be seen in Figure 6.1, which displays a plane-view scanning electron microscopy image of a ScN film from Acharya *et al.*[213] To guide the eye, red circles highlight a pair of twinned domain columns, with the domains rotated 180° relative to each other. This twinning results from the orientation of a (111) cubic film when grown upon a

(0002) wurtzite film. Each step of the (0002) GaN film with a height of c/2 (1/2 a unit cell) will have a 180° degree shift in atomic orientation. While this shift will have no overall effect on a hexagonal film, this atomic arrangement will define the nucleation of a (111) cubic film in heteroepitaxy. This will result in some regions of the ScN being oriented based on the "c" arrangement and other regions being oriented based on the "c/2" atomic arrangement. These initial orientations will define how the rest of the growth proceeds. Elimination of these twinned domains will significantly improve the heterointerface and surface roughness of ScN films. Additionally, the mobility of carriers within the ScN film would be improved by eliminating the significant number of grain boundaries that would lead to carrier scattering within the films.[148]

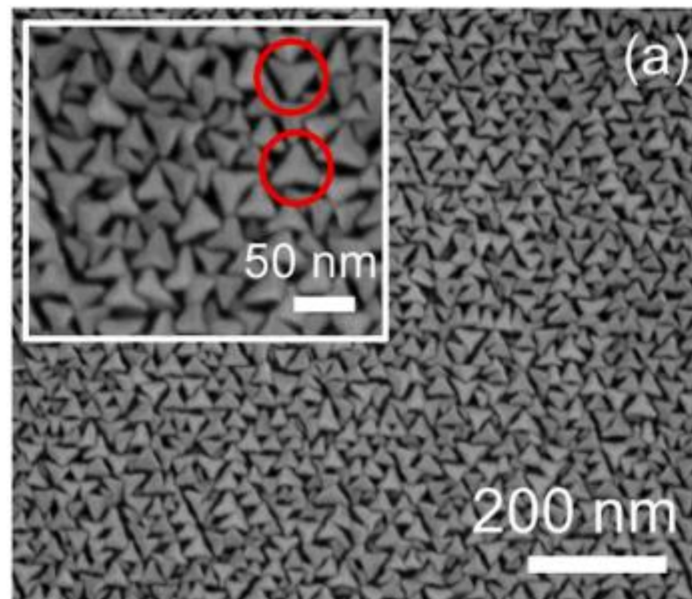

Figure 6.1: SEM surface image of a (111) ScN film grown on wurtzite GaN showing growth distinct rotated domains.

In this study, different nucleation methods are investigated for ScN growth on GaN to improve the interface and thin film phase purity along with the overall crystal quality. In traditional MBE, where ScN is initiated on a bare GaN surface, the initial layers of ScN demonstrate significant polycrystalline nature. This is demonstrated in reflection high energy electron diffraction (RHEED) patterns, where polycrystalline rings are prevalent due to random orientation of the ScN crystal on initiation. While the RHEED eventually improves to a single phase pattern, this takes a significant thickness, rendering any device that might rely on the GaN/ScN interface useless. Three initiation schemes are investigated to improve the GaN/ScN interface. In addition to 1) the direct ScN initiation on GaN, another scheme is investigated 2) in which a short dose of Sc metal deposition is employed before the ScN growth begins and 3) adding a layer of crystalline Sc deposited at low temperature and nitridated while heating to the ScN growth temperature. Both metal initiation schemes showed significant improvement in the RHEED characteristics, with a significant reduction, or total elimination, of the time in which the RHEED shows polycrystalline characteristics. Finally, both significant differences and similarities to the chemistry and kinetic behaviors of ScN versus other traditional III-Nitride binary compounds were observed. Such novel nucleation methods show promise for improving the phase purity and interface quality for ScN/GaN heterointerface.

6.2 Experimental Details

All films in this study were grown in a Riber 32 MBE reactor using the MME technique, the details of which can be found elsewhere.[142,143,153] All samples were grown on 1×1 cm^2 hydride vapor phase epitaxy (HVPE) iron doped semi-insulating GaN on sapphire templates. The substrates were single-side polished and $2\,\mu$m of tantalum was sputtered on the backside to facilitate uniform heat absorption during growth. Prior to growth the substrates were cleaned using

a 3:1 solution of H_2SO_4:H_2O_2. This clean was followed by a rinse with de-ionized (DI) water and a brief dip in dilute HF to reduce surface oxides, after which the sample was again rinsed with DI water and dried with N_2. After the chemical cleaning procedure, the samples were loaded into an introductory vacuum chamber with a base pressure of $\sim 1 \times 10^{-9}$ Torr in which they were outgassed at 200 °C for 20 minutes. Prior to growth, the samples were further outgassed at 675 °C, as measured via thermocouple, in the growth chamber which has a base pressure of $\sim 5 \times 10^{-11}$ Torr. Following the outgas, the samples were further cleaned using three cycles of gallium adsorption and desorption to further remove oxygen from the surface.[142]

During growth, aluminum and gallium fluxes were provided by conventional effusion cells and the scandium flux was provided via a high-temperature MBE Komponenten effusion cell. The ScN films were grown at a III/V ratio of 1.3 and a shuttering scheme of 21 s open and 11 s closed per cycle. The growth temperature and growth rate vary from sample to sample and are detailed in the discussion of each. An AlN film is grown standalone to obtain growth rate of AlN for comparison to ScN.

In situ surface monitoring was performed using Reflection High Energy Electron Diffraction (RHEED) to calibrate III/V ratio and metal doses, and postgrowth XRD analysis was performed with a Philips X'pert Pro MRD using a Cu Kα1 anode.[58,142] AFM measurements were performed via a Bruker Icon AFM in tapping mode. Transmission electron microscopy images were obtained using an F30 FEI Tecnai. Thickness measurements were performed via profilometry and growth rate was determined using ex-situ thickness measurements in combination for growth time and were adjusted for the active duty cycle of growth. The active duty cycle of the growth was taken to be the ratio of active growth time (shutter open time x III/V ratio) to total cycle time (shutter open time + shutter closed time). Thus, reported growth rates represent an active growth

rate as opposed to a global average growth rate which would simply be the film thickness grown over the total growth time to account for the differences in global average growth rate resulting from adjustments in shuttering and III/V ratios.

6.3 Results and discussion

6.3.1 Initiation Schemes for ScN Epitaxy

In order to change the conditions in the initial stage of growth, three different ScN initiation schemes were tested. The first was a control sample with no special initiation steps. In this sample the nitrogen plasma shutter was opened, exposing the GaN substrate to nitrogen, and then the Sc shutter was opened and growth was initiated. This will be referred to from here on as "standard". A second sample used a scheme attempting to increase the mobility of surface Sc atoms. In this sample, the Sc shutter was opened for 5s at growth flux before the nitrogen shutter was opened. Following the introduction of nitrogen, the growth was allowed to proceed as normal. This second scheme will be referred to as "Sc pulse". The third initiation scheme was intended to alter the initial surface during growth. In this case, 10 nm of Sc metal was deposited at 100 ^{o}C and the nitrogen plasma was exposed to this metal layer while the substrate was heated up to the growth temperature of 650 ^{o}C. As Sc metal has a hexagonal crystal structure like GaN, the metal film is presumed to be well ordered on the GaN template and will be shown via RHEED analysis to be likely the case. Nitridation of this metal film could result in a better ordered ScN film for growth to proceed on. This third scheme will be referred to as "Sc buffer".

While traditionally in epitaxy, XRD measurements would be a core part of structural characterization, such measurements are less effective in the case of (111) ScN on (0002) GaN. This issue is illustrated in Figure 6.2, showing a representative XRD 2θ-ω curve for a (111) ScN

film grown on (0002) GaN. Due to the interplanar spacing of (111) ScN and (0002) GaN, the two planes have a nearly identical peak position in the measurement. Due to the proximity of the two peaks, it is impossible to isolate the (111) ScN peak and take a rocking curve measurement. Traditionally, XRD rocking curves are used to assess crystal quality of a film, but in this case other, far more time consuming, methods will have to be utilized.

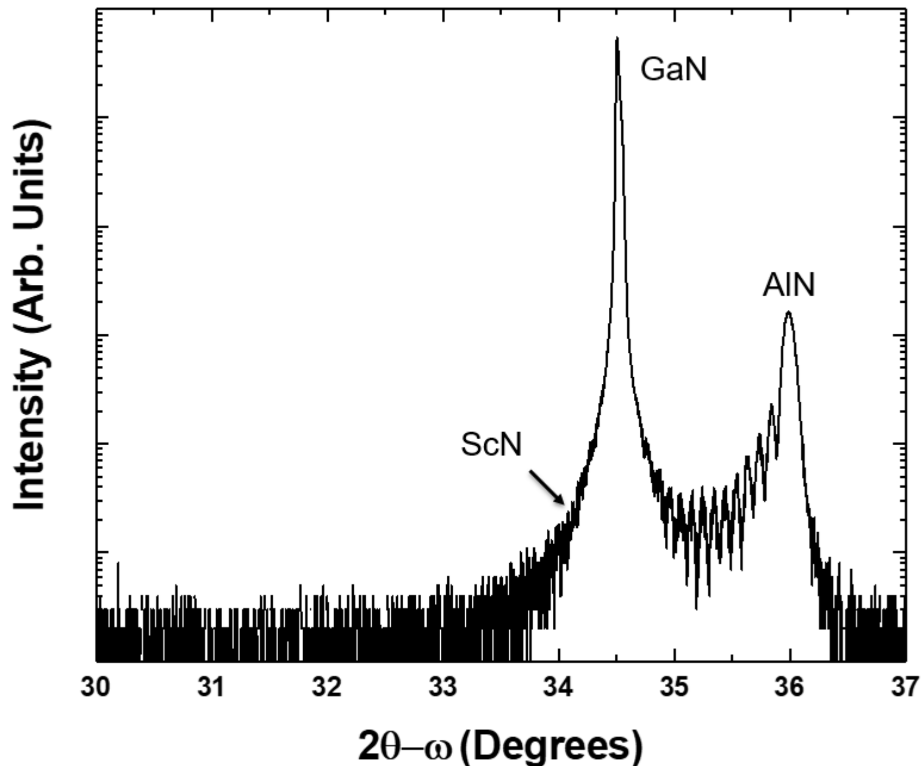

Figure 6.2: XRD 2θ-ω scan of a 111 ScN film grown on wurtzite GaN. Due to the lattice constants of the ScN, the peak is located inside the GaN peak and cannot be isolated.

For this study, three characterization methods have been selected to compare the different initiation schemes. To assess the surface of the (111) ScN films, RHEED and AFM are utilized. RHEED will give in-situ qualitative analysis of the film surfaces, while AFM will allow for ex-situ study of surface features and roughness. For structural and interface characterization, TEM was selected. The combination of these three techniques will allow for an accurate assessment of

the effect of the initiation schemes on the ScN films even without the traditional XRD measurements.

6.3.2 Surface Progression of (111) ScN Films

Figure 6.3 displays the RHEED progression of the three ScN films utilizing different initiation schemes. The leftmost image shows a representative image of a bare GaN surface. Proceeding to the right, a RHEED image from 1 minute and then 4 minutes into the growth is shown for each of the three samples. Finally, the rightmost series of images is taken at the end of growth for each of the three ~200 nm thick ScN films. While RHEED images are largely a qualitative analysis method, several useful inferences can be made by watching the progression of the RHEED patterns over time. Looking first at the images taken 1 minute into the growth, clear differences can be observed. The standard film shows a heavily polycrystalline nature. The pattern shows significant circular spots, characteristic of a polycrystalline film. It is possible in this case that due to strain between the wurtzite GaN layer and the ScN layer (which wants to take on a cubic structure) in the initial stages of growth under these conditions a portion of the ScN has a wurtize structure, while the rest is cubic, resulting in the observed polycrystalline pattern. In contrast, the Sc pulse and Sc buffer films show a much different RHEED pattern. Both films show a similar pattern to each other, representing a predominantly cubic film. However, the double spots along the ½ order streak present for both films in the lines above and below the central line are characteristic of a twinned cubic film, implying that in the initial stages of growth these initiation methods still result in twinned domain growth.

Four minutes into the ScN growth, the standard and Sc buffer RHEED patterns have evolved as the surfaces change. The Sc pulse film, however, shows little change relative to the

evolution seen in the standard and Sc buffer films. Going from the 1 minute to 4 minutes patterns for the standard film, all evidence of a polycrystalline nature is lost. The pattern is spotty and no longer shows any of the ring nature observed earlier in the growth, suggesting that the film has become fully cubic at this stage. However, the film now shows twinned spots, similar to what was observed at 1 minute for the Sc pulse and Sc buffer films, implying a twinned domain film at this stage. For the Sc buffer film, the twinned spots are still present, but the surface has begun to change. Instead of the individual spots observed at 1 minute, the spots have begun to widen into streaks. This suggests that the domains have begun to coalesce together, and one domain orientation is beginning to dominate.

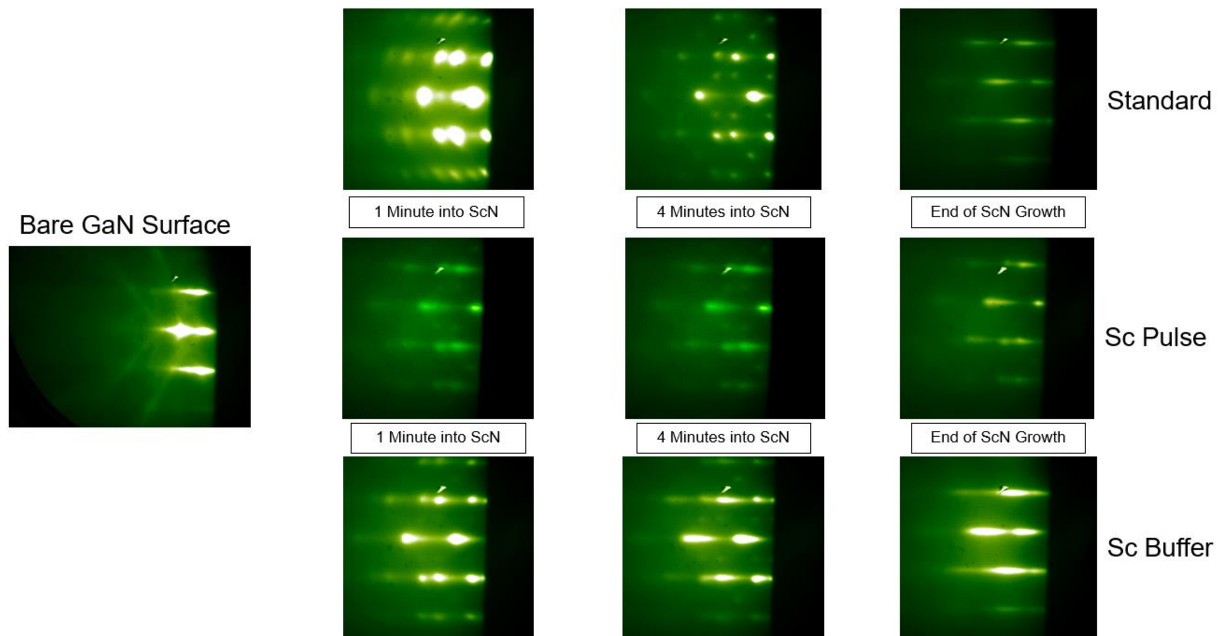

Figure 6.3: RHEED progression during growth for the three different initiation methods.

Finally, at the end of growth the RHEED pattern representative of the final film surface is obtained. At this stage the standard film has taken on a streaky pattern, with each line showing

broad streaks as opposed to the spots previously observed for the film. This suggests that a single domain orientation has become predominant within the film. The Sc buffer film shows a very similar pattern as the coalescence of the domains has continued and a predominant domain orientation has also taken over for this film. Surprisingly, the Sc pulse film has shown little change over the course of the growth and remains dim, possibly suggesting surface accumulated Sc remains on the surface even at the end of film growth. The RHEED patterns for the Sc pulsed film taken 1 minute into the growth and at the end of the growth are extremely similar, suggesting that the film initiated with twinned domain growth and did not evolve over the course of the growth.

Post growth, AFM scans are obtained to assess the final surfaces of the films and are shown in Figure 6.4. The standard film shows a rough surface with an RMS roughness of 11.8 nm. Additionally, features similar to previously observed triangular domains can be observed, implying that the growth proceeded in a largely columnar fashion and resulting in a large step height between each column, generating a rough surface. The Sc pulse film shows a similar surface to the standard film, with a high density of triangular domains. However, this film also appears to show macro-scale droplet like features, with 1-2 µm wide humps with higher peaks than the surrounding areas. At a temperature of 650 ^{o}C, Sc will have a high surface tension based on ex-situ observations of Sc metal films balling up on the surface at high temperature. This will result on Sc metal accumulating on the surface as droplets, rather than planar films. It is likely that in the case of the Sc pulse film, during the 5 s Sc pulse employed before the growth starts it is likely that the metal accumulated as droplets. These droplets were nitrided and growth proceeded on top of them. This resulted in a surface whose roughness was dominated by these droplets, resulting in an increase in the RMS roughness over the standard sample to 13 nm. In contrast, the Sc buffer sample showed a significant improvement in RMS roughness to 5.0 nm. It can be seen in the AFM scan for the Sc

buffer sample that instead of a high density of triangular columns, for this initiation method the domains have somewhat coalesced together. While it appears that the coalescence is not complete, with some gaps and distinct triangular features still being present, this merging of domains resulted in a significant improvement in surface morphology. Growing a thicker film with the Sc buffer initiation method could potentially result in total coalescence of domains and a smooth planar film.

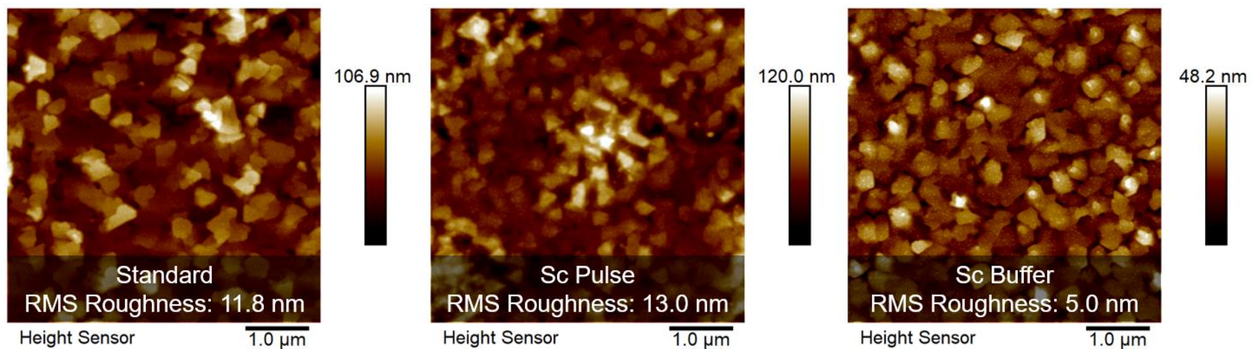

Figure 6.4: AFM scans of the end of growth surfaces for the ScN films grown using different initiation schemes.

Further effect of these initiation schemes can be observed in TEM measurements. Figure 6.5 shows cross sectional TEM images for the standard and Sc buffer samples. Two significant differences can be seen in the two structures. The first is the appearance of patterning within the film due to beam penetration through twinned, rotated domains especially prominent in the standard growth case. In the standard sample this effect is observable from the ScN/GaN interface all the way to the sample surface, with only minimal regions not showing this effect. This effect is significantly reduced in the Sc buffer sample. In the Sc buffer sample, some patterning due to twinned domains is present near the ScN/GaN interface, but most of it disappears within the first 20-30 nm of ScN, resulting in a significantly more homogeneous film compared to the standard sample. In the Sc buffer sample image in Figure 6.5, only one region of patterning can be observed extending to the sample surface in the measured region, a significant improvement over the

standard sample which has this effect reaching the surface over most of the measured region. The second significant difference lies in the surface and interface roughness for the two different films. In the previously discussed AFM images, it was already observed that the Sc buffer sample showed an RMS roughness of less than half that of the standard sample and this difference is even more pronounced in the TEM images. On this TEM length scale the Sc buffer sample shows a nearly planar surface, whereas significant variations in surface height are observed for the standard sample. Interestingly, the variation in surface height for the standard sample corresponds to similar ScN/GaN interface roughening directly below each surface feature. In fact, it appears that some form of alloying effect occurs at the ScN/GaN interface, likely due to some diffusion of Sc into the GaN film at ~650 ^{o}C, forming a $Sc_xGa_{1-x}N$ alloy. On the other hand, this effect is completely absent in the Sc buffer sample. Possibly, due to the low temperature at which the Sc was deposited pre nitridation (100 ^{o}C) no Sc was able to diffuse into the GaN film. Further, nitridation locked the Sc in place and prevented further diffusion of atoms into the GaN film and seems to have also prevented the deposited Sc from balling up as in the Sc pulsed case.

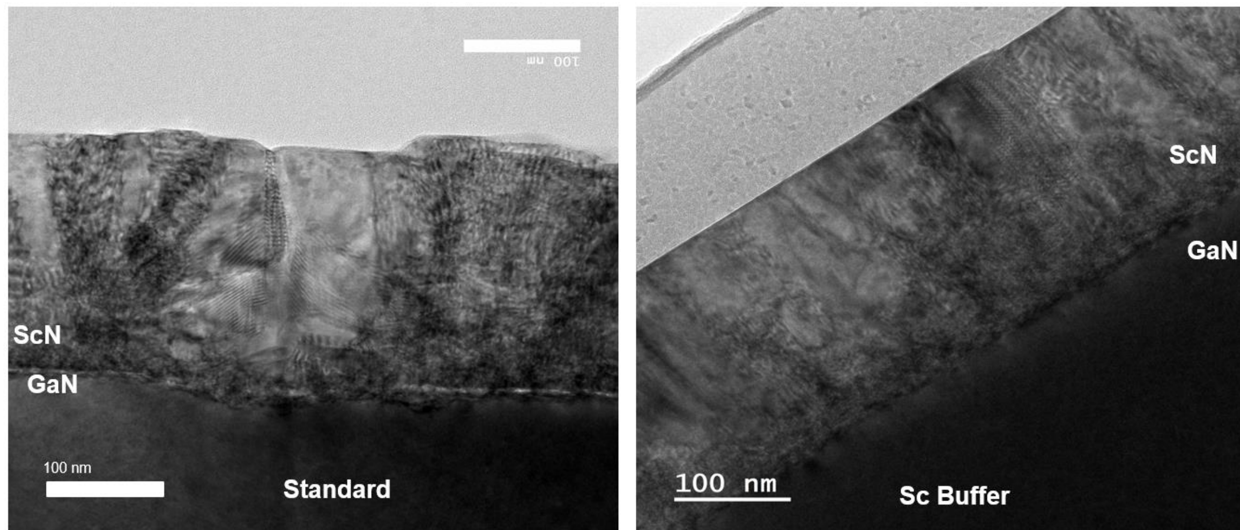

Figure 6.5: TEM images highlighting the differences between the standard initiation methods and the Sc Buffer initiation.

6.3.3 A Strong Catalytic Effect in ScN Growth

A standard post growth characterization step is profilometry to ensure that target thicknesses were met and that a systems growth rates are consistent. Unlike traditional MBE where a global average growth rate (the film thickness grown over the total growth time) is easily determined, the MME process has growth occurring over only a portion of the total cycle. Growth occurs during the metal shutter open cycle (both metal shutters simultaneously opened) and after the shutters are closed during the part of the cycle where the accumulated metals are consumed. However, growth then momentarily stops before the beginning of the next cycle. Thus, to report an accurate growth rate, a simple global average growth rate is inappropriate. The instantaneous growth rate (valid for the portions of the cycle where growth is occurring) was determined using ex-situ thickness measurements in combination with growth time and were adjusted for the active duty cycle of growth. The active duty cycle of the growth was taken to be the ratio of time growth is taking place (shutter open time x III/V ratio) to total cycle time (shutter open time + shutter

closed time). By weighting the shutter open time by the III/V ratio, the growth occurring while the metal shutters are closed, but accumulated metal remains, is accounted for, while the time no metal is present on the surface and no growth is occurring is removed from consideration. This method yields a reliable in-situ method of monitoring growth rate and making on the spot adjustments during growth to ensure accurate conditions. For traditional (Al, In, or Ga based) III-Nitride growth, variations in growth rate are minor and are normally due solely due to the differences in the c-lattice constants for the various alloys. Thickness measurements for ScN yielded surprising results, however. In the growth reactor used in this study, the growth rate for AlN is consistent at 680 nm/hr. On the other hand, the standard ScN sample, with growth initiation and conditions most similar to what would be used for traditional III-Nitride alloys, yielded a growth rate of 2.21 μm/hr, a growth rate over 3x that of AlN.

In order to investigate this growth rate increase further, an additional set of ScN films were growth. In this case, two more ScN films were grown using the standard initiation method, but at substrate temperatures of 550 and 600 ^{o}C. Post growth, the thickness of these films was measured via profilometry and the growth rate was calculated. These growth rates, as well as that of the standard ScN sample grown at 650 ^{o}C and an AlN sample grown under standard conditions for the system, are shown in Table 1. Surprisingly, a significant temperature dependence of the ScN growth rate is observed. In more traditional, Al, In, and/or Ga based, III-Nitride epitaxy, little growth rate variance is seen with temperature. Above the desorption regime for a metal the growth rate will decrease due to a loss of metal species on the surface, but growth below the desorption regime where all these measurements were performed generally sees little variation in growth rate.

Table 6.1: Growth rates for ScN and AlN at various substrate temperatures.

Material	Growth Substrate Temp. (°C)	Growth Rate (μm/hr)
ScN	650	2.21
ScN	600	1.92
ScN	550	1.75
AlN	700	0.68

The best explanation for such a large change in the growth rate for ScN vs other binaries would be a significant catalytic effect when using Sc in growth. In plasma assisted MBE (PAMBE) of III-Nitrides, multiple nitrogen species are supplied by the plasma, based on gas flow and excitation power conditions. In the minority will be excited atomic nitrogen species. These species impinge on the substrate surface with no further energy being required to produce reactive nitrogen and can quickly bond with a metal atom. However, the majority of the nitrogen supplied by the plasma is in the form of excited molecular nitrogen. Excited molecular nitrogen will require additional thermal and catalytic energy to crack and produce reactive nitrogen before it can contribute to film growth.[36] More traditional metals like Al, In, and Ga will have some level of catalysis for the production of reactive nitrogen but have little variation between the three metals.

In general, the growth rate differences between AlN, InN, and GaN will be due to the differences in the c-axis lattice constants of the materials and not any difference in catalysis. No such lattice constant difference can explain the difference in growth rate between these more traditional binaries and ScN.

ScN is a cubic material belonging to the Fm3m space group with a lattice constant of 4.52 Å.[214] When grown on GaN, as it was for this study, ScN has a 111 orientation, with an interplanar spacing of about 2.59 Å, extremely close to that of GaN. Therefore, if no catalytic effect was in play, ScN should grow at a similar rate as GaN. As a result, the best conclusion by far is the existence of a significantly higher catalytic effect for growth with Sc. This effect will cause complications in selection of growth conditions for the growth of ScN or ScN containing ternary alloys like ScAlN. This temperature dependence will cause changes in the metal fluxes required to hit a given III/V ratio for both binary and ternary alloys and effect the fluxes needed to achieve a desired Al/Sc ratio for ScAlN. In general, significant caution must be used in selecting growth conditions for any Sc bearing III-Nitride alloy.

6.4 Conclusion

ScN possesses many challenges for growth atop GaN that are unique among III-Nitride binary semiconductors. Due to its cubic structure and 111 orientation when grown atop a hexagonal substrate, twinned domains form as early as the initial film nucleation. While this effect can be partially overcome with proper initiation conditions and thick film growth, the presence of these twinned domains will cause significant disorder in the film and significant surface roughness. Further complicating the optimization of ScN epitaxy is a significant, temperature dependent, catalytic effect increasing the growth rate of ScN and causing it to grow over 3 times faster than

AlN in some conditions. Novel initiation methods can result in the improvement of 111 ScN films grown on GaN. Depositing a Sc metal buffer layer and low temperatures and nitriding the film while heating to the ScN growth temperature results in a significant reduction in the formation of twinned domains and a large improvement in surface roughness for the ScN film and the interface roughness for the ScN/GaN interface. Further, using this low temperature buffer prevents Sc diffusion into the GaN film that results in alloying and interface degradation.

CHAPTER 7. OVERCOMING METAL RICH SURFACE CHEMISTRY LIMITATIONS OF SCALN FOR HIGH ELECTRICAL PERFORMANCE HETEROSTRUCTURES

7.1 Introduction

ScAlN alloys have been a topic of great interest in recent years due to their high spontaneous and piezoelectric polarization and their ferroelectric properties, in addition to the fact that ScAlN has been reported to be lattice matched to GaN at a composition of ~18-20% Sc.[126–131] Due to the immense spontaneous polarization coefficients of the alloy, even in the case of being lattice matched to GaN where piezoelectric polarization will have no effect on sheet charge, 2D electron gas (2DEG) densities as high as ~$6x10^{13}$ cm^{-2} have been predicted in literature and approached in experiment.[127,132] Thanks to these favorable properties, a number of $Sc_xAl_{1-x}N$/GaN HEMT structures have been demonstrated, achieving sheet resistances as low as 167 Ω/□ and mobilities as high as 1556 cm^2/vs.[132–136] Since ScAlN is primarily grown nitrogen rich and thus tends to roughen, most of the high electron mobility structures utilize an AlN and/or AlGaN interlayer that provide smooth interfaces while, in the case of AlN, minimizing random alloy scattering. A number of growth issues have plagued the alloy that must be overcome to achieve the theoretical potential of the system. Previously, ScAlN was deposited via radio frequency (RF) sputtering, which often yielded material that was polycrystalline and/or contained a high defect density, degrading device performance.[137–141] In recent years, nitrogen-rich MBE of single phase ScAlN has been demonstrated with improved crystal quality, allowing for HEMT properties to be advanced.[135,136] However, a challenge still remains in MBE of ScAlN in the form of metal rich growth, which is the preferred chemistry for MBE and can provide enhanced atom surface

diffusion. In traditional III-Nitride MBE, metal rich chemistry has led to an improvement of crystal quality, surface roughness, and interface roughness.[24,142,144,145,215] Due to multiple intermetallic Al_xSc_y phases being thermodynamically stable under metal rich conditions, thus far, attempts to grow ScAlN under these metal rich conditions have led to the inclusion of unintended metal and even rock salt phases.[132,135,146] Adding an additional complication, the phase transition of ScAlN from wurtzite towards rock salt has been reported to occur around 40% Sc. Metal rich ScAlN has been investigated using Ga as a pseudo-surfactant, but since Ga is soluble in ScAlN at all achievable growth conditions, Ga will incorporate into the films creating a ScAlGaN alloy.[147] Thus, the achievement of phase pure ScAlN has been elusive for the generally preferred metal rich growth condition.

A transition to metal rich growth of single phase, high quality ScAlN films will lead to a number of advantages and improvements in the performance of devices. A significant, noteworthy improvement would be the reduction of interface roughness induced scattering to improve the mobility of the 2 dimensional electron gas (2DEG) generated at the interface of a ScAlN/GaN interface .[148–151] The use of ScAlN directly in contact with GaN could forego the screening of the beneficially large ScAlN polarization by the less polar AlN or AlGaN. It is worth noting that the work of Frei *et al.* achieved close to the theoretical value of 2DEG density by not using an interlayer.[132] However, thus far no report of successful metal rich, phase pure growth has been reported for this alloy system.

Of the predominant III-Nitride epitaxy techniques, only molecular beam epitaxy (MBE) seems to have the potential to grow ScAlN under metal rich conditions. Metal organic vapor phase epitaxy (MOVPE) typically uses heavily nitrogen rich growth for III-Nitride epitaxy, and faces the added issue of a lack of suitable precursors for Sc. Due to the poor volatility of Sc precursors, thus

far MOVPE-grown ScAlN films have been limited to a maximum Sc content of ~30% and to even achieve such a concentration custom modifications to the chamber were needed and growth is limited by rates far slower than what can be achieved for other III-Nitride alloys.[152] Utilizing standard or high temperature effusion cells, MBE reactors are capable of producing the Sc fluxes required to grow under metal rich conditions. However, previous MBE studies of metal rich growth of ScAlN have demonstrated the inclusion of metallic or rock salt phases. Hardy *et al.* utilized traditional MBE of $Sc_{0.18}Al_{0.82}N$ over a range of III/V ratios, but observed that as the III/V ratio increased and approached stoichiometry and transitioned into metal rich, phase separation was observed in X-Ray Diffraction including intermetallic inclusions and what was theorized as rock salt phases.[135] Frei *et al.* utilized an alternating Al then Sc cyclic pulsed metal technique in MBE, but observed much the same.[132] However, neither study implemented a scheme to control the buildup of surface metal, likely enhancing phase separation as has been reported in other ternary III-Nitride materials.[153]

Metal modulated epitaxy is a pulsed metal deposition MBE technique that has demonstrated surface engineering to control and eliminate phase separation in heavily metal rich growth of III-Nitride ternaries. MME has demonstrated single phase growth of InGaN, AlInN, and AlGaN utilizing III/V ratios well over stoichiometry, as well as the engineering of surface segregation to growth self-assembled superlattice structures.[24,58,153,181,215] This is achieved via precise control of metal adlayer buildup, as it has been demonstrated that excess metal buildup can be a severe catalyst for phase separation in III-nitride ternary growth. It is likely that uncontrolled metal buildup in previous attempts at metal rich growth of ScAlN has been a driving cause of phase separation, and that the surface engineering enabled by MME can overcome this challenge and allow for the utilization of the desirable properties of ScAlN films grown under metal rich

conditions. Key to MME's prior success is operation below the desorption temperatures of the metals making the surface a function of the incoming flux and not dependent on a position dependent desorbing flux resulting from even small temperature non-uniformities.

In this study we demonstrate, for the first time, metal rich growth of $Sc_{0.2}Al_{0.8}N$ with phase purity via MME. Variations in growth conditions, including substrate temperature and III/V ratio, were studied and the quality of the films was assessed via XRD and AFM. $Sc_{0.2}Al_{0.8}N$ XRD (0002) FWHM values as low as 225 arcsec were demonstrated, with AFM RMS roughness as low as 0.68 nm. The best growth conditions were applied to grow a HEMT structure consisting of 20 nm of $Sc_{0.2}Al_{0.8}N$ atop 200 nm of UID GaN grown on a semi insulating GaN:Fe template. Hall measurements of this structure revealed a sheet resistance (R_s) of 152 Ω/□, a mobility of 700 cm^2/Vs, and a sheet charge of 5.9×10^{13} cm^{-2} close to the theoretical maximum. Thus, metal rich growth of $Sc_{0.2}Al_{0.8}N$ demonstrates significant potential for the advancement of HEMTs.

7.2 Experimental Details

All films in this study were grown in a Riber 32 MBE reactor using the MME technique, the details of which can be found elsewhere.[142,153,215] All samples were grown on 1×1 cm^2 hydride vapor phase epitaxy (HVPE) unintentionally doped GaN on sapphire templates, except for the HEMT structure which was grown on a HVPE grown semi-insulating GaN:Fe template. The substrates were single-side polished and 2 μm of tantalum was sputtered on the backside to facilitate uniform heat absorption during growth. Prior to growth the substrates were cleaned using a 3:1 solution of H_2SO_4:H_2O_2. This clean was followed by a rinse with de-ionized (DI) water and a brief dip in dilute HF to reduce surface oxides, after which the sample was again rinsed with DI

water and dried with N_2. After the chemical cleaning procedure, the samples were loaded into an introductory vacuum chamber with a base pressure of $\sim 1 \times 10^{-9}$ Torr in which they were outgassed at 200 °C for 20 minutes. Prior to growth, the samples were further outgassed at 675 °C, as measured via thermocouple, in the growth chamber which has a base pressure of $\sim 5 \times 10^{-11}$ Torr. Following the outgas, the samples were further cleaned using three cycles of gallium adsorption and desorption to further remove oxygen from the surface.[142]

During growth, aluminum and gallium fluxes were provided by conventional effusion cells and the scandium flux was provided via a high-temperature MBE Komponenten effusion cell. An initial series of 100 nm thick ScAlN films were grown varying growth temperature and III/V ratio. Prior to the ScAlN layers, a 100 nm thick GaN layer was grown to bury contamination and provide a smooth regrowth surface. The best conditions from the first series were applied to grow a HEMT structure consisting of 20 nm $Sc_{0.2}Al_{0.8}N$ layer atop 200 nm UID GaN grown on a semi insulating GaN:Fe template. During ScAlN growth, the Al and Sc sources were shuttered synchronously, while the nitrogen plasma is exposed to the surface at all times, allowing for all excess metal to be consumed between cycles unless stated otherwise. Another set of samples was grown to assess the growth rates of the binary AlN and ScN alloys. These samples were grown at a III/V ratio of 1.3, with a shuttering scheme of 21s open and 11s closed per cycle. The substrate temperature and growth rate of these samples are listed below. Nitrogen was provided by a Veeco UNI-Bulb radio frequency (RF) plasma source with an RF power of 350 W and a gas flow of 1.25 SCCM, yielding a growth rate of 710 nm/hr for GaN, with the growth rate of other alloys being listed in later discussion. This slower growth rate than previously used for GaN was limited by the practically achievable Al flux without causing damage to the effusion cell.[154] Throughout this paper, we report growth rates obtained by excessively metal rich growth chemistry, often exceeding 60% greater

than the stoichiometric chemistry. To facilitate comparisons with other techniques and various III/V ratios, we report the instantaneous growth rates normalized to stoichiometry as defined in our prior work.[153] For linguistic simplicity, we refer to this as simply the growth rate.

In situ surface monitoring was performed using Reflection High Energy Electron Diffraction (RHEED) to calibrate III/V ratio and metal doses, and postgrowth XRD analysis was performed with a Philips X'pert Pro MRD using a Cu Kα1 anode.[58,142] AFM measurements were performed via a Bruker Icon AFM in tapping mode. Energy-dispersive X-ray spectroscopy (EDX) was performed via transmission electron microscopy (TEM) using an F30 FEI Tecnai. Unlike traditional MBE where a global average growth rate (the film thickness grown over the total growth time) is easily determined, the MME process has growth occurring over only a portion of the total cycle. Growth occurs during the metal shutter open cycle (both metal shutters simultaneously opened) and after the shutters are closed during the part of the cycle where the accumulated metals are consumed. However, growth then momentarily stops before the beginning of the next cycle. Thus to report an accurate growth rate, a simple global average growth rate is inappropriate. Thickness measurements were performed via profilometry, and the instantaneous growth rate (valid for the portions of the cycle where growth is occurring) was determined using ex-situ thickness measurements in combination with growth time and were adjusted for the active duty cycle of growth. The active duty cycle of the growth was taken to be the ratio of time growth is taking place (shutter open time x III/V ratio) to total cycle time (shutter open time + shutter closed time). By weighting the shutter open time by the III/V ratio, the growth occurring while the metal shutters are closed, but accumulated metal remains, is accounted for, while the time no metal is present on the surface and no growth is occurring is removed from consideration. Hall measurements were performed at room temperature with a LakeShore M91 fast Hall system with

the post excitation blanking time selected to eliminate potential self-heating effects. ScAlN etching was done with a Plasma Therm ICP and standard Ti/Al/Ni/Au (20/200/40/50 nm) contacts were deposited via e-beam evaporation, followed by a 1 minute anneal at 950 ^{o}C under nitrogen atmosphere.

7.3 Results and Discussion

7.3.1 Growth Temperature Optimization of ScAlN

Initially, a series of ScAlN films were grown under constant conditions, with a shuttering scheme of 2 s open/2 s closed and a III/V ratio of 1.6, varying only the growth substrate temperature between 600 and 700 ^{o}C in steps of 50 ^{o}C. This quick shuttering scheme was selected to minimize the buildup of a metal adlayer with each cycle to ~1 monolayer, as done previously in MME growth of InGaN and AlInN, where it was found that limiting the adlayer accumulation to about 1-1.2 monolayers prevented vertical segregation and improved film quality.[24,58,215] For this work, ~0.4 to 1.2 nm of ScAlN is grown while the metal shutters are open for 2 to 6 seconds and an additional 0.2 nm grown from the ~1.05 monolayers of excess metal accumulated and consumed during the metal shutter closed portion of the cycle. Since all temperatures used here are well below the desorption temperatures of Al and Sc, the Al/Sc ratio is strictly determined by the incoming flux and is constant to within ~1% (flux repeatability) in this series of samples. It should be assumed that, unless specifically stated otherwise, all surface metal is consumed during the 2 s shutter closed time each cycle. Figure 7.1 shows the XRD 2θ-ω scans of the three samples. The peak at ~36.1 corresponds to the (0002) plane of wurtzite ScAlN. The compositions of the films were determined via RBS to be 23% ± 2%, while the composition according to EDX is 19%

± 1%. The XRD reciprocal space map (RSM) measurements show an a lattice constant of ~3.185 Å, nearly lattice matched to GaN, suggesting a composition of about 18% Sc, though there is some uncertainty in the literature on the exact lattice constants for a given composition. Notably, because the total metal dose was limited by short shuttering times, growth at 650 and 700 °C display a single ScAlN peak, with no evidence of phase separation or the inclusion of metallic phases as has been previously observed for metal rich ScAlN growth.[132,135] This changes, however, at lower growth temperatures, as it can be seen in the film grown at 600 that an additional peak shows up at ~38 degrees. This is likely corresponding to the inclusion of Al_3Sc similar to previous observations for metal rich growth of ScAlN.

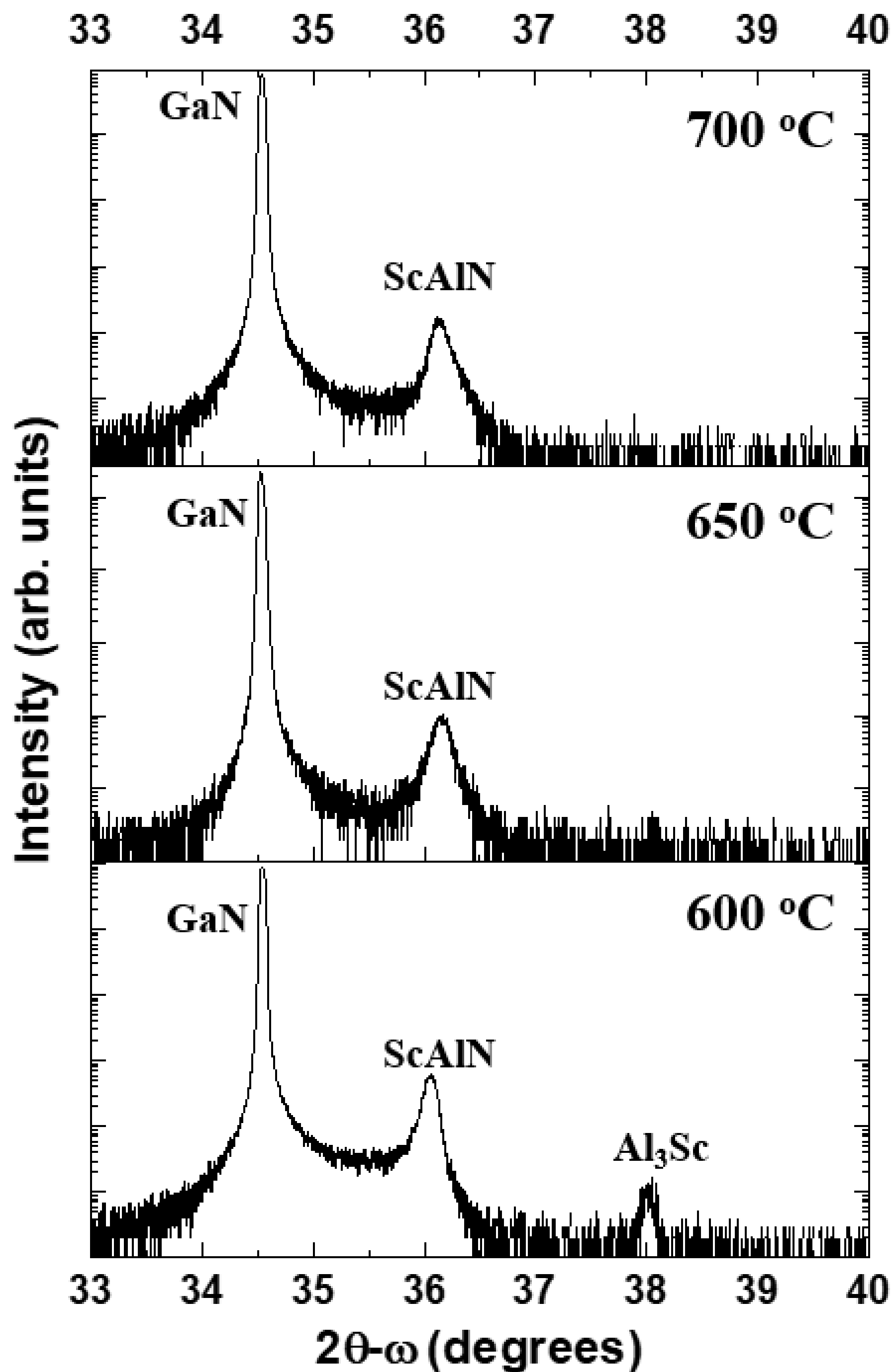

Figure 7.1: XRD 2θ-ω curves of ScAlN grown under metal rich conditions at various growth temperatures. Phase pure growth is observed for growth at and above 650 °C.

Table 7.1: XRD rocking curve FWHM values for the ScAlN films grown under metal rich conditions at various growth temperatures.

Grow Temperature ^{o}C	XRD (0002) RC FWHM
700	492
650	334
600	225

Two phenomena must be explained in these results. The first being the achievement of single phase ScAlN epitaxy under metal rich conditions and the second being the transition from phase pure growth at high substrate temperatures, to multi-phase at lower temperatures. Previous attempts at metal rich growth of ScAlN have failed to demonstrate phase pure material, but have also utilized growth schemes that lack the surface kinetics control innate to MME. For example, Hardy *et al*. utilized traditional MBE and likely allowed for the uncontrolled buildup of metal on the surface of the ScAlN film during growth, resulting in the formation of additional metallic or rock-salt phases.[135] Frei *et al.* utilized a pulsed growth method in MBE, but only varied which metal flux was active at a given time and likely also allowed for the uncontrolled buildup of surface metal.[132] Surface accumulation of metal is a critical parameter in MBE of ternary alloys, especially one as unique as ScAlN. Previous work on InGaN and AlInN have shown that excess buildup of metal result in significant film degradation and phase separation.[58,204] AlGaN has demonstrated surface segregation, resulting in the formation of self-assembled superlattice structures due to the spontaneous exchange of cations between metal adlayers.[153] All of these factors will likely play a

role in the growth of ScAlN and have been mitigated here by shutter open times that are coordinated with the growth rates. By utilizing a controlled shutter scheme in MME, we are able to limit the adlayer buildup to a single monolayer, as determined via RHEED analysis. Controlling accumulation to a single monolayer will do three things for the growth: first, adatom mobility will be increased by replacing strong semiconductor bonds with weak metal bonds, allowing for the frequently noted benefits of metal rich growth; second, cation exchange between adlayers will be eliminated, mitigating a potential driver for vertical phase separation; and third, allows for a surface strain state of the metallic adlayer that will reduce the chance of phase separation. This last point results due to the closest stable intermetallic phase to the flux ratio of 80/20 Al/Sc being Al_3Sc with a lattice constant of 4.11 Å.[214] Thus, the first metal adlayer accumulated during growth is pseudomorphically strained to the underlying film and has a lattice constant similar to GaN, 3.185 angstroms, making it difficult to form standalone Al_3Sc phases. The same strain driven preference for the semiconductor phase over the metal phase applies to cubic ScAlN phases, as both the crystal structure and lattice constants would be significantly different. This strain benefit diminishes when the second adlayer begins to form and is gone completely when droplets of metal form. Caution is warranted in the use of the widely accepted term "droplet" in that Sc, Al and multiple intermetallic phases can be solid at these growth temperatures. Thus, this controlled surface chemistry (i.e., one or less adlayers of metal) successfully demonstrated phase pure growth of ScAlN under metal rich conditions with high crystal quality, as is shown via the XRD figures of merit listed in Table 7.1. While the best figures of merit are found at lower growth temperatures, these films also demonstrate the inclusion of Al_3Sc.

The reason for the transition from phase pure to multi-phase growth with reduced growth temperature is a temperature dependent catalytic effect of Sc. It has been suggested, though not

studied in detail or quantified, that Sc has a catalytic effect in the growth of III-Nitrides, with Frei *et al.* noting an increase in growth rate with additional Sc flux under otherwise nominally identical growth conditions including constant temperature.[132] We observe a temperature dependent catalytic effect of Sc with growth rates of the binary ScN dropping from 2.21 um/hour to 1.75 um/hour, with conditions other than substrate temperature being constant, whereas AlN has a fairly constant growth rate of 0.68 um/hour as shown in Table 7.2. This more-than-doubling of the growth rate for ScN, relative to AlN, suggests that Sc has a remarkably strong catalytic effect of cracking the pre-excited molecular nitrogen that is responsible for traditional III-Nitride plasma epitaxy.[14] The temperature dependence of this catalytic effect explains the inclusion of Al_3Sc in the lower growth temperature ScAlN XRD scans. As the Sc catalytic effect is reduced at lower temperatures, the growth rate would be lower than anticipated for ScAlN, increasing the effective III/V ratio. At a lower growth rate, adlayer accumulation would occur faster and lead to the unintentional accumulation of a thicker metal adlayer, leading to the formation of Al_3Sc upon cooling. Like other III-Nitride metal adlayers, this metal would segregate to the surface during growth, accumulating on the surface over time during growth.

Table 7.2: Growth rate at various substrate temperatures for ScN and AlN.

Material	Growth Substrate Temp. (ºC)	Growth Rate (μm/hr)
ScN	650	2.21
ScN	600	1.92
ScN	550	1.75
AlN	700	0.68

Figure 7.2 shows the AFM scans of the three ScAlN samples grown with a substrate temperature ranging from 700 to 600 ºC. The surfaces show smooth morphologies with RMS roughnesses ranging from 1.7 to 1.2 nm. The samples grown at 650 and 700 ºC appear to show broad grains, forming hill like structures with noticeable circular valleys. On a macro scale, the sample grown at 600 ºC appears to show a substantially smoother surface but also shows significant micro droplet formation, likely due to the metallic peaks shown in the XRD 2θ-ω scans. The surface accumulation of Al_3Sc is supported by Figures 7.3 and 7.2, XRD 2θ-ω and AFM scans

of the ScAlN film grown at 600 ^{o}C immediately after growth and then after a 20 minute HCL etch. Post etch, no evidence is seen of Al_3Sc nor droplets, suggesting that all metal accumulation was indeed surface level and in droplet form. Additionally, a significant reduction in surface roughness is observed post etch, from 1.3 to 0.68 nm. This could also imply that for any application in which the thin ScAlN will be the top layer of the structure, more metal surface accumulation could be allowed to increase crystal quality and reduce surface roughness, simply removing the accumulated metal via a post growth etch before device processing.

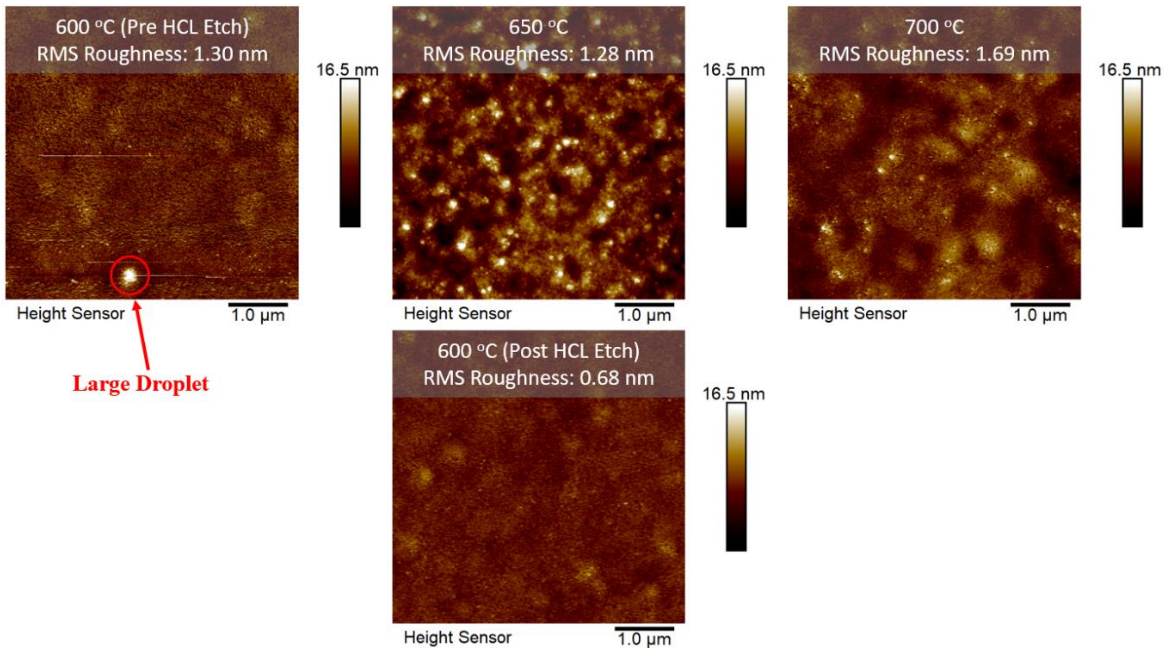

Figure 7.2: AFM scans of the ScAlN films grown under metal rich conditions at varying growth temperatures. Roughness reduction is observed with reduced growth temperature, with large droplets appearing at 600 ^{o}C.

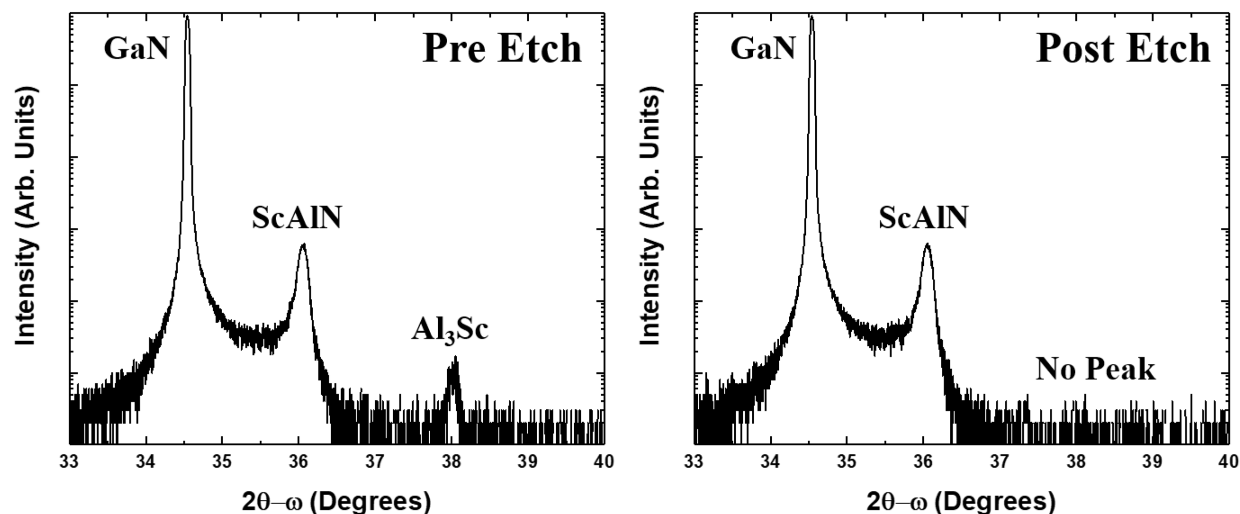

Figure 7.3: XRD 2θ-ω curves of ScAlN before and after a 20 minute HCL etch. The unintentional Al_3Sc peak is eliminated post etch.

7.3.2 Metal Dose Optimization of ScAlN Growth

A second series of ScAlN samples were grown to assess the effect of different metal rich III/V ratios on the quality and phase purity of ScAlN. The samples were grown at a substrate temperature of 650 ^{o}C at III/V ratios of 1.6, 1.4, and 1.2, adjusting both Al and Sc to keep the Al/Sc metal ratios constant while changing the metal to nitrogen ratio. The shutter timings were adjusted to account for the different metal adlayer buildup times at varying III/V ratios so as to maintain the same final metal accumulation but building up to that total accumulated amount was done at different rates. Thus, the shutter open/close times were 2, 3, and 6 s, for targeted III/V ratios of 1.6, 1.4, and 1.2 respectively. Figure 7.4 shows the XRD 2θ-ω curves for the III/V ratio variation samples, with the XRD (0002) rocking curve figures of merit being listed in Table 7.3. Figure 7.4 shows minimal change as the III/V ratio is reduced from 1.6 to 1.4, with no noticeable change in the 2θ-ω peaks and a decrease in the rocking curve FWHM. A much larger difference in XRD spectra is seen when reducing the III/V ratio further to 1.2, with the inclusion of additional

peaks at about 38° and 38.5^o likely corresponding to Al_3Sc and Al, respectively. This result at first seems counter intuitive, lowering metal richness leads to more accumulated metal. However, as the inclusion of extra metal phases is generally caused by excess metal buildup, reduction in Sc flux due to a lower III/V ratio likely causes a reduction in the previously mentioned catalytic effect owing to a reduced time averaged Sc surface coverage, reducing the growth rate and allowing for more metal adlayer buildup than intended. In fact, the growth rate was observed to decrease from 790 nm/hr for a III/V ratio of 1.6, down to 720 nm/hr for a III/V ratio of 1.2 due to this reduction in the catalytic effect. Since the growth rates are thus related to the instantaneous Sc metal coverage, the approximations of III/V ratio that are normally valid for other III-Nitride materials are invalid for Sc alloys. The 1.6, 1.4 and 1.2 effective III/V ratios are estimates based on metal consumption times (see Ref. 17 for details) observed in RHEED assuming constant growth rates throughout the MME cycle, which could be significantly erroneous due to the newly observed dynamic changes in growth rates throughout the MME cycle. Interpretation of the III/V ratio in RHEED is further convoluted by the inclusion of metal precipitates. In a MME cycle, the RHEED transient has three dominant regions, labelled in Figure 7.5 which shows a representative RHEED transient for ScAlN growth. The first region(labelled as I) is a sharp decrease in the RHEED intenisty as metal is accumulated on the surface during the metal shutter open phase. The second region (labelled as II) occurs after the metal shutters are closed and the accumulated metal is consumed into the film, resulting in an increase in RHEED intensity until the intensity reaches a plateau at the same intensity as before the metal shutters were opened. This plateau represents the third region (labelled as III), known as the "dead time", in which no growth is occuring. The III/V ratio for a given growth is determined as the ratio of the sum of the first two region times to the shutter open time. If all metal accumulated is consumed into the film, this provides a reliable in-

situ measurement of III/V ratio. However, the precipitation of metal that is not accumulated into the film will result in ambiguity, as the duration of the second region of the cycle is determined solely by the metal that is accumulated into the film. Precipitated metal will result in a decrease in the RHEED intensity over the course of the growth, but will cause little cycle to cycle variation. This issue is present in the film grown at a measured III/V ratio of 1.2. While in-situ measurements suggested a III/V ratio of 1.2, over time the RHEED intensity decreased and the post growth XRD scan in Figure 7.4 shows the presence of metal precipitates. Thus, while the measured and reported III/V ratio is 1.2, the real III/V ratio would be higher, resulting in higher than intended metal accumulation and the observed inclusion of metal.

While this misaccounting of the metal dose from RHEED explains why the presence of the metal precipitates results in an underestimate of the III/V ratio as measured by RHEED, this leaves a critcal unanswered question: why do the precipitates form as the III/V ratio is lowered. Since all filmswere grown at the same temperature, temperature seems to not be an issue. At present, the most likely hypothesis, to be explored in future work, is the slower accumulation of metal in the III/V=1.2 case compared to the III/V=1.4 and 1.6 cases, leaves a surface that is substantially less covered with metal for a longer time. This condition approches the more traditional MBE constant flux, metal rich situation which is also known to precipitate metal (see ref 7 for example). The origin as to why this precipitation happens as the III/V ratio approaches 1 remains unknown.

Figure 7.6 shows the AFM scans for the same ScAlN samples measured in Figure 7.4. When reducing the III/V ratio from 1.6 to 1.4 the RMS roughness decreases to 1 nm, similar to the trend of improved crystal quality in XRD. Reducing the III/V ratio futher, however, to 1.2 sees a significant increase in the surface roughness to 1.6 nm, matched by a loss of phase purity in XRD. These results suggest that a balance must be used in the selection of the III/V ratio and this balance

is very much dependent on the surface coverage of Sc. Growing too close to stochiometry leads to a loss of nitrogen catylitic activity and thus growth rate, leading to increased metal accumulation which improves surface adatom mobility and smoothness but can reduce phase purity. Growing too metal rich leads to increased catylitic activity, increased growth rate and thus, lower metal accumulation and surface quality giving a reduction in crystal quality. Finally, we note that compared to other non-scandium III-Nitrides, both the surface and XRD quality changes resulting from such extreme effective III/V ratio changes are much smaller. This is due to an inherent feedback mechanism operating under metal rich conditions. Specifically, as the effective III/V ratio is reduced which would normally lower material quality for MME, the reduction of active nitrogen due to the catylitic reduction provides more metal to the surface, slowing the degradation of quality.

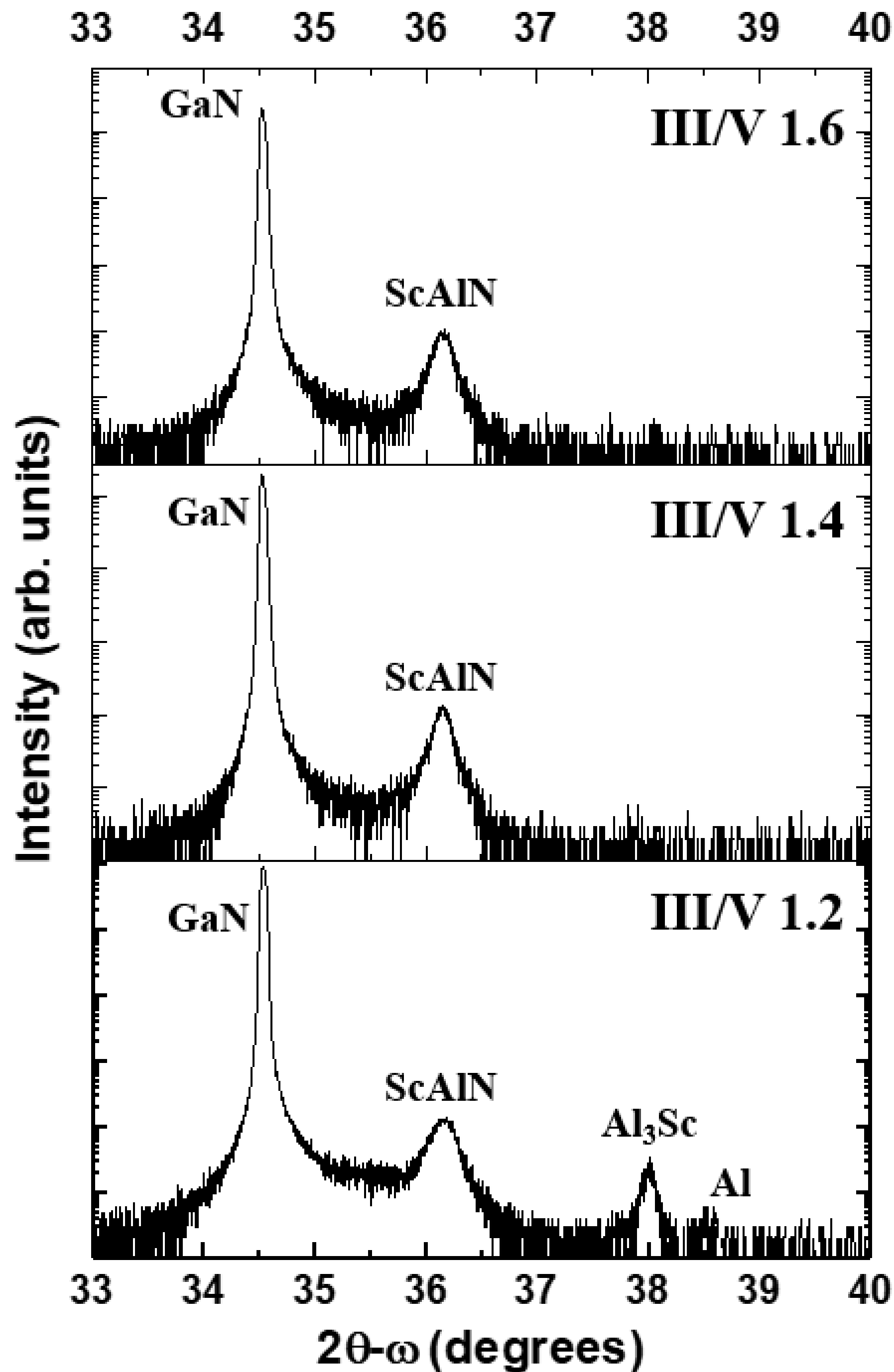

Figure 7.4: XRD 2θ-ω curves of ScAlN grown under metal rich conditions at varying III/V ratios. Single phase growth is observed at higher III/V ratios, with phase purity being lost at a III/V ratio of 1.2.

Table 7.3: XRD rocking curve FWHM values for the ScAlN films grown under metal rich conditions at various III/V ratios.

III/V Ratio	XRD (0002) RC FWHM
1.6	334
1.4	301
1.2	276

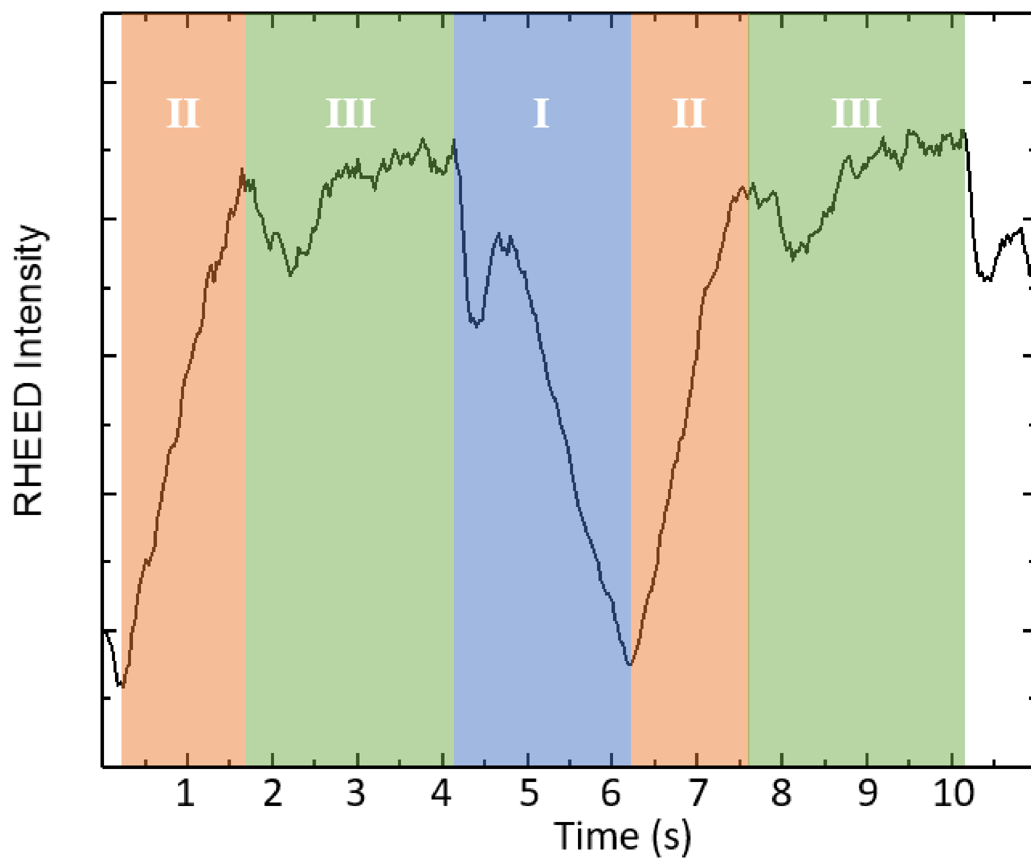

Figure 7.5: Representative RHEED transient for ScAlN growth. Defined regions for metal shutter open and thus, metal accumulation (I), metal adlayer consumption (II), and dead time (III).

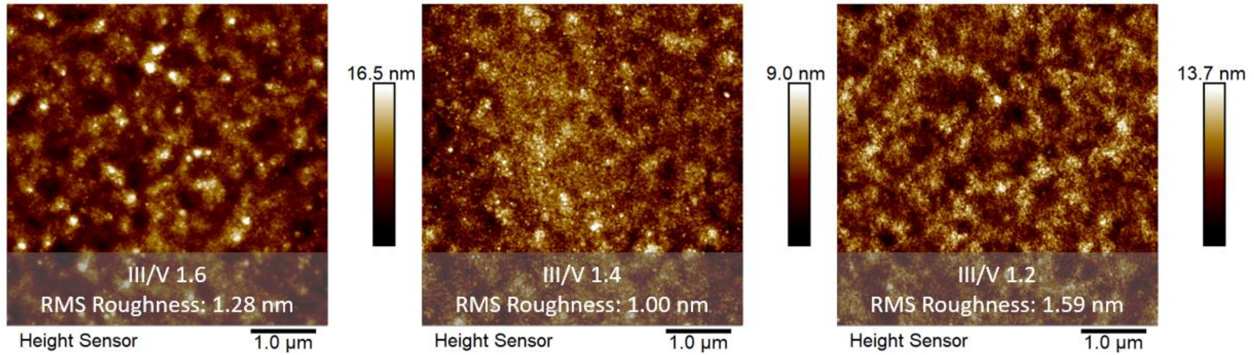

Figure 7.6: AFM scans of the ScAlN films grown under metal rich conditions at 650 °C at various III/V ratios.

7.3.3 Low Temperature Growth Yields High Crystal Quality and Lattice Constants Close to Theory

With full optimization of growth conditions and precise control of metal accumulation it is possible to grow ScAlN even at very low temperatures. Figure 7.7 shows the AFM scan and XRD scan of a $Sc_{0.18}Al_{0.82}N$ film grown at 400 °C, well below anything studied previously in this work. Here, exceptional crystal quality was obtained, with an (0002) RC FWHM of 250 arcsec and a (10-15) RC FWHM of 469 arcsec. In addition to the strong figures of merit, distinct thickness fringes can be seen around the ScAlN peak. This suggests an exceptionally smooth interface between the ScAlN and GaN films, implying that lower temperature growth not only results in improved bulk quality, but improved growth initiation. The AFM scan shows a smooth surface as well, with an RMS roughness of 0.73 nm and the presence of spiral hillocks as is typically seen when film growth progresses in a two dimensional growth mode. Of additional interest is the lattice constants of the low temperature growth vs the high temperature growth. The film grown at 650

^{o}C with the same composition resulted in a c lattice constant, calculated via XRD peak position, of 4.965 Å. This value is well below the theoretical value at this composition. From theoretical calculations, the c lattice constant of $Sc_{0.18}Al_{0.82}N$ should be about 5.024 Å.[126] On the other hand, the $Sc_{0.18}Al_{0.82}N$ film grown at 400 ^{o}C demonstrated a lattice constant of 5.027 Å. While there is some uncertainty in literature as to the exact physical parameters to be used for modelling and calculations and RBS or EDX measurements have a degree of error in determining the composition of a film, such a shift in lattice constants cannot be explained solely by such error.

The reason for such an improvement in film quality and shift in lattice constants is uncertain at this point, but some suggestions can be made. As ScN is a cubic crystal while AlN is wurtzite, it is possible that some domains of either cubic ScN or cubic ScAlN are present in the growth of ScAlN that is overall a wurtzite crystal. In low temperature growth, these cubic inclusions may be supressed. This would result in a film of greater purity, resulting in an improvement in crystal quality. This could also explain the shift in lattice constants to be closer to theory when using low temperature growth. Inclusion of cubic phases at higher temperatures would result in a distortion of the crystal lattice, either shifting bond lengths or bond angles. Further study, both experimental and theoretical, must be performed to determine the exact reason for this shift in lattice constants and improvement in crystal quality.

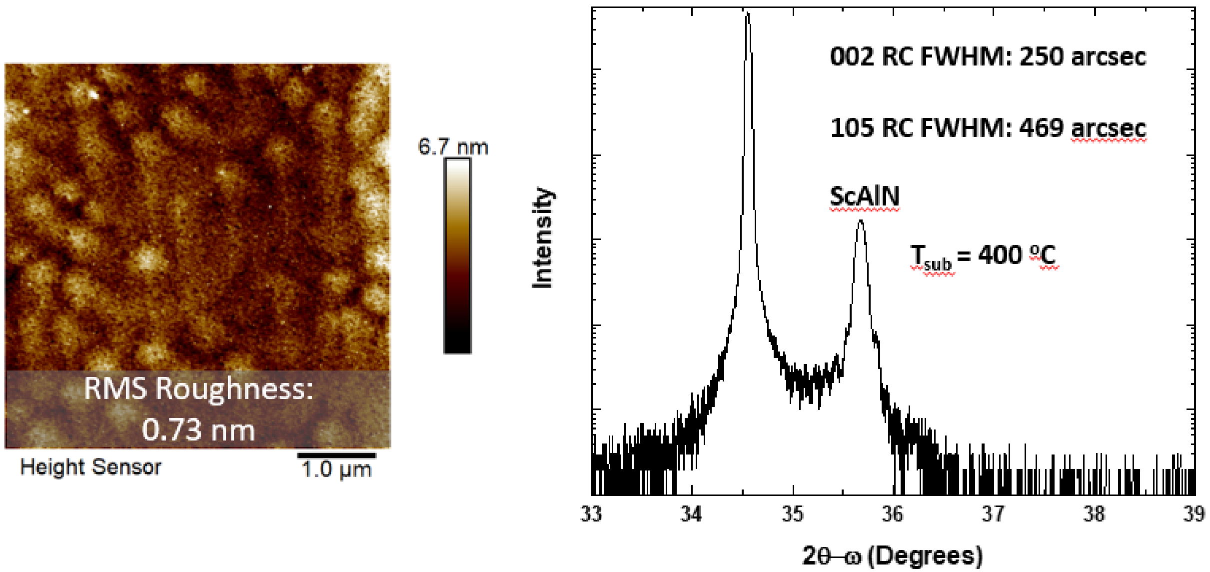

Figure 7.7: AFM scan (left) and XRD 2θ-ω scan of a $Sc_{0.18}Al_{0.82}N$ film growth at a low substrate temperature of 400 ºC.

7.3.4 High Performance HEMT Structures Demonstrated With Metal Rich ScAlN Growth

Finally, by taking all of these growth complexities into account, a ScAlN HEMT structure was grown to assess the electrical characteristics of metal rich ScAlN films. Figure 7.8 displays the XRD 2θ-ω scan and the AFM image of the 20 nm ScAlN film. The XRD shows a ScAlN (0002) rocking curve FWHM of 229 arcsec and the AFM scan shows an RMS roughness of 0.8 nm, indicating a high crystal quality and smooth surface. It was found that annealed contacts to the film as grown could not make contact to the ScAlN/GaN channel owing to the resistivity of the ScAlN and the apparent lack of alloying depth of the Ti based contacts. Thus, the contact area was etched to a thickness of 5 nm and contacts were deposited and annealed to achieve ohmic behavior and Hall measurements were performed. The mobility of the film was measured to be 700 cm^2/Vs with a sheet charge of 5.9×10^{13} cm^{-2}, resulting in a sheet resistance of 152 Ω/□. All Hall measurements were performed at room temperature. Further materials optimization and well-

known AlN/AlGaN interlayer schemes can further increase the mobility of the channel at the expense of the sheet charge and may lead to even better sheet resistance of the structure. These excellent electrical properties show the strong potential of metal rich ScAlN growth for the fabrication of HEMT structures and devices.

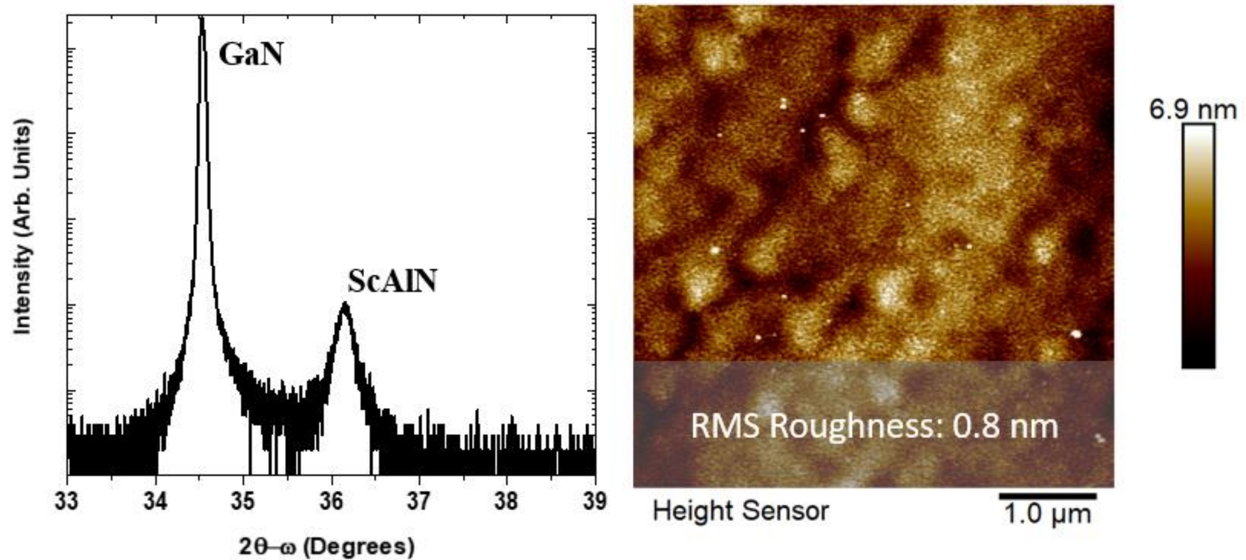

Figure 7.8: XRD 2ω-θ scan and AFM scan of the ScAlN/GaN HEMT structure showing excellent crystallinity and surface roughness.

7.4 Conclusion

Metal Modulated Epitaxy was utilized to demonstrate, phase pure, metal rich growth of ScAlN. The effects of growth temperature and III/V ratio were studied, and an x-ray diffraction figure of merit and surface roughness as low as 225 arcsec and 0.68 nm demonstrated. A significant Sc catalytic effect was quantified that results in growth rates that vary with temperature and Sc surface coverage. This reduction in semiconductor growth rate with decreasing temperature results in the metal surface coverage increasing and can result in mixed semiconductor-metal phases at lower

temperatures. By accounting for all these complexities not typically observed in traditional III-Nitride plasma MBE, a $Sc_{0.2}Al_{0.8}N$ high electron mobility transistor (HEMT) structure is grown and fabricated, demonstrating with a simple structure a sheet resistance of 152 Ω/□, a mobility of 700 cm^2/Vs, and a sheet charge of 5.9×10^{13} cm^{-2}. Such a growth method shows great potential in the advancement of ScAlN based HEMT technology.

CHAPTER 8. INVESTIGATION OF CRYSTAL STRUCTURE AND PHASE PURITY OF WURTZITE SCALN OVER A WIDE COMPOSITION RANGE

8.1 Introduction

In recent years, ScAlN has leapt into the forefront of study in the field of III-Nitrides, including growth and material development and device advancement. Enormous attention has been given to the material due the large spontaneous and piezoelectric polarization effects theorized and later observed in ScAlN/GaN heterostructures.[127,132,135] In fact, ScAlN demonstrates the largest polarization coefficients of any III-Nitride alloy as the composition shifts more Sc rich, until at a composition of 38-43% the alloy transitions to a cubic phase, causing a swift loss in polarization.[126,127] Further benefiting the material is the fact that at a composition of about 18% scandium the alloy is lattice matched to GaN, allowing for strain free heteroepitaxy of the material.[136,139,152] At this lattice matched composition the ScAlN/GaN interface sheet charge has been calculated to be ~$6x10^{13}$ cm^{-2}, more than twice that of a lattice matched $In_{0.18}Al_{0.82}N$/GaN heterointerface, a structure that has already shown great potential for high electron mobility transistor (HEMT) applications.[127] As a result, ScAlN has strong applications for future HEMT and radio frequency (RF) switching applications, with multiple groups already demonstrating high performance devices even in the early stages of development. However, epitaxy of the material is in the early phases of study and many more challenges remain to be overcome in order to harness the full potential of this material.

Early study focused on RF sputtering to grow ScAlN, especially as it proved difficult to find suitable Sc sources for other growth methods. However, as is common with RF sputtering in the development of III-Nitride materials, crystallinity issues plague performance of devices fabricated with RF sputtered material.[139–141] Metal organic chemical vapor deposition (MOCVD) has faced significant issues in ScAlN growth due to the lack of a suitable precursor.[152] Some success has been demonstrated, but it has been limited to low Sc compositions and requires growth rates significantly lower than what is typically used for more traditional III-Nitrides. In the past few years molecular beam epitaxy (MBE) has shown great success in high quality epitaxy of ScAlN. Multiple groups have performed studies on MBE growth of ScAlN and demonstrated good crystal quality on both sapphire and SiC substrates, allowing for low sheet resistance HEMT structures and further improvement in RF device performance.[130,132,134,146] Despite promising early results, improvements in epitaxy and understanding still remain to be made.

A challenge remaining to be solved is metal rich growth of ScAlN. In past MBE growth of traditional III-Nitride alloys, metal rich growth has led to improvements in material quality as well as surface and interface roughness. High crystal quality and smooth interfaces are both critical to reducing or eliminating carrier scattering mechanisms, resulting in improved carrier transport properties and improved device performance. If such benefits could be translated to ScAlN, HEMT performance could be further improved over the potential already displayed. However, thus far metal rich ScAlN growth has proved challenging. Both Hardy *et al.* and Frei *et al.* have presented studies on the effect of III/V ratio variation on ScAlN epitaxy. Both found that growth near stoichiometry or in the metal rich regime resulted in a loss of phase purity, demonstrated in the inclusion of other ScAlN phases or metal peaks in x-ray diffraction (XRD) scans.[132,135] These problems may be overcome with proper surface engineering and a growth scheme that limits

adlayer buildup to minimize the potential for phase separation and the formation of unintended metal inclusions.

Elaboration is also required on the phase transition from wurtzite to cubic ScAlN. While many reports have claimed that the transition happens in the 38-43% Sc range, others have reported differently. Some have shown that the transition can begin to occur in a composition as low as 30%, and there is evidence to show that the transition is not abrupt, likely starting with high Sc content cubic phase inclusions at a lower average Sc film content, with the concentration of these inclusions increasing with added Sc until the film becomes completely cubic.[216] Further study must be performed to clarify this transition and it is not unlikely the nature of the transition could change with growth technique and conditions.

In this study we utilize a pulse modulated MBE technique called metal modulate epitaxy MME to grow ScAlN over a wide composition range under metal rich conditions. XRD studies are performed to assess both the phase purity and crystalline quality of the films. XRD in combination with reflection high energy electron diffraction (RHEED) analysis and transmission electron microscopy (TEM) is used to study the wurtzite to cubic phase transition. Critically, thickness of the film is found to be a critical parameter for the onset of phase transitions from wurtzite to cubic. Finally, HEMT structures are grown over a range of ScAlN compositions to assess the electrical quality of the ScAlN films grown under metal rich conditions.

8.2 Experimental Details

All films in this study were grown in a Riber 32 MBE reactor using the MME technique, the details of which can be found elsewhere.[142,143,153] All samples were grown on 1×1 cm^2 hydride vapor phase epitaxy (HVPE) unintentionally doped (UID) GaN on sapphire templates, except for

the HEMTs structures which were grown on HVPE grown semi-insulating GaN:Fe templates. The substrates were single-side polished and 2 μm of tantalum was sputtered on the backside to facilitate uniform heat absorption during growth. Prior to growth the substrates were cleaned using a 3:1 solution of H_2SO_4:H_2O_2. This clean was followed by a rinse with de-ionized (DI) water and a brief dip in dilute HF to reduce surface oxides, after which the sample was again rinsed with DI water and dried with N_2. After the chemical cleaning procedure, the samples were loaded into an introductory vacuum chamber with a base pressure of $\sim 1 \times 10^{-9}$ Torr in which they were outgassed at 200 °C for 20 minutes. Prior to growth, the samples were further outgassed at 675 °C, as measured via thermocouple, in the growth chamber. Following the outgas, the samples were further cleaned using three cycles of gallium adsorption and desorption to further remove oxygen from the surface.

During growth, aluminum and gallium fluxes were provided by conventional effusion cells and the scandium flux was provided via a high-temperature effusion cell. An initial series of ScAlN films were grown with thicknesses of 100-150 nm with varying Sc content. The content was adjusted by changing the metal fluxes to achieve a nominal metal ratio. Prior to the ScAlN layers, a 100 nm thick GaN layer was grown to bury contamination and provide a smooth regrowth surface. Three HEMT structures were grown consisting of a 20 nm ScAlN layer atop 200 nm UID GaN grown on a semi insulating GaN:Fe template. The ScAlN composition of each structure is varied and is detailed later. During ScAlN growth, the Al and Sc shutters were shuttered synchronously. Nitrogen was provided by a Veeco UNI-Bulb radio frequency (RF) plasma source with an RF power of 350 W and a gas flow of 1.25 SCCM, yielding a growth rate of 0.69 nm/hr for AlN.

In situ surface monitoring was performed using (RHEED) to calibrate III/V ratio and metal doses, and postgrowth XRD analysis was performed with a Philips X'pert Pro MRD using a Cu Kα1 anode. TEM measurements were performed using an F30 FEI Tecnai. Hall measurements were performed with a LakeShore M91 fast hall system. ScAlN etching was done with a Plasma Therm inductive coupled plasma (ICP) dry etch and Ti/Al/Ni/Au contacts were deposited via e-beam evaporation, followed by a 1 minute anneal at 925 ^{o}C under nitrogen atmosphere.

8.3 Results and Discussion

8.3.1 Shift of Lattice Constants with Composition

Figure 8.1 displays XRD 2θ-ω curves for 7 ScAlN films grown with a composition between 9 and 41% Sc. Composition was determined either via EDX or RBS and is subject to an error of about ±1%. The a and c values for the 41% Sc film are not shown as the film has transitioned to a cubic phase and no longer displays hexagonal peaks, as will be discussed later. The 9% to 35% films all show only a single wurtzite ScAlN peak in both the symmetric 2θ-ω scans shown and the reciprocal space maps (not shown here), suggesting a predominantly, or fully, wurtzite film. It should be noted that if an additional cubic phase is present it is possible that either the peak would not be detected in such scans and would require additional exploration of reciprocal space, similar to what was observed by Satoh *et al.* or would be too low intensity to detect.[216] The 41% Sc sample deviates from this trend however. At 41% a ScAlN peak is observed at ~36°, but two additional peaks are also present. While it is difficult to identify what exactly the additional peaks correspond to, there are a few likely options. The first would be intermetallic Al_xSc_y phases. The two peaks are at about 38 and 38.5^{o}, which are close to Al_3Sc and Al, which have 111 peaks at 37.94 and

38.61° respectively.[214] While the proximity of the measured peaks to these theoretical values makes these metallic phases likely, another possibility is the inclusion of cubic ScAlN phases. At an average film composition of 41% Sc, the film lies within the wurtzite to cubic transition point, stated to be 40-44% Sc depending on the reference.[137] As a result, it is possible that these extra peaks correspond to a cubic phase, but without knowledge of the composition of these cubic phases from a high resolution source like transmission electron microscopy or atom probe tomography it is difficult to determine exactly what cubic planes the peaks would correspond to.

Figure 8.2 displays the a and c lattice constants vs composition for the films extracted from the (0002) peak position and the (10-15) peak position (located via reciprocal space map) respectively. I note that the two extremes, ~9%Sc and ~34% Sc show the largest deviation from the middle data trend clustered around an a-lattice constant strained to GaN at ~3.186 angstroms. This is not surprising as these two films are likely relaxed due to the larger lattice mismatch. The trend in the c-lattice constants for Sc greater than the lattice matched composition (Sc~>18%) shows the expected trend. Specifically, the c-lattice constant for this range of compressive strain shows a progressively increasing c-lattice constant as the composition deviates from the lattice matched case. Interestingly, the trend in c-lattice constants does not match with a consistent compositional shift in wurtzite phase material when the tensile strained film (~12% Sc) is considered. It would be expected that with increasing Sc content, the c lattice constant would decrease, provided that the film maintains pure wurtzite nature and is relaxed. For a compressively strained film (the case for the middle points as evidenced by the a-lattice constant) the strain could offset or overwhelm this decrease leading to a larger overall c-lattice constant. But for the tensile strained film with ~12% Sc, the strain and the increase in Sc should work in the same direction to lower the lattice constant. In the case of the first two films, the c lattice constant held near that of

AlN, followed by a decrease as the lattice matched film is approached, but then begins to increase past ~24% Sc as compressive strain kicks in. While this behavior aligns with simple theory for the compressive strained films, the dramatic magnitude of the c-lattice increase does not align with the expected value for increasing Sc content in pure wurtzite ScAlN. The large increases in c-lattice constant with increasing Sc could be explained by the inclusion of high Sc content cubic phases within the films with increased Sc content. The inclusion of high Sc content cubic films would lead to a reduction in Sc content within the wurtzite phase measured in XRD, yielding lattice constants closer to AlN. This effect is further realized in the 34% Sc case where the strain is lost (film is relaxed) and the c-lattice constant drops considerably. This will be discussed further in section 8.3.2.

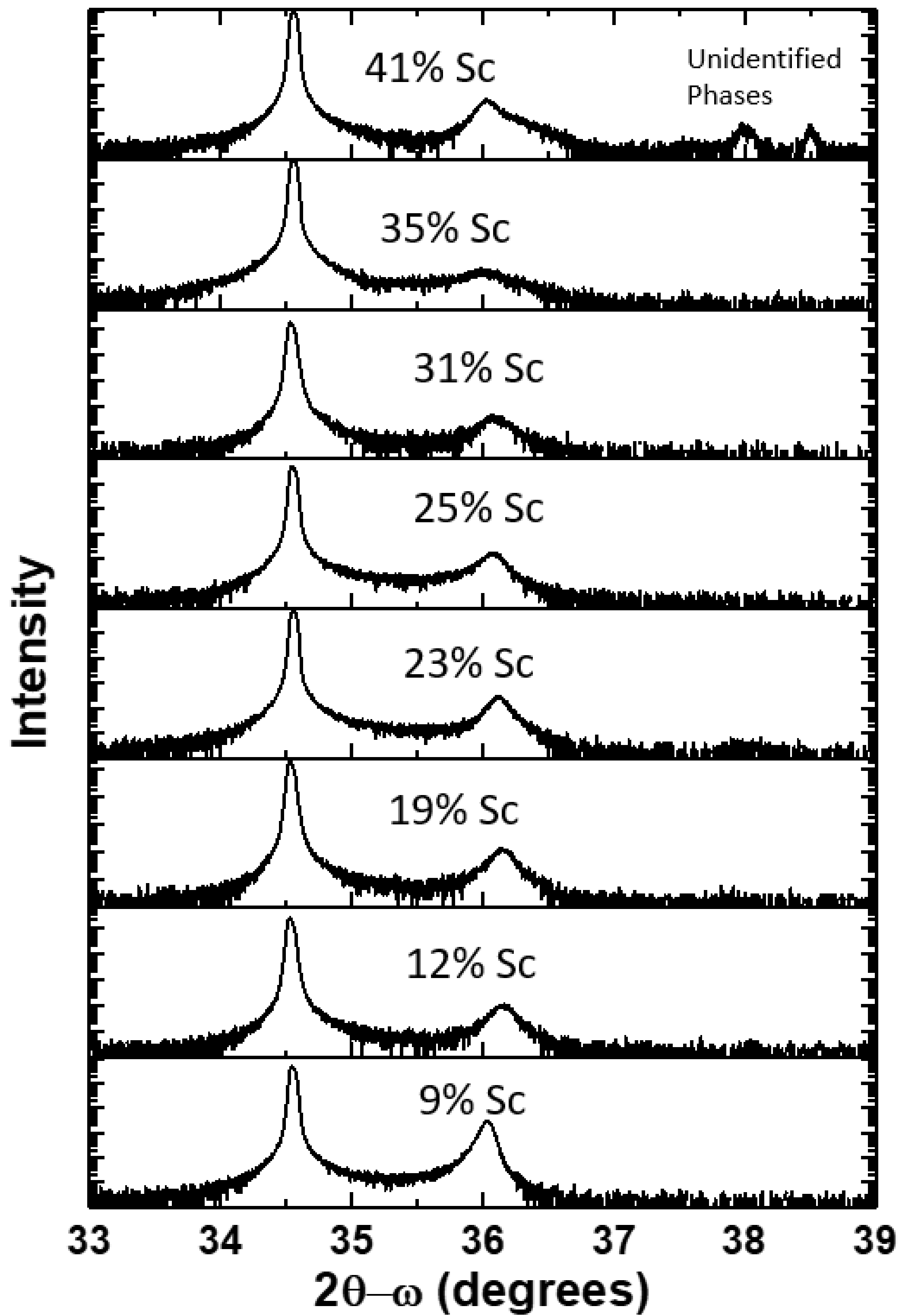

Figure 8.1: XRD scans of ScAlN films grown via MME over a wide composition range.

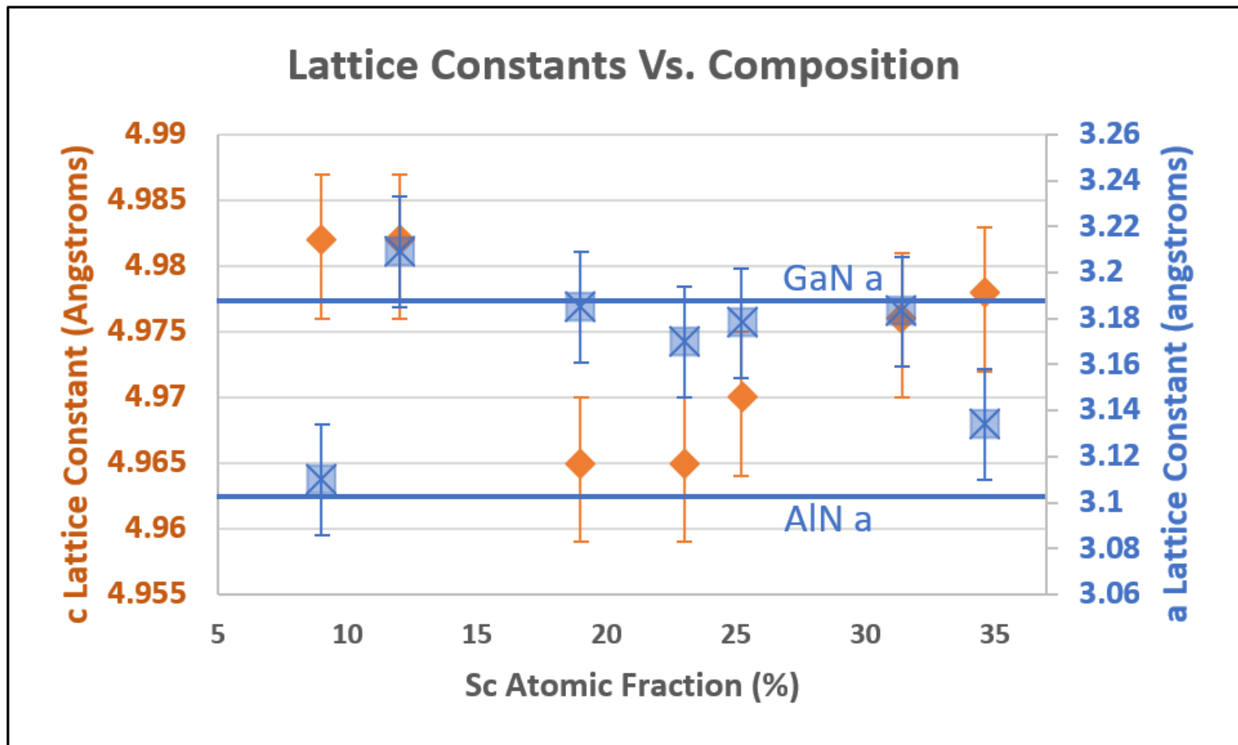

Figure 8.2: Wurtzite lattice constants vs Sc content for the ScAlN films.

8.3.2 Phase Transition From Wurtzite to Cubic ScAlN

While it has been observed in literature that ScAlN transitions from a wurtzite phase to a cubic phase at 40-44% Sc, it has also been observed that this transition begins at a lower Sc content with the inclusion of cubic phases.[216] This phenomenon may elucidate the odd lattice constant shifts observed in the previous section at high Sc composition. Evidence of this shift within our films can be seen in figure 8.3. Figure 8.3 displays the end of growth RHEED images for the samples grown between 9 and 41% Sc. The samples with compositions between 9 and 23% Sc show pure wurtzite nature in the RHEED patterns. The patterns are streaky, with horizontally elongated spots, suggesting no evidence of alternate phases or a polycrystalline film. The RHEED pattern of the 25% Sc sample begins to show a different nature. The pattern changes from streaky, horizontally elongated spots to a pattern that has less horizontal elongation of the spots.

Additionally, the spots begin to widen vertically, indicative of the inclusion of a spread in lattice constants suggesting more than one phase and a transition towards a polycrystalline growth. This worsens as the composition shifts to 31 and 35% Sc as the pattern loses all trace of streakiness and the spots elongate vertically further, beginning to form arcs as the films become more polycrystalline. At 41% Sc the all the spots have become wide arcs, though the pattern has not taken on the ring nature of a fully polycrystalline material, suggest that the film still has a predominant phase.

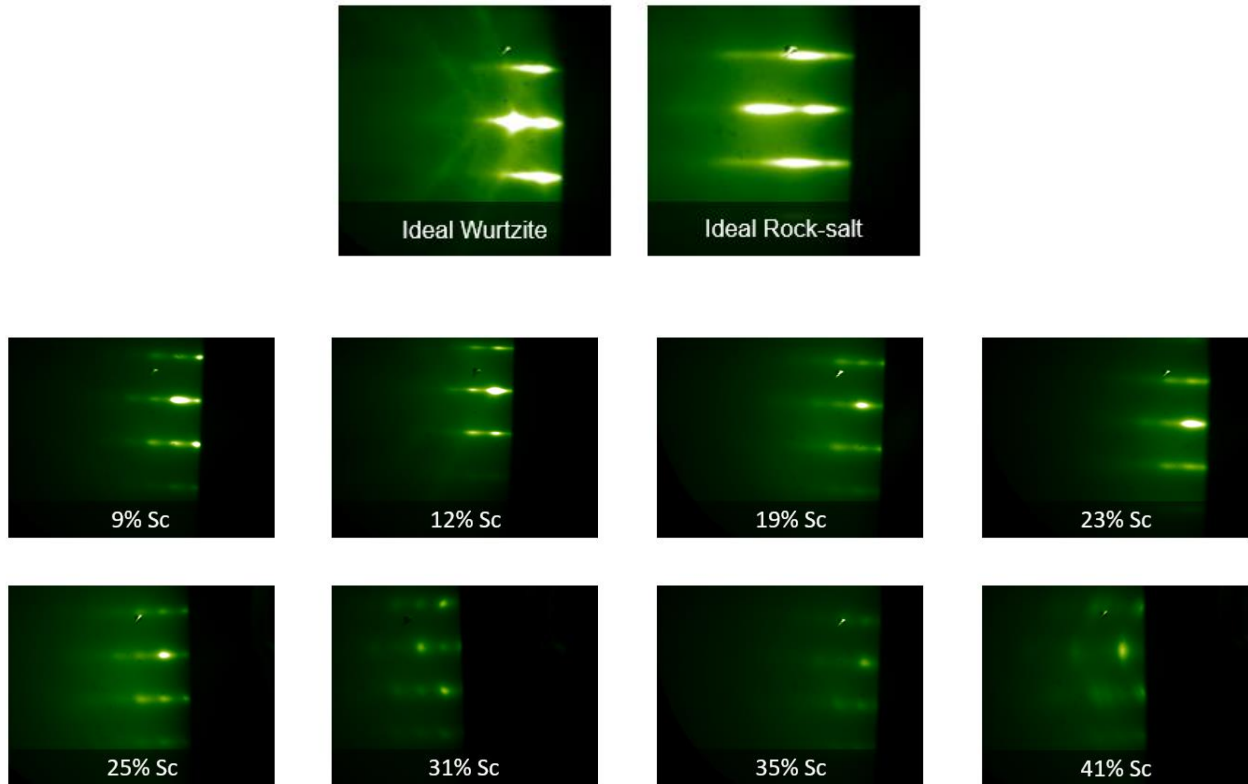

Figure 8.3: End of growth RHEED images for the ScAlN films showing a progression of surface features with changing Sc content, as well as in ideal wurtzite and rock-salt RHEED pattern,.

This shift in RHEED patterns aligns well with a transition from pure wurtzite phase ScAlN to mixed wurtzite/cubic material. A similar observation was found by Satoh *et al.* where films grown with compositions between 30 and 41% Sc were mixed wurtzite and cubic phases.[216] Further evidence of mixed phase material with higher Sc content can be seen in Figure 8.4. Figure 8.4 shows TEM diffraction patterns for the $Sc_{0.35}Al_{0.65}N$ films, with image 1 being taken for the underlying GaN film, and image 2 being taken for the $Sc_{0.35}Al_{0.65}N$ film. While the GaN film shows a typical wurtzite diffraction pattern, under the same beam conditions the ScAlN film shows a much more convoluted pattern with multiple c-axis lattice constants/diffraction peaks all having the same approximate a-lattice constant (strained to GaN). While the same core wurtzite pattern is present and produces the brightest spots, significant inclusions of other patterns is observed. While the source of the extra patterns cannot be determined by just the diffraction pattern, the presence of these extra patterns indicates that the film is not purely wurtzite, reinforcing the idea that ScAlN takes on a mixed phase nature with increasing Sc content as the wurtize to cubic transition point is approached.

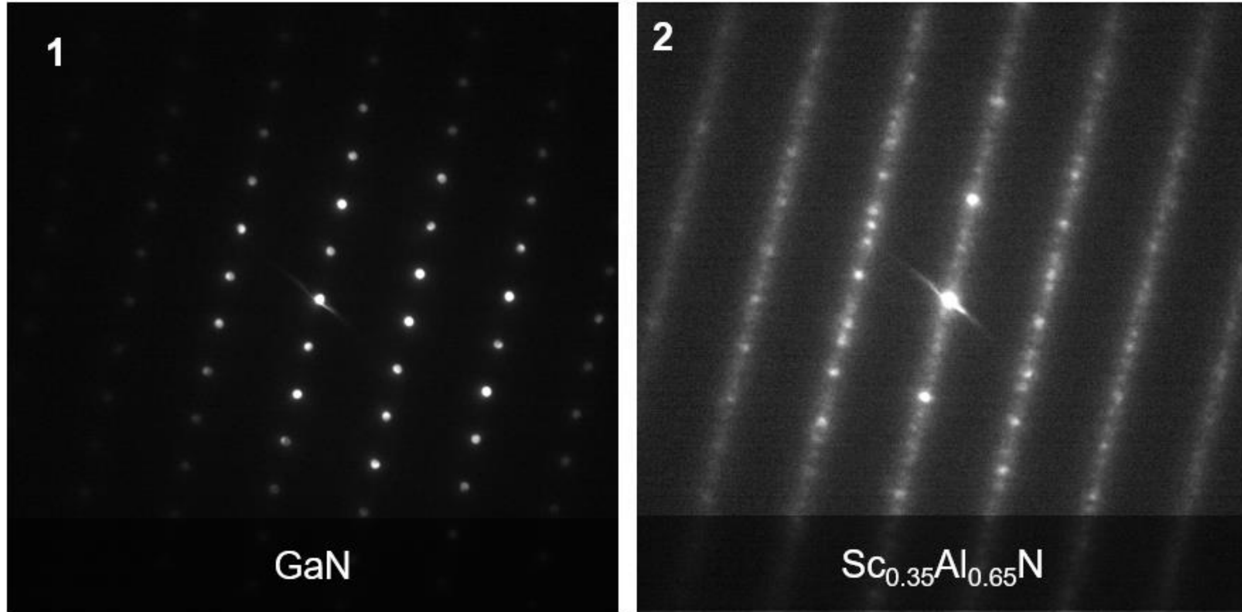

Figure 8.4: TEM diffraction patterns of a GaN film (left) and a $Sc_{0.35}Al_{0.65}N$ film (right) showing a shift from a pure wurtzite pattern to a pattern containing multiple phases.

Of further note, the inclusion of high Sc content cubic phases would explain the shift in lattice constants previously observed at high Sc compositions. High Sc content cubic material would reduce the Sc content available for incorporation in the wurtzite phase material. As the wurtzite peak is the dominant peak in XRD measurements, the XRD extracted lattice constants would correspond to a lower Sc content than the global average Sc in the entirety of the ScAlN film. This global average Sc composition for a ScAlN film is measured by EDX or RBS, which would give an average of the overall film content without regards for the phase. Thus, as cubic inclusions increase in density with higher average film Sc content, the Sc content in the wurtzite phase would continue to decrease as Sc precipitates out into the cubic phases, resulting in a shift in lattice constants towards that of AlN. This is observed in the lattice constant data presented in Figure 8.1 in section 8.3.1. In order to study the true experimental lattice constants of wurtzite

phase ScAlN up to the phase transition, the inclusion of non-wurtzite phase would have to be suppressed in some way.

One potential method for the suppression of non-wurtzite phases is limiting film thickness. For growth of thin films, the ScAlN layer will be strained to the underlying GaN layer. While strained to the GaN layer, the most energetically favorable crustal structure will be the same wurtzite structure as the GaN substrate. As a result, if growing below a certain thickness the formation of a cubic phase will be suppressed in the film, resulting in a purely wurtzite ScAlN layer. This can be seen in Figure 8.5, which shows the end of growth RHEED images for a 20 nm and a 150 nm ScAlN film grown at the same composition of 41% Sc. The RHEED patterns show significantly different nature for the two films. The thicker film at 150 nm shows severe polycrystalline nature due to a mixed wurtzite and cubic phase material. The 20 nm film, however, shows a pure wurtzite RHEED pattern, with no vertical elongation of the spots and a generally horizontally streaky pattern. While this method allows for the growth of thin films suitable for applications like HEMTs, which only typically require 5 to 20 nm of material for the barrier layer, it does not allow for accurate determination of all the lattice constants within the film. While at 20 nm the (0002) ScAlN peak will be present in an XRD 2θ-ω scan, this peak will only give information on the c lattice constant of the material. An asymmetric peak, like the (10-15) or (10-12) would be needed to determine the a lattice constant of the films, but at 20 nm thickness such peaks would be too low intensity to measure. Therefore, limiting the film thickness will be useful for studying device applications of wurtzite ScAlN over a wide composition range, another method of cubic phase suppression must be found for an in-depth materials studies.

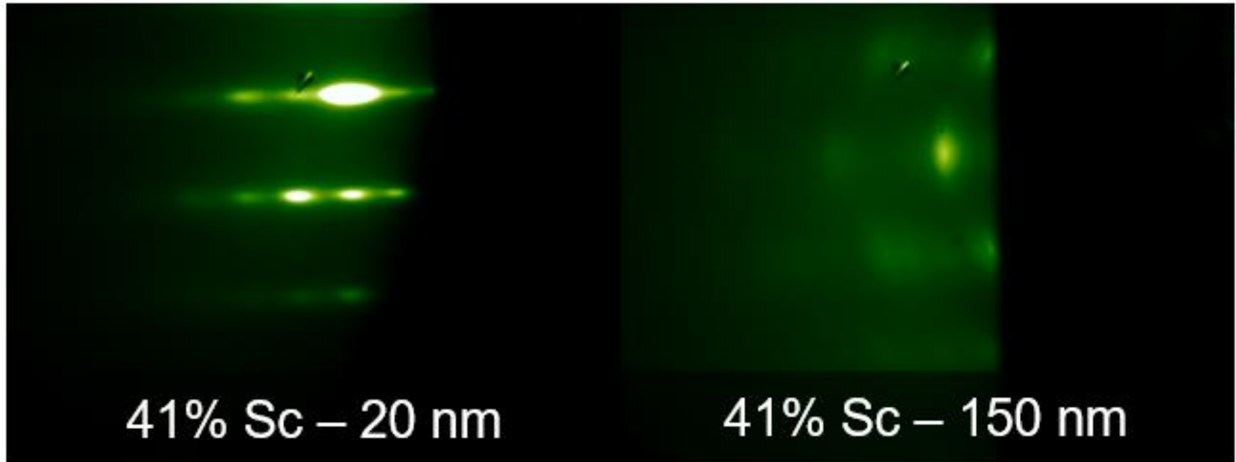

Figure 8.5: End of growth RHEED pattern for a 20 nm thick (left) and 150 nm thick (right) $Sc_{0.41}Al_{0.59}N$ film. The 20 nm film retains pure wurtzite RHEED pattern while the thicker film shows a polycrystalline nature.

8.3.3 Electrical Performance of ScAlN Films Over a Range of Wurtzite Compositions

In order to test this material for HEMT device viability, three HEMT structures were grown at ScAlN compositions of 19, 31, and 41% Sc. In order to form contacts for hall measurements, ~15 nm of ScAlN was removed via a chlorine based ICP dry etch and a stack of Ti/Al/Ni/Au (20/200/40/50 nm) was deposited, following a rapid thermal anneal at 925 ^{o}C in a nitrogen atmosphere. Figure 8.6 shows the measured hall sheet resistance and sheet charge of the three samples vs. composition. At 19% Sc, a nearly ideal sheet charge of 5.9E13 cm^{-2} compared to theory of 6E13 cm^{-2} is observed, resulting in a sheet resistance of 152 Ω/□. This sheet resistance is state of the art for III-Nitride HEMTs.[132,135,136] The sheet charge reduced to 4.1E13 (vs theory of 4.2E13 cm^{-2}) and 1.2E13 cm^{-2} (vs theory of 1.2E12 cm^{-2} but 39% Sc is indeed of 1.2E13 cm^{-2}) as the composition changed to 31 and 41%, with a corresponding increase in sheet resistance. This loss of sheet charge resulted from a decrease in net polarization due to a rapid increase in the piezoelectric polarization countering the large spontaneous polarization of the material. A loss of

polarization could also be the result of the previously discussed shift from wurtzite to cubic crystal structure in the 31 and 41% Sc films, however at a thickness of only 20 nm the inclusion of cubic phases are suppressed, as shown in section 8.3.2 and is evidenced by Figure 8.4, comparing the RHEED pattern at the end of the ScAlN layer for the HEMT structure with 41% Sc (20 nm) and the thicker film (150 nm) with 41% Sc. These films show state of the art electrical performance, even without the use of common AlN based interlayers to improve interface mobility. The use of these interlayers has been shown to improve device performance by enhancing mobility but comes at the cost of reduced sheet charge. Typical interlayers use 2-3 nm of AlN or a combination of AlN, GaN, or AlGaN, but even such thin films will screen the polarization of the ScAlN layer. This results in the sheet charge being reduced by half or more, resulting in increased sheet resistance despite the improved mobility of the channel. Thus, this method of ScAlN shows great potential for the development of HEMT devices without the need for interlayer structures to improve device performance.

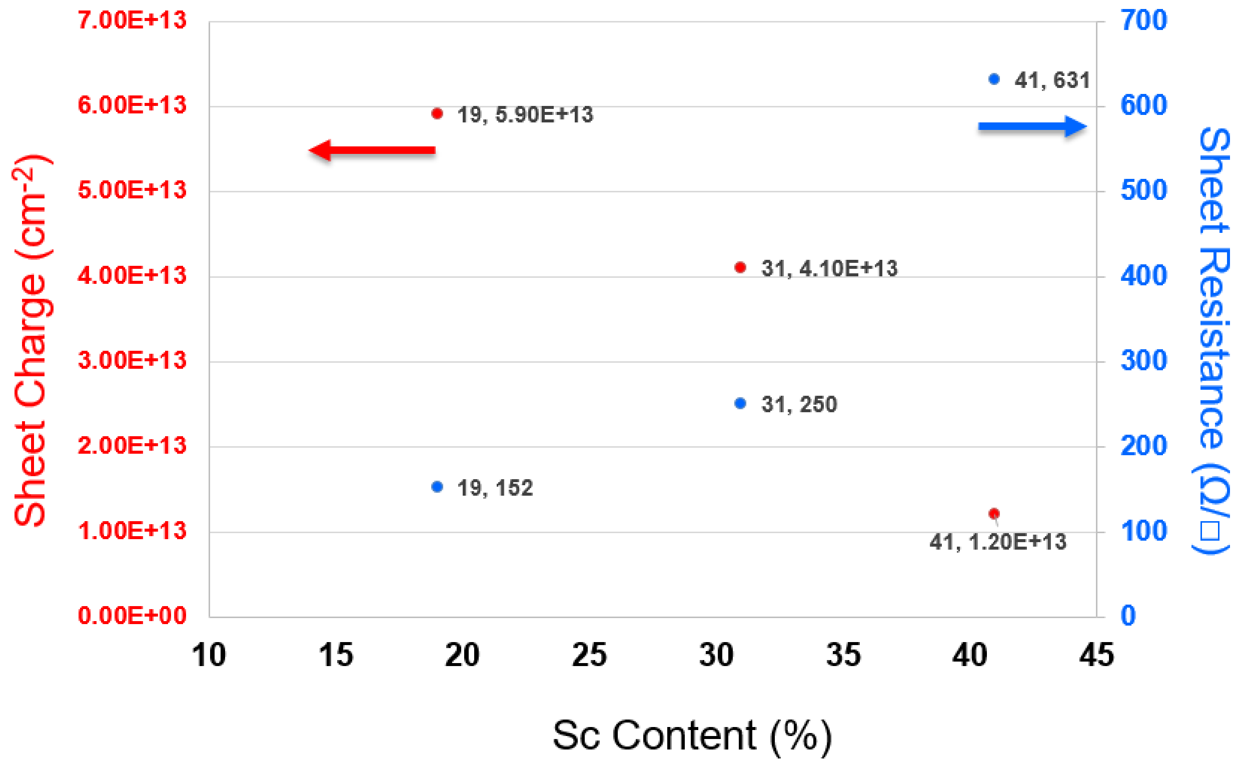

Figure 8.6: Sheet charge and sheet resistance of three ScAlN HEMT structures grown at different Sc compositions.

8.4 Conclusion

Metal rich epitaxy of ScAlN was investigated over a wide range of compositions within the theoretical wurtzite structure composition regime. ScAlN films with compositions between 9 and 41% Sc were grown with metal modulated epitaxy and were investigated structurally with XRD, RHEED, and TEM. Single phase material was observed in XRD scans up to a composition of 41 % Sc, in which additional peaks began to appear within the scan. However, an unexpected trend in lattice constants was observed with increasing Sc content. At a composition of about 25% Sc, lattice constants began to diverge from the expected values for pure wurtzite material. RHEED analysis suggested that the films began to phase separate at compositions above 25% Sc, despite the lack of additional peaks within the XRD scans. The shift in RHEED suggested the formation

of a non-wurtzite phase, with the most likely phase being a high Sc content cubic ScAlN phase. This mixed phase film nature is confirmed with TEM on a sample of 35% Sc, showing within the TEM diffraction pattern a significant number of extra, non-wurtzite, diffraction spots. This resulted in reduced Sc content in the wurtzite phase ScAlN, providing a likely explanation for the unexpected lattice constants trend. Finally, 20 nm ScAlN films at various compositions were grown on GaN to assess the electrical characteristics of the 2D sheet charge at the ScAlN/GaN interface. At the lowest Sc content of 19% a sheet charge of $5.9x10^{13}$ cm^{-3} and a state of the art sheet resistance of 152 Ω/□ were observed, with electrical characteristics degrading with increased Sc content until at a composition of 41% Sc the sheet charge and sheet resistance were measured to be $1.2x10^{-13}$ cm^{-3} and 631 Ω/□. This metal rich method of ScAlN growth shows extreme potential for the improvement of ScAlN material properties and HEMT devices utilizing the material for the advancement of RF applications.

CHAPTER 9. SUMMARY AND FUTURE DIRECTION

9.1 Low Temperature Epitaxy of In-Rich AlInN

Novel, low temperature epitaxy methods were investigated for the growth of high In content AlInN films. An initial study was performed focusing on a single composition of 30% Al to establish growth conditions for the alloy. Substrate temperature conditions were studied, and the best film quality was found when using a temperature of 350 ^{o}C, far below what is typically used for Al bearing alloys. Record crystal quality for this composition was achieved at this temperature, with XRD figures of merit demonstrating an 11x improvement over previous literature. Under these conditions, exceptionally smooth surfaces were obtained with RMS roughnesses as low as 0.4 nm. Strong photoluminescence emission is observed for the AlInN films, with a peak at about 1.45 eV which agrees well with theory. Additionally, oscillations are observed within the films suggesting the source of the emission being from quantum confined structures.

The study was expanded to a wide composition range, with films being grown between 10% and 50% Al. Under the same low temperature growth conditions excellent crystal quality was demonstrated over this wide composition range. The XRD (0002) RC FWHM values were as low as 135 arcsec and the (10-15) RC FWHM was as low as 886 arcsec. Smooth surfaces were again demonstrated with RMS roughnesses between 0.4 and 1.1 nm. Compositions between 10 and 30% Al showed strong photoluminescence emission but increasing the Al content further lead to a loss of intensity and emission energy that remained pinned to a near constant value. Spectroscopic ellipsometry was performed to determine the band gaps of the material and the band gap energies were found to agree well with theory. In addition, SE measurements showed a high absorption

coefficient for the material, suggesting strong promise in photovoltaic or photodetector applications.

9.2 Hyper Doping of AlGaN for Electrical and Optical Device Applications

Building off previous demonstrations by the group of exceptionally high electron and hole concentrations in GaN, doping of a wide range of AlGaN compositions, with Mg for holes and Si for electrons, was studied. MME was applied to dope AlGaN with a composition range from 0 to ~60% Al and hall measurements were performed to determine the electrical properties of the films. Increasing the Al content resulted in reducing the electron concentration within AlGaN films from 1.8E20 to 3.8E19, with a corresponding decrease in mobility and increase in resistivity. Increasing the Al content of the films resulted in a much larger drop in hole concentration for the films, from 1.5E20 to 3.6E18 with corresponding shifts in resistivity and mobility. With doping conditions being established, the device applications of these films are studied. PN diodes are grown and fabricated with these extreme doping levels and demonstrated tunneling behavior. Negative differential resistance is observed up to an Al content of 19%, while high reverse bias tunneling current is observed up to 58% Al. These tunnel diodes are applied as tunnel contacts to AlGaN based UV LEDs emitting at 275 nm and result in an increase in output current of over 100% at 7.5 mA.

9.3 Investigation of Formation Mechanisms for AlGaN Self-Assembled Superlattices

To eliminate the growth interrupts that lead to interface contamination in the epitaxy of superlattice structures a novel method of self-assembled superlattice (SASL) growth is investigated. The effects of various growth conditions were studied to engineer the structure of the SASLs. Metal dose was determined to have a strong effect on the thicknesses of the individual

layers. Metal dose changes were found to result in a change in composition for the thinner, Ga-rich well layers, but have little effect on the composition of the thicker, Al-rich barriers. Photoluminescence measurements reveal a controlled shift in emission energy from the wells, confirming control over the well composition. The effect of III/V ratio on the SASL structures was investigated and was found to be the controlling factor in the well to barrier thickness ratio. The well thickness was found to be a fraction of the barrier thickness equal to the III/V ratio minus one. The III/V ratio also had a strong effect on the well composition, with higher III/V ratios resulting in a closer matching of composition between the well and barrier layers. Finally, the effect of growth rate was studied for the SASL structures. While the growth rate had no meaningful effect on the composition or well to barrier ratio, changing it did alter the thickness of the overall period. Additionally, higher growth rates were found to result in increased coherency within the SASL structure, with reduced variation in layer thickness and composition in thick SASL stacks.

9.4 Metal Rich Epitaxy of ScAlN for HEMT Improvement

Metal rich growth methods for epitaxy of ScAlN films were investigated to improve the material and electrical properties. Prior to this work no success has been demonstrated in metal rich growth of ScAlN, with all previous attempts resulting in phase separation and/or the inclusion of intermetallic phases in the film. Here, phase pure metal rich growth of the material is demonstrated using precise control of metal adlayer accumulation at a composition of 18 % Sc. Excellent crystal quality was demonstrated, with an XRD (0002) RC FWHM as low as 225 arcsec and surface RMS roughness as low as 0.7 nm. In addition, HEMT structures were grown and processed for hall measurements to assess the electrical properties of the films. A state-of-the-art sheet resistance of 152 Ω/□ is measured, being the lowest reported in the literature for this material. The sheet carrier concentration was measured to be 5.9×10^{13} cm^{-2}, near the theoretical value for

the material at this composition. The study was expanded to a wide range of compositions to study the effect of this growth method on the phase transition from wurtzite to cubic material. While all films showed only a single crystalline peak in XRD measurements, pure wurtzite material was only demonstrated up to a composition of ~24% Sc. As additional Sc was added to the crystal, high Sc content cubic ScAlN inclusions began to form, seen in RHEED analysis and TEM measurements. These inclusions become more prevalent with increasing Sc content, resulting in a polycrystalline film at an average film composition of 41% Sc. However, it was observed that at low film thicknesses (20 nm) the film remains wurtzite even at a composition as high as 41% Sc. As a result, HEMT structures were able to be fabricated at high Sc contents to be analyzed with hall measurements. Increasing Sc content resulted in a reduction in sheet charge and an increase in sheet resistance, as to be expected from a reduction in polarization at the ScAlN/GaN interface.

9.5 Contributions

1. Identified a low temperature growth regime in which to grow AlInN for significant improvements in crystal quality.
2. Increased crystal quality of high In-content AlInN by up to 11x over previous literature values as well as made improvements to surface roughness.
3. Identified quantum-confined like emission from bulk AlInN films, enhancing photoluminescence emission.
4. Revealed strong stokes shift in higher In content AlInN films.
5. Measured the absorption coefficients and bandgaps for AlInN via spectroscopic ellipsometry.
6. Demonstrated high p and n type doping for AlGaN films with contents from 0 to ~60 % Al.

7. First ever demonstration of an AlGaN homojunction tunnel diode.
8. Achieved tunneling in an AlGaN homojunction diode up to an Al content of 62%.
9. Applied AlGaN tunnel diodes as a contact layer to a UV LED increasing light output power by over 110%.
10. Utilized surface chemistry engineering to develop a method to grow AlGaN self-assembled superlattices.
11. Demonstrated control over structural parameters of AlGaN SASLs via modification of growth conditions.
12. Investigated photoluminescence emission from SASL structures and found control over emission energy by modifying the well layer parameters.
13. Eliminated the need for growth interrupts in the epitaxy of thick AlGaN superlattice structures.
14. Established conditions for the growth of coherent SASL structures up to nearly a micron thick.
15. Utilized a novel initiation scheme for ScN epitaxy on GaN to improve interface and surface roughness.
16. Increased film coherency in a ScN film utilizing a low temperature Sc buffer layer.
17. Revealed a significant temperature dependent catalytic effect in ScN growth, increasing growth rate of the material to more than twice that of traditional III-Nitride alloys.
18. Established growth conditions for metal rich epitaxy of phase pure ScAlN.
19. Improved crystal quality of $Sc_{0.18}Al_{0.82}N$ lattice matched to GaN with XRD (0002) RC FWHM values as low as 225 arcsec.

20. Demonstrated state of the art electrical properties for a ScAlN/GaN heterostructure, with a 2D sheet charge density of 5.9×10^{13} cm^{-2} and a sheet resistance of 152 Ω/□.
21. Elucidated the phase transition from wurtzite to cubic ScAlN including an intermediate regime with mixed phase inclusions.
22. Successfully grew pure wurtzite ScAlN thin films with compositions as high as 41%, near the theoretical wurtzite to cubic transition regime.

9.6 Future Directions

9.6.1 Overcome PL Emission Pinning for AlInN Films

While AlInN films grown with high indium content show high potential for photodetector or photovoltaic applications due to their high absorption coefficients over a wide range of relevant bandgaps, challenges remain if the materials are to be applied to LED or other optical emission applications. The presented photoluminescence energy level pinning presents a serious challenge in applying the material to LEDs. Investigation of the source of this pinning must be performed in order to assess if this is an issue related to defect generation during growth or potentially nanoclustering like what is observed in InGaN. If a growth-related issue is present, steps must be taken to optimize the growth to overcome this energy pinning. Alternatively, if such a Stoke's shift is innate to the material and cannot be overcome electroluminescence studies should be performed to assess if electrical excitation produces a different stokes shift compared to optical excitation. The later requires control over doping to make pn junctions which has not been achieved due to a large residual electron concentration in In-rich AlInN.

9.6.2 Fabricated LED Structures With AlGaN SASL Structures

While the formation of AlGaN self-assembled superlattices has been demonstrated and parameters for customization of the SASL structures have been found, the use of such structures in device applications must be studied. Likely the most technologically applicable test would be use of such SASL structures as multi quantum wells in a UV LED. Fabrication of a UV LED structure with a 3-5 period MQW structure formed with this SASL growth method would allow for the assessment of optical uniformity between each quantum well. Additionally, comparison of the SASL MQW LED to a LED designed for the same emission energy with a traditional growth method would allow for a comparison of the EQE between this novel growth method and a more traditional fabrication method.

9.6.3 Investigate Low Temperature Growth of ScAlN for Device Applications

Recent studies, both in this work and by groups in literature, have suggested that low temperature growth yields higher quality ScAlN films. The exact reason for this needs to be elucidated but could be suppression of unintended cubic phases at lower temperature growth. Regardless, the crystal quality, surface roughness, and lattice constants being close to theory when using low temperature epitaxy suggests that a significant improvement is observed when using low temperatures. This revelation should be applied to a wider range of scandium contents, especially ones closer to the wurtzite to cubic transition point to attempt to suppress cubic phases and improve crystal quality. Additionally, the electrical properties of such films should be investigated to see if when cubic phases are suppressed the sheet charge increases due to increased polarization with a lack of non-polar cubic inclusions.

9.6.4 Fabricate Full HEMTs with metal rich ScAlN

ScAlN/GaN HEMT structures have been grown and studied via Hall effect measurements. The next step in development would be to fabricate full HEMT devices with the same structures. Full devices would allow for device parameters to be extracted and compared to the state of the art. Device parameters could be correlated to material properties and growth conditions and further optimization could be performed to push technology forward.

9.6.5 Examine Ferroelectric Properties of metal rich ScAlN

ScAlN is an interesting ferroelectric material with several memory and transistor applications possible. To date very few MBE groups have achieved ferroelectric ScAlN. Given the state of the art material quality and near theoretical lattice constants observed in metal rich low temperature grown ScAlN, the ferroelectric properties of various Sc compositions should be examined.

CITATIONS

[1] B.U.K. Mishra, L. Shen, T.E. Kazior, and Y. Wu, **96**, 287 (2008).

[2] N.S. Mansour, K.W. Kim, and M.A. Littlejohn, J. Appl. Phys. **77**, 2834 (1998).

[3] S.K.O. Leary, B.E. Foutzb, M.S. Shur, U. V Bhapkar, and L.F. Eastmanb, **105**, 621 (1998).

[4] F.A. Ponce and D.P. Bour, Nature **386**, 351 (1997).

[5] S.P. Denbaars, D. Feezell, K. Kelchner, S. Pimputkar, C. Pan, C. Yen, S. Tanaka, Y. Zhao, N. Pfaff, R. Farrell, M. Iza, S. Keller, U. Mishra, J.S. Speck, and S. Nakamura, Acta Mater. **61**, 945 (2013).

[6] J. Wu, J. Appl. Phys. **106**, 011101 (2009).

[7] H. Hirayama, N. Maeda, S. Fujikawa, S. Toyoda, and N. Kamata, Jpn. J. Appl. Phys. **53**, (2014).

[8] T. Nishida, H. Saito, and N. Kobayashi, Appl. Phys. Lett. **79**, 711 (2001).

[9] H. Hirayama, S. Fujikawa, J. Noguchi, Norimichi Norimatsu, K. Takano, Takayoshi Tsubaki, and N. Kamata, Phys. Status Solidi A **206**, 1176 (2009).

[10] C. Kuhn, L. Sulmoni, M. Guttmann, J. Glaab, N. Susilo, T. Wernicke, M. Weyers, and M. Kneissl, Photonics Res. **7**, B7 (1999).

[11] Z. Ma, H. Cao, S. Lin, X. Li, and L. Zhao, Solid State Electron. **156**, 92 (2019).

[12] R. Zwierz, S. Golka, K. Kachel, D. Siche, R. Fornari, P. Sennikov, A. Vodopyanov, and A. V. Pipa, Cryst. Res. Technol. **48**, 186 (2013).

[13] C.A.M. Fabien and W.A. Doolittle, Sol. Energy Mater. Sol. Cells **130**, 354 (2014).

[14] E.A. Clinton, E. Vadiee, M.B. Tellekamp, and W.A. Doolittle, J. Appl. Phys. **126**, 015705 (2019).

[15] S.Y. Karpov, R.A. Talalaev, Y.N. Makarov, N. Grandjean, J. Massies, and B. Damilano, Surf. Sci. **450**, 191 (2000).

[16] A.J. Ptak, M.R. Millecchia, T.H. Myers, K.S. Ziemer, and C.D. Stinespring, Appl. Phys. Lett. **74**, 3836 (1999).

[17] K. Hiramatsu, T. Detchprohm, and I. Akasaki, Jpn. J. Appl. Phys. **32**, 1528 (1993).

[18] R. Blasco, A. Núñez-Cascajero, M. Jiménez-Rodríguez, D. Montero, L. Grenet, J. Olea, F.B. Naranjo, and S. Valdueza-Felip, Phys. Status Solidi Appl. Mater. Sci. **216**, 1 (2019).

[19] A. Knübel, R. Aidam, V. Cimalla, L. Kirste, M. Baeumler, C. Leancu, V. Lebedev, J. Wallauer, M. Walther, and J. Wagner, Phys. Status Solidi A **6**, 1480 (2009).

[20] M. Higashiwaki and T. Matsui, Jpn. J. Appl. Phys. **41**, 540 (2002).

[21] E. Iliopoulos, A. Georgakilas, E. Dimakis, A. Adikimenakis, K. Tsagaraki, M. Androulidaki, and N.T. Pelekanos, Phys. Status Solidi A **203**, 102 (2006).

[22] H. Ahmad, K. Motoki, E.A. Clinton, C.M. Matthews, Z. Engel, and W.A. Doolittle, Appl. Mater. Interfaces **12**, 37693 (2020).

[23] M. Moseley, B. Gunning, J. Greenlee, J. Lowder, G. Namkoong, and W.A. Doolittle, J. Appl. Phys. **112**, 014909 (2012).

[24] M. Moseley, J. Lowder, D. Billingsley, and W.A. Doolittle, Appl. Phys. Lett. **97**, 2008 (2010).

[25] M. Moseley, B. Gunning, J. Lowder, W.A. Doolittle, and G. Namkoong, J. Vac. Sci. Technol. B **31**, 03C104 (2013).

[26] S.D. Burnham, G. Namkoong, D.C. Look, B. Clafin, and W.A. Doolittle, J. Appl. Phys. **104**, 024902 (2008).

[27] G. Namkoong, E. Trybus, K.K. Lee, M. Moseley, W.A. Doolittle, and D.C. Look, Appl. Phys. Lett. **93**, 172112 (2008).

[28] B.P. Gunning, J. Lowder, M. Moseley, and W.A. Doolittle, Appl. Phys. Lett. **101**, 082106 (2012).

[29] C.A.M. Fabien and W.A. Doolittle, Sol. Energy Mater. Sol. Cells **130**, 354 (2014).

[30] C.A.M. Fabien, A. Maros, C.B. Honsberg, and W.A. Doolittle, IEEE J. Photovoltaics **6**, 460 (2016).

[31] E. Vadiee, E.A. Clinton, H. McFavilen, A.S. Weidenbach, Z. Engel, C. Matthews, C. Zhang, C. Arena, R.R. King, C.B. Honsberg, and W.A. Doolittle, Appl. Phys. Express **11**, (2018).

[32] E.A. Clinton, Z. Engel, E. Vadiee, J.V. Carpenter, Z.C. Holman, and W.A. Doolittle, Appl. Phys. Lett. **115**, (2019).

[33] E.A. Clinton, E. Vadiee, S. Shen, K. Mehta, P.D. Yoder, and W.A. Doolittle, Appl. Phys. Lett. **112**, 252103 (2018).

[34] C.A.M. Fabien, B.P. Gunning, W.A. Doolittle, A.M. Fischer, Y.O. Wei, H. Xie, and F.A. Ponce,

J. Cryst. Growth **425**, 115 (2015).

[35] I. Vattulainen, J. Merikoski, T. Ala-Nissila, and S.C. Ying, Phys. Rev. B - Condens. Matter Mater. Phys. **57**, 1896 (1998).

[36] E.A. Clinton, E. Vadiee, C.A.M. Fabien, M.W. Moseley, B.P. Gunning, W.A. Doolittle, A.M. Fischer, Y.O. Wei, H. Xie, and F.A. Ponce, Solid. State. Electron. **136**, 3 (2017).

[37] W. Gotz, L.T. Romano, N.M. Johnson, and R.J. Molnar, Mater. Res. Soc. Symp. Proc. **449**, 525 (1996).

[38] B. Gunning, J. Lowder, M. Moseley, and W.A. Doolittle, Appl. Phys. Lett. **101**, 082106 (2012).

[39] K.B. Nam, M.L. Nakarmi, J. Li, J.Y. Lin, and H.X. Jiang, Appl. Phys. Lett. **83**, 878 (2003).

[40] S. Nakamura, T. Mukai, M. Senoh, and N. Iwasa, Jpn. J. Appl. Phys. **31**, 139 (1992).

[41] U. Kaufmann, P. Schlotter, H. Obloh, K. Köhler, and M. Maier, Phys. Rev. B **62**, 867 (2000).

[42] G. Miceli and A. Pasquarello, Phys. Rev. B **93**, 165207 (2016).

[43] K. Iwata, T. Narita, M. Nagao, K. Tomita, K. Kataoka, T. Kachi, and N. Ikarashi, Appl. Phys. Express **12**, (2019).

[44] A. Bhattacharyya, W. Li, J. Cabula, T.D. Moustakas, D.J. Smith, and R.L. Herving, Appl. Phys. Lett. **85**, 4965 (2004).

[45] H. Turski, G. Muzioł, M. Siekacz, P. Wolny, K. Szkudlarek, A. Feduniewicz-Zmuda, K. Dybko, and C. Skierbiszewski, J. Cryst. Growth **482**, 56 (2018).

[46] N. Tetsuo, I. Nobuyuki, T. Kazuyoshi, K. Keita, and K. Tetsu, J. Appl. Phys. **124**, 165706 (2018).

[47] R.R. Lieten, V. Motsnyi, L. Zhang, K. Cheng, M. Leys, S. Degroote, G. Buchowicz, O. Dubon, and G. Borghs, J. Phys. D. Appl. Phys. **44**, 135416 (2011).

[48] I. Ho and G.B. Stringfellow, Appl. Phys. Lett. **69**, 2701 (1996).

[49] R. Singh, D. Doppalapudi, T.D. Moustakas, and L.T. Romano, Appl. Phys. Lett. **70**, 1089 (1997).

[50] N.A. El-Masry, E.L. Piner, S.X. Liu, and S.M. Bedair, Appl. Phys. Lett. **72**, 40 (1998).

[51] D. Doppalapudi, S.N. Basu, K.F. Ludwig, and T.D. Moustakas, J. Appl. Phys. **84**, 1389 (1998).

[52] Z.C. Feng, T.R. Yang, R. Liu, and T.S.A. Wee, Mater. Sci. Semicond. Process. **5**, 39 (2002).

[53] S. Chichibu, T. Sota, K. Wada, and S. Nakamura, J. Vac. Sci. Technol. B **16**, 2204 (1998).

[54] F. Wang, Z. Ji, Q. Wang, X. Wang, S. Qu, X. Xu, Y. Lv, and Z. Feng, J. Appl. Physicsn **144**, (2013).

[55] R.A. Oliver, S.E. Bennett, T. Zhu, D.J. Beesly, M.J. Kappers, D.W. Saxey, A. Cerezo, and C.J. Humphreys, J. Phys. D Appl. Phys. **43**, 354003 (2010).

[56] Y. Lai, C. Liu, Y. Lin, T.-H. Hsueh, R.-M. Lin, D.-Y. Lyu, Z.-X. Peng, and T.-Y. Ling, Nanotechnology **17**, 3734 (2006).

[57] M. Bosi and R. Fornari, J. Cryst. Growth **265**, 434 (2004).

[58] M. Moseley, B. Gunning, J. Greenlee, J. Lowder, G. Namkoong, and W.A. Doolittle, J. Appl. Phys. **112**, 014909 (2012).

[59] M. Moseley, B. Gunning, J. Lowder, W.A. Doolittle, and G. Namkoong, J. Vac. Sci. Technol. B, Nanotechnol. Microelectron. Mater. Process. Meas. Phenom. **31**, 03C104 (2013).

[60] A.M. Fischer, Y.O. Wei, F.A. Ponce, M.W. Moseley, B.P. Gunning, and W.A. Doolittle, Appl. Phys. Lett. **103**, 131101 (2013).

[61] K.S.A. Butcher, D. Alexandrov, P. Terziyska, V. Georgiev, D. Georgieva, and P.W. Binsted, Phys. Status Solidi A **209**, 41 (2012).

[62] A. Botchkarev, A. Salvador, B. Sverdlov, J. Myoung, and H. Morkoç, J. Appl. Phys. **77**, 4455 (1995).

[63] Ž. Gacevic, V.J. Gómez, N. García Lepetit, P.E.D. Soto Rodríguez, A. Bengoechea, S. Fernández-Garrido, R. Nötzel, and E. Calleja, J. Cryst. Growth **364**, 123 (2013).

[64] K.H. Chiu, J.H. Chen, H.R. Chen, and R.S. Huang, Thin Solid Films **515**, 4819 (2007).

[65] V. Darakchieva, M. Beckers, M.Y. Xie, L. Hultman, B. Monemar, J.F. Carlin, E. Feltin, M. Gonschorek, and N. Grandjean, J. Appl. Phys. **103**, 103513 (2008).

[66] F. Medjdoub, J.-F. Carlin, M. Gonschorek, M.. A. Py, N. Grandjean, S. Vandenbrouck, C. Gaquière, J.. C. Dejaeger, and E. Kohn, Electron. Lett. **42**, 779 (2006).

[67] J.-F. Carlin and M. Ilegems, Appl. Phys. Lett. **83**, 668 (2003).

[68] J. Dorsaz, J.F. Carlin, C.M. Zellweger, S. Gradecak, and M. Ilegems, Phys. Stat. Sol. **201**, 2675

(2004).

[69] H.J. Kim, S. Choi, S.-S. Kim, J.-H. Ryou, P.D. Yoder, R.D. Dupuis, A.M. Fischer, K. Sun, and F.A. Ponce, Appl. Phys. Lett. **96**, 101102 (2010).

[70] C. Hums, A. Gadanecz, A. Dadgar, J. Bläsing, P. Lorenz, S. Krischok, F. Bertram, A. Franke, J.A. Schaefer, J. Christen, and A. Krost, Phys. Stat. Sol. **6**, 451 (2009).

[71] N. Re-, M. May, J.J. Dooiey, M.C. Morgan, A.K.N. Reddy, R.H. Williams, E.A. Parson, D.W. Keith, M.C. Zinyowera, D.J. Dokken, R.E. Evenson, W. Ruttan, and M.I. Nadiri, **285**, 692 (2000).

[72] V.G. De and A. V Vozny, **39**, 623 (2005).

[73] N.A. El-Masry, E.L. Piner, S.X. Liu, and S.M. Bedair, Appl. Phys. Lett **72**, 40 (1998).

[74] S. Choi, F. Wu, R. Shivaraman, E.C. Young, and J.S. Speck, Appl. Phys. Lett. **100**, 232102 (2012).

[75] L. Zhou, D.J. Smith, M.R. Mccartney, D.S. Katzer, and D.F. Storm, Appl. Phys. Lett. **90**, 081917 (2007).

[76] M. Sawicka, N. Fiuczek, P. Wolny, A. Feduniewicz-Zmuda, M. Siekacz, M. Krysko, K. Nowakowski-Szkudlarek, J. Smalc-Koziorowska, Ž. Gacevic, E. Calleja, and C. Skierbiszewski, J. Cryst. Growth J. **544**, (2020).

[77] W. Terashima, S.B. Che, Y. Ishitani, and A. Yoshikawa, Japanese J. Appl. Physics, Part 2 Lett. **45**, (2006).

[78] E.C.H. Kyle, S.W. Kaun, F. Wu, B. Bonef, and J.S. Speck, J. Cryst. Growth **454**, 164 (2016).

[79] Y. Houchin, A. Hashimoto, and A. Yamamoto, Phys. Status Solidi Curr. Top. Solid State Phys. **5**, 1571 (2008).

[80] T. Hempel, K. Lorenz, J. Bläsing, A. Diez, C. Hums, A. Dadgar, J. Christen, E. Alves, and A. Krost, Appl. Phys. Lett. **90**, 022105 (2007).

[81] T.T. Kang, M. Yamamoto, M. Tanaka, A. Hashimoto, and A. Yamamoto, J. Appl. Phys. **106**, 1 (2009).

[82] Y. Taniyasu, J.-F. Carlin, A. Castiglia, R. Butté, and N. Grandjean, Appl. Phys. Lett. **101**, 082113 (2012).

[83] A.T. Cheng, Y.K. Su, W.C. Lai, Y.Z. Chen, and S.Y. Kuo, J. Electron. Mater. **37**, 1070 (2008).

[84] H.F. Liu, C.C. Tan, G.K. Dalapati, and D.Z. Chi, J. Appl. Phys. **112**, 1 (2012).

[85] H.F. Liu, S.B. Dolmanan, S. Tripathy, G.K. Dalapati, C.C. Tan, and D.Z. Chi, J. Phys. D. Appl. Phys. **46**, (2013).

[86] A. Núñez-Cascajero, S. Valdueza-Felip, R. Blasco, M. de la Mata, S.I. Molina, M. González-Herráez, E. Monroy, and F.B. Naranjo, J. Alloys Compd. **769**, 824 (2018).

[87] J. Yun, J.I. Shim, and H. Hirayama, Appl. Phys. Express **8**, 022104 (2015).

[88] C. Weisbuch, M. Piccardo, L. Martinelli, J. Iveland, J. Peretti, and J.S. Speck, Phys. Status Solidi A **5**, 899 (2015).

[89] D.S. Meyaard, G. Lin, Q. Shan, J. Cho, E.F. Schubert, H. Shim, M. Kim, and C. Sone, Appl. Phys. Lett. **251115**, 251115 (2011).

[90] B. Galler, A. Laubsch, A. Wojcik, H. Lugauer, A. Gomez-Iglesias, M. Sabathil, and B. Hahn, Phys. Status Solidi C **8**, 2372 (2011).

[91] M.F. Schubert, S. Chhajed, J.K. Kim, E.F. Schubert, D.D. Koleske, M.H. Crawford, S.R. Lee, A.J. Fischer, G. Thaler, and M.A. Banas, Appl. Phys. Lett. **91**, (2007).

[92] T. Akasaka, H. Gotoh, T. Saito, and T. Makimoto, Appl. Phys. Lett. **85**, 3089 (2004).

[93] C. Haller, J.F. Carlin, G. Jacopin, D. Martin, R. Butté, and N. Grandjean, Appl. Phys. Lett. **111**, 262101 (2017).

[94] A.M. Armstrong, B.N. Bryant, M.H. Crawford, D.D. Koleske, S.R. Lee, and J.J. Wierer, J. Appl. Phys. **117**, 134501 (2015).

[95] C. Haller, J.F. Carlin, G. Jacopin, W. Liu, D. Martin, R. Butté, and N. Grandjean, Appl. Phys. Lett. **113**, 111106 (2018).

[96] T. Li, Q.Y. Wei, A.M. Fisher, J.Y. Huang, Y.U. Huang, F.A. Ponce, J.P. Liu, Z. Lochner, J.H. Ryou, and R.D. Dupuis, Appl. Phys. Lett. **102**, 04115 (2013).

[97] S. Han, D. Lee, S. Lee, C. Cho, M. Kwon, S.P. Lee, D.Y. Noh, D. Kim, Y.C. Kim, and S. Park, Appl. Phys. Lett. **94**, 231123 (2009).

[98] C.H. Wang, C.C. Ke, C.Y. Lee, S.P. Chang, W.T. Chang, J.C. Li, Z.Y. Li, H.C. Tang, H.C. Kuo, T.C. Lu, and S.C. Wang, Appl. Phys. Lett. **97**, 1 (2010).

[99] R. Lin, S. Yu, S. Chang, T. Chiang, S. Chang, and C. Chen, Appl. Phys. Lett. **101**, 081120 (2012).

[100] F. Zhang, N. Can, S. Hafiz, M. Monavarian, S. Das, V. Avrutin, Ü. Özgür, and H. Morkoç, Appl. Phys. Lett. **106**, 181105 (2015).

[101] M. Usman, A. Anwar, K. Saba, M. Munsif, and P. Perlin, Mater. Sci. Eng. B **258**, (2020).

[102] M.A. Khan, Phys. Status Solidi Appl. Mater. Sci. **203**, 1764 (2006).

[103] M.A. Khan, E. Matsuura, Y. Kashima, and H. Hirayama, Phys. Status Solidi A **216**, 1900185 (2019).

[104] H. Hirayama, N. Maeda, S. Fujikawa, S. Toyoda, and N. Kamata, Jpn. J. Appl. Phys. **53**, 100209 (2014).

[105] Y. Nagasawa and A. Hirano, Appl. Sci. **8**, (2018).

[106] H. Ahmad, Z. Engel, C.M. Matthews, S. Lee, and W.A. Doolittle, J. Appl. Phys. **131**, 175701 (2022).

[107] M. Shatalov, W. Sun, R. Jain, A. Lunev, X. Hu, A. Dobrinsky, Y. Bilenko, J. Yang, G.A. Garret, L.E. Rodak, M. Wraback, M. Shur, and R. Gaska, Semicondcutor Sci. an Technol. **29**, 084007 (2014).

[108] J.-S. Park, J.K. Kim, J. Cho, and T.-Y. Seong, ECS J. Solid State Sci. Technol. **6**, Q42 (2017).

[109] C.J. Humphreys, Use Effic. Light. **83**, 459 (2008).

[110] J.K. Sheu, S.J. Chang, C.H. Kuo, Y.K. Su, L.W. Wu, Y.C. Lin, W.C. Lai, J.M. Tsai, G.C. Chi, and R.K. Wu, IEEE Photonics Technol. Lett. **15**, 18 (2003).

[111] J. Hwang, R. Hashimoto, S. Saito, and S. Nunoue, Appl. Phys. Express **7**, 071003 (2014).

[112] A. Dussaigne, F. Barbier, B. Damilano, S. Chenot, A. Grenier, A.M. Papon, B. Samual, B. Ben Bakir, D. Vaufrey, J.C. Pillet, A. Gasse, O. Ledoux, M. Rozhavskay, and D. Sodda, J. Appl. Phys. **128**, 135704 (2020).

[113] T. Mukai, M. Yamada, and S. Nakamura, Jpn. J. Appl. Phys. **38**, 3976 (1999).

[114] J.A. Phys, R.C. Cramer, E.C.H. Kyle, and J.S. Speck, **035703**, (2019).

[115] S.P. Bremner, M.Y. Levy, and C.B. Honsberg, Prog. PhotovoltaicsL Res. Appl. **16**, 225 (2008).

[116] A.G. Bhuiyan, K. Sugita, A. Hashimoto, and A. Yamamoto, IEEE J. Photovoltaics **2**, 276 (2012).

[117] C. Jiang, L. Jing, X. Huang, M. Liu, C. Du, T. Liu, X. Pu, W. Hu, and Z.L. Wang, ACS Nano **11**, 9405 (2017).

[118] C.A.M. Fabien, A. Maros, S. Member, C.B. Honsberg, S. Member, W.A. Doolittle, and S. Member, IEEE J. Photovoltaics **6**, 460 (2016).

[119] B.R. Jampana, A.G. Melton, M. Jamil, N.N. Faleev, R.L. Opila, I.T. Ferguson, and C.B. Honsberg, IEEE Electron Device Lett. **31**, (2010).

[120] C.H. Henry, J. Appl. Phys. **51**, (2008).

[121] D.J. Friedman, Curr. Opin. Solid State Mater. Sci. **14**, 131 (2010).

[122] M. Chu, W. Liao, R. Horng, and T. Tsai, IEEE Electron Device Lett. **32**, 922 (2011).

[123] L. Sang, M. Liao, N. Ikeda, Y. Koide, and M. Sumiya, Appl. Phys. Lett. **99**, 161109 (2011).

[124] S.-W. Feng, C.-M. Lai, C.-H. Chen, W.-C. Sun, and L.-W. Tu, J. Appl. Phys. **108**, (2010).

[125] N.G. Young, R.M. Farrell, Y.L. Hu, Y. Terao, M. Iza, S. Keller, S.P. DenBaars, S. Nakamura, and J.S. Speck, **103**, (2013).

[126] O. Ambacher, B. Christian, N. Feil, D.F. Urban, C. Elsässer, M. Prescher, and L. Kirste, J. Appl. Phys. **130**, (2021).

[127] O. Ambacher, B. Christian, M. Yassine, M. Baeumler, S. Leone, and R. Quay, J. Appl. Phys. **129**, (2021).

[128] K. Furuta, K. Hirata, S.A. Anggraini, M. Akiyama, M. Uehara, and H. Yamada, J. Appl. Phys. **130**, (2021).

[129] D. Wang, P. Wang, S. Mondal, S. Mohanty, T. Ma, E. Ahmadi, and Z. Mi, Adv. Electron. Mater. **2200005**, 1 (2022).

[130] P. Wang, D. Wang, N.M. Vu, T. Chiang, J.T. Heron, and Z. Mi, Appl. Phys. Lett. **118**, (2021).

[131] N. Wolff, S. Fichtner, B. Haas, M.R. Islam, F. Niekiel, M. Kessel, O. Ambacher, C. Koch, B. Wagner, F. Lofink, and L. Kienle, J. Appl. Phys. **129**, (2021).

[132] K. Frei, R. Trejo-Hernández, S. Schütt, L. Kirste, M. Prescher, R. Aidam, S. Müller, P. Waltereit, O. Ambacher, and M. Fiederle, Jpn. J. Appl. Phys. **58**, (2019).

[133] A.J. Green, J.K. Gillespie, R.C. Fitch, D.E. Walker, M. Lindquist, A. Crespo, D. Brooks, E. Beam, A. Xie, V. Kumar, J. Jimenez, C. Lee, Y. Cao, K.D. Chabak, and G.H. Jessen, IEEE Electron Device Lett. **40**, 1056 (2019).

[134] M.T. Hardy, B.P. Downey, N. Nepal, D.F. Storm, D.S. Katzer, and D.J. Meyer, ECS Meet. Abstr. **MA2017-02**, 1334 (2017).

[135] M.T. Hardy, B.P. Downey, N. Nepal, D.F. Storm, D.S. Katzer, and D.J. Meyer, Appl. Phys. Lett. **110**, (2017).

[136] M.B. Tahhan, J.A. Logan, M.T. Hardy, M.G. Ancona, B. Schultz, B. Appleton, T. Kazior, D.J. Meyer, and E.M. Chumbes, IEEE Trans. Electron Devices **69**, 962 (2022).

[137] M. Akiyama, K. Kano, and A. Teshigahara, Appl. Phys. Lett. **95**, 1 (2009).

[138] K. Arakawa, T. Yanagitani, K. Kano, A. Teshigahara, and M. Akiyama, Proc. - IEEE Ultrason. Symp. 1050 (2010).

[139] M. Sumisaka, K. Yamazaki, S. Fujii, G. Tang, T. Han, Y. Suzuki, S. Otomo, T. Omori, and K.Y. Hashimoto, Jpn. J. Appl. Phys. **54**, (2015).

[140] Y. Zhang, W. Zhu, D. Zhou, Y. Yang, and C. Yang, J. Mater. Sci. Mater. Electron. **26**, 472 (2015).

[141] J.C. Yang, X.Q. Meng, C.T. Yang, and Y. Zhang, Appl. Surf. Sci. **287**, 355 (2013).

[142] H. Ahmad, K. Motoki, E.A. Clinton, C.M. Matthews, Z. Engel, and A. Doolittle, ACS Appl. Mater. Interfaces **12**, 37693 (2020).

[143] Z. Engel, E.A. Clinton, C.M. Matthews, and W.A. Doolittle, J. Appl. Phys. **127**, (2020).

[144] S.Y. Kwon, H.J. Kim, H. Na, Y.W. Kim, H.C. Seo, H.J. Kim, Y. Shin, E. Yoon, and Y.S. Park, J. Appl. Phys. **99**, 1 (2006).

[145] F. Widmann, B. Daudin, G. Feuillet, N. Pelekanos, and J.L. Rouvière, Appl. Phys. Lett. **73**, 2642 (1998).

[146] M.T. Hardy, E.N. Jin, N. Nepal, D.S. Katzer, B.P. Downey, V.J. Gokhale, D.F. Storm, and D.J. Meyer, Appl. Phys. Express **13**, (2020).

[147] P. Wang, D. Wang, Y. Bi, B. Wang, J. Schwartz, R. Hovden, and Z. Mi, Appl. Phys. Lett. **120**, 012104 (2022).

[148] J.P. Harrang, R.J. Higgins, R.K. Goodall, P.R. Jay, M. Laviron, and P. Delescluse, Phys. Rev. B **32**, 8126 (1985).

[149] N. Ma and D. Jena, Phys. Rev. X **4**, 1 (2014).

[150] J. Antoszewski, M. Gracey, J.M. Dell, L. Faraone, T.A. Fisher, G. Parish, Y.F. Wu, and U.K. Mishra, J. Appl. Phys. **87**, (2000).

[151] V. Umansky, R. de-Picciotto, and M. Heiblum, Appl. Phys. Lett. **71**, 683 (1997).

[152] S. Leone, J. Ligl, C. Manz, L. Kirste, T. Fuchs, H. Menner, M. Prescher, J. Wiegert, A. Žukauskaitė, R. Quay, and O. Ambacher, Phys. Status Solidi - Rapid Res. Lett. **14**, 1 (2020).

[153] Z. Engel, E.A. Clinton, K. Motoki, H. Ahmad, C.M. Matthews, and W.A. Doolittle, J. Appl. Phys. **130**, (2021).

[154] B.P. Gunning, E.A. Clinton, J.J. Merola, W.A. Doolittle, R.C. Bresnahan, B.P. Gunning, E.A. Clinton, J.J. Merola, W.A. Doolittle, and R.C. Bresnahan, J. Appl. Phys. **118**, 155302 (2017).

[155] E.A. Clinton, Z. Engel, E. Vadiee, J. V Carpenter, Z.C. Holman, and W.A. Doolittle, Appl.

Phys. Lett. **115**, 082104 (2019).

[156] M. Moseley, J. Lowder, D. Billingsley, and W.A. Doolittle, Appl. Phys. Lett. **97**, 1 (2010).

[157] B. Heying, X.H. Wu, S. Keller, Y. Li, D. Kapolnek, B.P. Keller, S.P. DenBaars, and J.S. Speck, Appl. Phys. Lett. **68**, 643 (1996).

[158] E. Monroy, B. Daudin, E. Bellet-Amalric, N. Gogneau, D. Jalabert, F. Enjalbert, J. Brault, J. Barjon, and L.S. Dang, J. Appl. Phys. **93**, 1550 (2003).

[159] C.S. Gallinat, G. Koblmüller, J.S. Brown, and J.S. Speck, J. Appl. Phys. **102**, 064907 (2007).

[160] B.R. Nag and S. Gangopadhyay, Phys. Stat. Sol. **179**, 463 (1993).

[161] S. Nakamura, Science (80-.). **281**, 956 (1998).

[162] J. Kuzmík, IEEE Electron Device Lett. **22**, 510 (2001).

[163] N. Sarazin, E. Morvan, M.A. Di Forte Poisson, M. Oualli, C. Gaquiere, O. Jardel, O. Drisse, M. Tordjman, M. Magis, and S.L. Delage, IEEE Electron Device Lett. **31**, 11 (2010).

[164] J.W. Chung, W.E. Hoke, E.M. Chumbes, and T. Palacios, IEEE Electron Device Lett. **31**, 195 (2010).

[165] V. Kumar, W. Lu, R. Schwindt, A. Kuliev, G. Simin, J. Yang, M.A. Khan, and I. Adesida, IEEE Electron Device Lett. **23**, 455 (2002).

[166] H. Hirayama, S. Fujikawa, and N. Kamata, Electron. Commun. Japan **98**, 1 (2015).

[167] R.J. Kaplar, A.A. Allerman, A.M. Armstrong, M.H. Crawford, J.R. Dickerson, A.J. Fischer,

A.G. Baca, and E.A. Douglas, ECS J. Solid State Sci. Technol. **6**, Q3061 (2017).

[168] W. Saito, Y. Takada, M. Kuraguchi, K. Tsuda, and I. Omura, IEEE Trans. Electron Devices **53**, 356 (2006).

[169] H. Ahmad, Z. Engel, A. Ghosh, C.M. Matthews, and W. Alan Doolittle, IEEE Trans. Electron Devices **69**, 2566 (2022).

[170] J.K. Sheu, S.J. Chang, C.H. Kuo, Y.K. Su, L.W. Wu, Y.C. Lin, W.C. Lai, J.M. Tsai, G.C. Chi, and R.K. Wu, IEEE Photonics Techno **15**, 18 (2003).

[171] Y.K. Kuo, J.Y. Chang, M.C. Tsai, and S.H. Yen, Appl. Phys. Lett. **95**, 011116 (2009).

[172] S. Nakamura, M. Senoh, S. Nagahama, N. Iwasa, T. Yamada, T. Matsushita, H. Kiyoku, and Y. Sugimoto, Jpn. J. Appl. Phys. **35**, 74 (1996).

[173] M. Kuramoto, S. Kobayashi, T. Akagi, K. Tazawa, K. Tanaka, T. Saito, and T. Takeuchi, Appl. Sci. **9**, 416 (2019).

[174] T. Takeuchi, S. Kamiyama, M. Iwaya, and I. Akasaki, Reports Prog. Phys. **82**, 012502 (2019).

[175] H. Hirayama, T. Yatabe, N. Noguchi, T. Ohashi, and N. Kamata, Appl. Phys. Lett. **91**, 071901 (2007).

[176] M. Miyoshi, M. Yamanaka, T. Egawa, and T. Takeuchi, Appl. Phys. Express **11**, 051001 (2018).

[177] R. Goldhahn, P. Schley, A.T. Winzer, G. Gobsch, V. Cimalla, O. Ambacher, M. Rakel, C. Cobet, N. Esser, H. Lu, and W.J. Schaff, Phys. Status Solidi **203**, 42 (2006).

[178] M. Moseley, B. Gunning, J. Greenlee, J. Lowder, G. Namkoong, and W. Alan Doolittle, J. Appl. Phys. **112**, (2012).

[179] R. Butté, J.F. Carlin, E. Feltin, M. Gonschorek, S. Nicolay, G. Christmann, D. Simeonov, A. Castiglia, J. Dorsaz, H.J. Buehlmann, S. Christopoulos, G. Baldassarri Höger Von Högersthal, A.J.D. Grundy, M. Mosca, C. Pinquier, M.A. Py, F. Demangeot, J. Frandon, P.G. Lagoudakis, J.J. Baumberg, and N. Grandjean, J. Phys. D. Appl. Phys. **40**, 6328 (2007).

[180] S.N. Alam, V.Z. Zubialevich, B. Ghafary, and P.J. Parbrook, Sci. Rep. **10**, 16205 (2020).

[181] E.A. Clinton, Z. Engel, E. Vadiee, J. V. Carpenter, Z.C. Holman, and W.A. Doolittle, Appl. Phys. Lett. **115**, 082104 (2019).

[182] P. Kozodoy, Y.P. Smorchkov, M. Hansen, H. Xing, S.P. DenBaars, U.K. Mishra, A.W. Saxler, R. Perrin, and W.C. Mitchel, Appl. Phys. Lett. **75**, 2444 (1999).

[183] Y. Yan Zhang and Y. An Yin, Appl. Phys. Lett. (2011).

[184] S.H. Park and S.L. Chuang, Appl. Phys. Lett. **76**, 1981 (2000).

[185] T. Kinoshita, T. Obata, H. Yanagi, and S.I. Inoue, Appl. Phys. Lett. **102**, 012105 (2013).

[186] S. Heikman, S. Keller, Y. Wu, J.S. Speck, S.P. DenBaars, and U.K. Mishra, J. Appl. Phys. **93**, 10114 (2003).

[187] O. Ambacher, J. Smart, J.R. Shealy, N.G. Weimann, K. Chu, M. Murphy, W.J. Schaff, L.F. Eastman, R. Dimitrov, M. Stutzmann, W. Reiger, and J. Hilsenbeck, J. Appl. Phys. **85**, 3222 (1999).

[188] O. Aktas, A. Kuliev, V. Kumar, R. Schwindt, S. Toshkov, D. Costescu, J. Stubbins, and I. Adesida, Solid. State. Electron. **48**, 471 (2004).

[189] J.P. Zhang, H.M. Wang, M.E. Gaevski, C.Q. Chen, Q. Fareed, J.W. Yang, G. Simin, and A.M. Khan, Appl. Phys. Lett. **80**, 3542 (2002).

[190] U. Zeimer, V. Kueller, A. Knauer, A. Mogilatenko, M. Weyers, and M. Kneissl, J. Cryst. Growth **377**, 32 (2013).

[191] Y. Jianchang, W. Junxi, L. Naixin, L. Zhe, R. Jun, and L. Jinmin, J. Semicond. **30**, 103001 (2009).

[192] S. Kamiyama, M. Iwaya, N. Hayashi, T. Takeuchi, H. Amato, I. Akasaki, S. Watanabe, Y. Kaneko, and N. Yamada, J. Cryst. Growth **223**, 83 (2001).

[193] M. Stutzmann, O. Ambacher, A. Cros, M.S. Brandt, H. Angerer, R. Dimitrov, N. Reinacher, T. Metzger, R. Höpler, D. Brunner, R. Freudenberg, F Handschuh, and C. Deger, Mater. Sci. Eng. B **B50**, 212 (1997).

[194] C.R. Elsass, I.P. Smorchkova, B. Heying, E. Haus, P. Fini, K. Maranowski, J.P. Ibbetson, S. Keller, P.M. Petroff, S.P. DenBaars, U.K. Mishra, and J.S. Speck, Appl. Phys. Lett. **74**, 3528 (1999).

[195] H.M. Wang, J.P. Zhang, C.Q. Chen, Q. Fareed, J.W. Yang, and A.M. Khan, Appl. Phys. Lett. **81**, 604 (2002).

[196] J.H. Park, K.D. Y, S. Hwang, D. Meyaard, E.F. Schubert, Y.D. Han, J.W. Choi, J. Cho, and J.K. Kim, Appl. Phys. Lett. **103**, 061104 (2013).

[197] M. M, C. Kuhn, E. Ziffer, T. Simoneit, V. Kueller, A. Knauer, J. Rass, T. Wernicke, S. Einfeldt, M. Weyers, and M. Kneissl, Appl. Phys. Lett. **108**, 151108 (2016).

[198] K.E. Waldrip, J. Han, J.J. Figiel, H. Zhou, E. Makarona, and A. V Nurmikko, Appl. Phys. Lett. **78**, 3205 (2001).

[199] N. Nakada, H. Ishikawa, T. Egawa, and J. Takashi, Jpn. J. Appl. Phys. **42**, 144 (2003).

[200] N. Nakada, M. Nakaji, H. Ishikawa, T. Egawa, M. Umeno, and J. T, Appl. Phys. Lett. **76**, 1804 (2000).

[201] E.L. Waldron, J.W. Graff, and E.F. Schubert, Appl. Phys. Lett. **79**, 2737 (2001).

[202] S.R. Xu, Y. Hao, J.C. Zhang, X.W. Zhou, L.A. Yang, J.F. Zhang, H.T. Duan, Z.M. Li, M. Wei, S.G. Hu, Y.R. Cao, Q.W. Zhu, Z.H. Xu, and W.P. Gu, J. Cryst. Growth **311**, 3622 (2009).

[203] W.E. Hoke, P.J. Lemonias, and A. Torabi, J. Vac. Sci. Technol. B **16**, 3041 (1998).

[204] Z. Engel, E.A. Clinton, C.M. Matthews, and W.A. Doolittle, J. Appl. Phys. **127**, 125301 (2020).

[205] J.E. Northrup and J. Neugebauer, Phys. Rev. B - Condens. Matter Mater. Phys. (2000).

[206] M. Moseley, D. Billingsley, W. Henderson, E. Trybus, and W.A. Doolittle, J. Appl. Phys. **106**, 014905 (2009).

[207] S.J. Barnett, G.T. Brown, D.C. Houghton, and J.M. Baribeua, Appl. Phys. Lett. **54**, 1781 (1989).

[208] R. Niewa, D.A. Zherebtsov, M. Kirchner, M. Schmidt, and W. Schnelle, Chem. Mater. **16**, 5445 (2004).

[209] M.A. Moram, Y. Zhang, M.J. Kappers, Z.H. Barber, and C.J. Humphreys, Appl. Phys. Lett. **91**, 8 (2007).

[210] B.U. Haq, A. Afaq, G. Abdellatif, R. Ahmed, S. Naseem, and R. Khenata, Superlattices Microstruct. **85**, 24 (2015).

[211] H. Al-Brithen and A.R. Smith, Appl. Phys. Lett. **77**, 2485 (2000).

[212] Z. Gu, J.H. Edgar, J. Pomeroy, M. Kuball, and D.W. Coffey, J. Mater. Sci. Mater. Electron. **15**, 555 (2004).

[213] S. Acharya, A. Chatterjee, V. Bhatia, A.I.K. Pillai, M. Garbrecht, and B. Saha, Mater. Res. Bull. **143**, 111443 (2021).

[214] A. Jain, S. Ping Ong, G. Hautier, W. Chen, W.D. Richards, S. Dacek, S. Cholia, D. Hunter, D. Skinner, G. Ceder, and K.A. Persson, Mater. Proj. **1**, 011002 (2013).

[215] Z. Engel, E.A. Clinton, C.M. Matthews, and W.A. Doolittle, J. Appl. Phys. **127**, 125301 (2020).

[216] S. Satoh, K. Ohtaka, T. Shimatsu, and S. Tanaka, J. Appl. Phys. **132**, (2022).